DESIGN THEORY, MATERIALS SELECTION, AND FABRICATION OF HOLLOW CORE WAVEGUIDES FOR INFRARED TO THZ RADIATION

by

BRADLEY F. BOWDEN

A Dissertation submitted to the

Graduate School – New Brunswick

Rutgers, The State University of New Jersey

in partial fulfillment of the requirements

for the degree of

Doctor of Philosophy

Graduate Program in Ceramic and Materials Science and Engineering

written under the direction of

Professor James A. Harrington

and approved by

_____

_____

_____

_____

_____

New Brunswick, New Jersey

October, 2007

ABSTRACT OF THE DISSERTATION

DESIGN THEORY, MATERIALS SELECTION, AND FABRICATION OF HOLLOW CORE WAVEGUIDES FOR INFRARED TO THZ RADIATION

BY BRADLEY F. BOWDEN

DISSERTATION DIRECTOR:

PROF. JAMES A. HARRINGTON

Hollow core waveguides (HCWs) are comprised of a central hole surrounded by a highly reflective inner wall. The core can be filled with air, inert gas, or vacuum, allowing these waveguides to transmit a broad range of wavelengths with low attenuation. HCWs are of particular interest for the transmission of infrared (IR) to THz radiation, where it is otherwise difficult to find materials that have the optical, thermal, and mechanical properties required for use in solid core optical fibers.

Ray optics calculations are used to predict the attenuation of the low-loss Gaussian-like HE_{11} mode propagating in two types of HCWs: hollow Bragg fibers (HBFs) and metal/dielectric hollow glass waveguides (HGWs). These calculations provide guidance on the materials selection and design of HCWs optimized for CO_2 (10.6 μm) IR laser radiation and CO_2 pumped CH_3OH (119 μm) THz laser radiation.

An all-chalcogenide glass HBF is proposed for the delivery of CO_2 laser radiation. Such a fiber would combine a high refractive index contrast (ratio of the high to low refractive index) with low materials absorption, characteristics that are critical to the design of a low loss HBF. $Ge_{20}Se_{80}$ glass ($\tilde{n}_{\lambda=10.6\ \mu m} = 2.46 + i9.7e\text{-}7$) is identified as

an excellent candidate for the low refractive index composition due to its thermal stability and relatively low refractive index among chalcogenide glasses that transmit 10.6 μm radiation. To identify a high refractive index glass to combine with $Ge_{20}Se_{80}$, several glass compositions in the Ag-As-Se glass forming system are characterized using FTIR spectroscopy, CO_2 laser variable angle reflectometry, and CO_2 laser calorimetry. Of the compositions investigated, $Ag_{25}As_{40}Se_{35}$ glass ($\tilde{n}_{\lambda=10.6\ \mu m}$ = 3.10 + i1.7e-6) has the best thermal and optical properties for this application. Ray optics calculations show that a HBF made from alternating layers of $Ge_{20}Se_{80}$ and $Ag_{25}As_{40}Se_{35}$ glass could have orders of magnitude lower loss than any IR waveguide that has been demonstrated to date.

A metal/polymer coated HGW is proposed for the transmission of THz radiation. Ray optics calculations show that silver (Ag) has the best optical properties for use in this application. In theory, a polystyrene (PS) layer added over the silver coating can reduce the waveguide's attenuation by over an order of magnitude. Ag/PS HGWs are fabricated by extending coating techniques that were originally developed for IR transmitting HCWs. FTIR spectroscopy is used to determine the PS film thicknesses and confirm coating uniformity. Uniform PS films are deposited with thicknesses up to 16.7 μm, which is approximately ten times greater than what had previously been demonstrated using these techniques. The mode structure, attenuation, and coupling loss of Ag/PS HGWs are characterized using a CO_2 pumped CH_3OH THz laser tuned to emit 119 μm radiation. The best waveguide demonstrated in this study, a 2.2 mm bore diameter Ag/PS HGW with a 8.2 μm PS film thickness, has a loss of 0.95 dB/m and a coupling efficiency of 80 %. These attributes are the best that have been demonstrated for any THz waveguide to date.

ACKNOWLEDGEMENTS

The guidance of my advisor, Prof. James Harrington, has been immensely valuable in my development as a researcher, as a professional, and as a person. I would like to thank him for accepting me into his research group and providing me with the opportunity and means to pursue exciting and challenging problems. My accomplishments as a graduate student were made possible by his advice and encouragement. I am appreciative of all I have learned under Prof. Harrington's mentorship and I am confident his teachings will benefit me throughout my career.

I would like to thank my thesis committee members: Prof. John Federici, Prof. Jong Heo, Prof. John Matthewson, and Prof. George Sigel for their commitment to my education and for their significant contributions to my research.

The contributions of Dr. Oleg Mitrofanov, of Alcatel-Lucent Bell Labs, and Dr. Gilles Benoit, formerly of the Photonic Bandgap Fibers & Devices Group at MIT, were instrumental in the completion of this work. I can't possibly thank them enough.

I am grateful to my group members: Roshan George, Dan Gibson, Veena Gopal, Valencia Johnson, and Pål Pederson. They've helped me to understand the fundamentals of infrared waveguides and have provided valuable input towards the development of new ideas. Discussions with Ray Brennan, Kevin Farley, and Anil Kaza also contributed a great deal to this work.

I have been fortunate to work with several talented undergraduate research assistants: Charles Dooner, Andrew Gmitter, Jason Cutrera, Isaac Chao, Adam Karcz, and Jason Goncalves. Their hard work and creativity were critical to the completion of this research.

I am grateful for the use of equipment provided by Prof. Dunbar Birnie III, Prof. Federici (NJIT), Prof. Yoel Fink (MIT), Prof. Victor Greenhut, Prof. Rich Haber, Prof. Lisa Klein, Prof. Rick Lehman, Prof. Matthewson, Prof. Manish Chhowalla, and Dr. Mitrofanov (Bell Labs). I did my best not to break anything!

Special thanks go to Prof. Roger Cannon, Prof. Greenhut, and Prof. Klein for encouraging me to continue my academic studies in Rutgers' Graduate Program in Materials Science and Engineering. It was difficult to leave my home in Alfred, but I count it among the best decisions that I have ever made.

Many thanks to the friends that I've made in New Jersey: Al, Andrew, Anil, Asha, Bill, Brian, Caonabo, Cari, Dave, Drew, Errica, Isaac, J.D., Jaideep, James, Jason, Jen C., Jen L., Jess, Joe, Kevin, Leonid, Lorie, Lou, Luca, Monica, Navin, Pål, Ray, Shawn, Steve M., Steve R., Susan, Tum, Valencia, and Vivek. GO CHEFS!

I owe everything that I have to my family: Mom, Dad, Grandma, Judy, Jake, Amy, and Vic. Also included under family are my brothers from other mothers: Pat and Phil. Their friendship, advice, and support have been so important throughout my life.

Last, but most definitely not least, my proofreader; my drill sergeant; my chef; my "finder-of-things"; my navigator; my singer/songwriter; my inspiration; my best friend; my love: Jami Lacerte. I could never have done this without her patience, kindness, and love.

DEDICATION

This dissertation is dedicated to Jami. The day I met her was the first day of my life.

TABLE OF CONTENTS

ABSTRACT OF THE DISSERTATION ..... **ii**

ACKNOWLEDGEMENTS ..... **iv**

DEDICATION ..... **vi**

TABLE OF CONTENTS ..... **vii**

LIST OF FIGURES ..... **xi**

LIST OF TABLES ..... **xxii**

Chapter I Introduction **1**

I.A Background 1

I.B Applications of Infrared and THz Transmitting Waveguides 3

I.C Approach and Organization of the Dissertation 7

I.D References 9

Chapter II Design of Hollow Core Waveguides **13**

II.A Background 13

II.B Ray Optics Calculations for Hollow Core Waveguides 17

II.C Modes in Hollow Core Waveguides 18

II.D Coupling to the HE_{11} Mode 21

II.E Calculations of Reflectivity Coefficients 23

II.F Optimized Hollow Core Waveguide Structures 28

II.F-1 All-dielectric hollow Bragg fibers 27

II.F-2 Metal/dielectric hollow glass waveguides 31

II.G Characteristics of the OmniGuide Hollow Bragg Fiber 32

II.G-1 Structure and fabrication of OmniGuide fibers 33

II.G-2 Transmission of CO_2 laser radiation in OmniGuide fibers 34
II.G-3 Omnidirectional reflection 36
II.H Material Selection for Infrared Transmitting Hollow Bragg Fibers 40
II.I Chalcogen Based Hollow Bragg Fibers 42
II.I-1 Loss and refractive index contrast 43
II.I-2 Effect of additional layers 46
II.I-3 Effect of materials absorption 47
II.I-4 Layer thickness uniformity 50
II.J Design of Metal/Dielectric Hollow Glass Waveguide for THz Radiation 52
II.J-1 Metal selection for THz hollow glass waveguides 54
II.J-2 Evaluation of dielectrics for THz hollow glass waveguides 59
II.J-3 Silver/polystyrene hollow glass waveguides for THz radiation 63
II.K Summary 67
II.L References 69
Chapter III Chalcogenide Glass Hollow Bragg Fibers 73
III.A Background 73
III.B Germanium Selenide Glass 77
III.C Indentifying High Refractive Index Contrast Chalcogenide Glasses 80
III.D Optical Properties of Silver Arsenic Selenide Glasses 82
II.D-1 Glass fabrication 85

II.D-2 Fourier transform infrared spectroscopy 92
II.D-3 CO_2 laser variable angle reflectometry 95
II.D-4 CO_2 laser calorimetry 100
III.E THEORETICAL ANALYSIS OF GE-SE/AG-AS-SE HOLLOW BRAGG FIBERS 105
III.F CHALCOGENIDE GLASS HOLLOW BRAGG FIBER PREFORM FABRICATION AND DRAWING 107
III.G SUMMARY 113
III.H REFERENCES 115
Chapter IV Ag/PS Hollow Glass Waveguides for THz Radiation 120
IV.A BACKGROUND 120
IV.B FABRICATION OF METAL/DIELECTRIC HOLLOW CORE WAVEGUIDES 121
IV.C THE LIQUID FLOW COATING PROCESS 124
IV.D VISCOSITY OF POLYSTYRENE.TOLUENE SOLUTIONS 129
IV.E LIQUID FLOW COATING PROCESS STUDY 132
IV.E-1 Ag coating deposition 133
IV.E-2 Polystyrene thin film deposition 137
IV.E-3 Characterization of Ag/PS hollow glass waveguides by FTIR spectroscopy 141
IV.F AG/PS HOLLOW GLASS WAVEGUIDE CHARATERIZATION USING 119 μM THZ LASER RADIATION 149
IV.F-1 The SIFIR-50 laser 150
IV.F-2 Mode profiles 152
IV.F-3 Cutback loss measurements 155

IV.F-4 Coupling efficiency 158
IV.G SUMMARY 160
IV.H REFERENCES 162
Chapter V Conclusions and Future Work 166
V.A REFERENCES 170
Curriculum Vita 171

LIST OF FIGURES

Figure I-1 Schematic cross sections and refractive index profiles of the seven types of hollow core waveguides: ATIR waveguide (a), metal tube (b), metal-coated hollow glass waveguide (HGW) or hollow polymer waveguide (HPW) (c), metal/dielectric HGW or HPW (d), multilayer metal/dielectric HGW or HPW (e), hollow Bragg fiber (HBF) (f), and photonic crystal fiber (g). 4

Figure II-1 A schematic diagram of a hollow core waveguide that indicates the bore radius, a, and mode angle, Θ_z. 18

Figure II-2 A TEM plane wave propagating between two planar mirrors that satisfies the condition of self-consistency. The wavefronts of the initial plane wave, reflected plane wave, and twice reflected plane wave are shown in red, green, and blue, respectively. The diamond shaped pattern formed by the intersection of the wavefronts is analogous to a waveguide mode. 20

Figure II-3 The HE_{11} mode angle, θ_z, is plotted as a function of bore diameter, $2 \cdot a$, for HCWs transmitting CO_2 laser infrared radiation at 10.6 μm and CO_2 pumped CH_3OH THz radiation at 119 μm. 21

Figure II-4 The relative intensity distributions of the TEM_{00} Gaussian beam (a) with beam diameter, $\omega = 0.64 \cdot a$, and the HE_{11} mode (b) propagating in a HCW with bore diameter, a, are shown. The darkest regions correspond to the greatest intensities. 23

Figure II-5 A schematic diagram of a plane wave incident on a multilayer thin film. 25

Figure II-6 A schematic diagram of the multilayer alternating n_L/n_H all dielectric Bragg reflector design. 30

Figure II-7 A schematic diagram of the reflector design that includes a single dielectric layer on a metal substrate. 32

Figure II-8 A schematic of the OmniGuide HBF cross section.....34

Figure II-9 The transmission loss of the HE_{11} mode for 10.6 μm CO_2 laser radiation propagating in an OmniGuide fiber is plotted as a function of the number of layer pairs, *N*, that form the waveguide's reflective inner wall. The red curve indicates the loss when the complex refractive indices of the materials are considered. Only the real indices are considered in the calculation of the blue curve. a = 350 μm and λ_o = 10.6 μm. 35

Figure II-10 The average reflectivity coefficient, R_{avg}, of an OmniGuide fiber is plotted on a color scale within a wavelength vs. angle of incidence coordinate system. The extinction coefficients of the materials are ignored. The high reflectivity photonic bandgap regions appear as white bands in the diagram. N = 35, k = 0, and λ_o = 10.6 μm. 37

Figure II-11 The average reflectivity coefficient, R_{avg}, of an OmniGuide fiber is plotted on a black-to-white scale within a wavelength vs. angle of incidence coordinate system. The complex refractive indices of the materials are used in the calculations. Horizontal bands correspond to the absorption bands of PEI. N = 35 and λ_o = 10.6 μm. 37

Figure II-12 The average reflectivity coefficient, R_{avg}, is plotted as a function of angle of incidence for the wall of a Ag-coated HGW, a Ag/AgI coated HGW, and the OmniGuide fiber with and without materials absorption.....39

Figure II-13: A schematic diagram of the proposed fiber cross-section showing its air core (a), chalcogenide glass Bragg reflector film (b), and thick

polymer coating (c). A schematic of the film's layered structure and polymer substrate is shown below the cross section. 43

Figure II-14 HE_{11} transmission loss contours for CO_2 laser radiation are plotted in an n_H vs. n_L coordinate system for HBFs. Loss values are expressed in dB/m. a = 500 μm, k = 0, N = 25, and λ_o = 10.6 μm.....44

Figure II-15 Refractive index contrast n_H/n_L contours are plotted in an n_H vs. n_L coordinate system. 45

Figure II-16 Theoretical HE_{11} mode transmission loss for CO_2 laser radiation is plotted as a function of refractive index contrast n_H/n_L for HBFs with $2.0 \leq n_L \leq 2.5$ and $2.8 \leq n_H \leq 3.8$. N = 25, a = 500 μm, k = 0, and λ_o = 10.6 μm.....45

Figure II-17 Theoretical HE_{11} mode transmission loss for CO_2 laser radiation is plotted as a function of refractive index contrast n_H/n_L for HBFs with $2.0 \leq n_L \leq 2.5$ and $2.8 \leq n_H \leq 3.8$ for various numbers of layer pairs, N. a = 500 μm, k = 0, and λ_o = 10.6 μm. 47

Figure II-18 A Theoretical HE_{11} mode transmission loss for CO_2 laser radiation is plotted as a function of refractive index contrast n_H/n_L for HBFs with $2.0 \leq n_L \leq 2.5$ and $2.8 \leq n_H \leq 3.8$ for various extinction coefficients, k, of the layer pairs. a = 500 μm, N = 25, and λ_o = 10.6 μm. 48

Figure II-19 The theoretical HE_{11} mode transmission loss for CO_2 laser radiation is plotted as a function of the number of layer pairs, N, for a n_L = 2.4 / n_H = 3.2 HBF for various extinction coefficients, k, of the layer pairs. a = 500 μm and λ_o = 10.6 μm.....49

Figure II-20 The theoretical HE_{11} mode transmission loss for CO_2 laser radiation propagating in HBFs with $2.0 \leq n_L \leq 2.5$ and $2.8 \leq n_H \leq 3.8$ is plotted as a function of refractive index contrast n_H/n_L for various

magnitudes of error, σ/μ, in their layer thicknesses as measured by the standard deviation, σ, of each layer's thickness divided by it's optimum thickness, μ. a = 500 μm, N = 10, and λ_o = 10.6 μm. 51

Figure II-21 A schematic diagram of the axial (left) and longitudinal (right) cross sections of a metal (Ag) / dielectric (PS) coated HGW.....53

Figure II-22 The transmission loss for CO_2 laser radiation propagating in Ag/AgI coated HGWs is plotted as a function of their bore diameter, 2a. The red curve indicates the HE_{11} mode loss calculated using the ray optics method. The Miyagi-Kawakami impedance/admittance formulation is used to calculate the black curve. Black squares indicate experimental data. 53

Figure II-23 The refractive indices, n, of some metals commonly used as reflective coatings for HGWs are plotted as a function of wavelength. The values are calculated from each metal's Drude coefficients.....55

Figure II-24 The extinction coefficients, k, of some metals commonly used as reflective coatings for HGWs are plotted as a function of wavelength. The values are calculated from each metal's Drude coefficients.....56

Figure II-25 The theoretical HE_{11} mode transmission loss for CH_3OH laser radiation at 119 μm is plotted as a function of bore diameter for metal coated HGWs. Each curve represents a different metal commonly used in reflective coatings for HGWs. 58

Figure II-26 The theoretical HE_{11} mode transmission loss for CH_3OH laser radiation at 119 μm is plotted as a function of the metal layer thickness, d_{metal}, for metal coated HGWs. Each curve represents a

different metal commonly used in reflective coatings for HGWs. a = 900 μm. 58

Figure II-27 The theoretical HE_{11} mode transmission loss for CH_3OH laser radiation at 119 μm is plotted as a function of the refractive index of the dielectric film, n_d, for Ag/dielectric coated HGWs. Each curve is calculated assuming a different value for the extinction coefficient of the dielectric. a = 900 μm and λ_o = 119 μm. 60

Figure II-28 The optimum dielectric refractive index, n_d, for a Ag/dielectric coated HGW is plotted as a function of the dielectric's extinction coefficient k_d. 61

Figure II-29 The refractive index, n, of PS is plotted as a function of wavelength. 62

Figure II-30 The extinction coefficient, k, of PS is plotted as a function of wavelength. 62

Figure II-31 The theoretical HE_{11} mode transmission loss for CH_3OH laser radiation at 119 μm is plotted as a function of different polystyrene film thickness, d_d, for Ag/PS coated HGWs. a = 900 μm and λ_o = 119 μm. 64

Figure II-32 The theoretical HE_{11} mode transmission loss for CH_3OH laser radiation at 119 μm is plotted as a function of wavelength for Ag/PS coated HGWs. Each curve represents a different polystyrene film thickness d_d. a = 900 μm. 64

Figure II-33 The theoretical HE_{11} mode transmission loss for CH_3OH laser radiation at 119 μm propagating in silver/polystyrene coated HGWs is plotted as a function of the magnitude of error, σ/μ, in the PS layer thicknesses, as measured by the standard deviation σ of each layer's

thickness divided by it's optimum thickness. a = 900 μm and λ_o = 119 μm. 66

Figure II-34 The average reflectivity coefficient, R_{avg}, is plotted as a function of angle of incidence for the wall of a Ag-coated HGW, a Ag/AgI coated HGW, and the OmniGuide fiber with and without materials absorption. 67

Figure III-1 The glass forming difficulty of Ge-Se glasses is plotted as a function of Ge content. 78

Figure III-2 The refractive index of $Ge_{1-x}Se_x$ glasses is plotted as a function of x. 79

Figure III-3 The refractive indices of many chalcogenide glass compositions are plotted as a function of their density. 81

Figure III-4 The glass forming regions in the Ag-As-Se system. 83

Figure III-5 The glass transition temperature is indicated for several compositions in the Se deficient region of Ag-As-Se glass formation. 84

Figure III-6 The crystallization temperature is indicated for several compositions in the Se deficient region of Ag-As-Se glass formation. 84

Figure III-7 A schematic diagram of the distillation furnace used to purify Se before chalcogenide glass batching. 87

Figure III-8 A schematic diagram of the surface oxide removal furnace used to purify Ag and As before chalcogenide glass batching. 89

Figure III-9 A schematic diagram of the rocking furnace used to melt chalcogenide glasses. 91

Figure III-10 A digital photograph of an ampoule (upper) used to melt chalcogenide glass compositions and a Ag-As-Se glass slug (lower)..... 91

Figure III-11 A schematic diagram of the Nicolet Protégé 360 FTIR. 93

Figure III-12 The infrared transmission spectra of 3 mm thick chalcogenide glass samples. 94

Figure III-13 R_s, and R_p are plotted as a function of θ_0 for the interface between air and dielectrics with n = 2.8 (red curves) and n = 3.2 (blue curves). 96

Figure III-14 A schematic diagram of a variable angle reflectometer. 97

Figure III-15 The cross section of the VAR sample holder is shown schematically for each stage of the procedure used to align a chalcogenide glass sample. 98

Figure III-16 R_p is plotted a function of the angle of incidence of $Ag_{25}As_{40}Se_{35}$ glass. 99

Figure III-17 The refractive indices of Ag-As-Se glasses are indicated on a ternary diagram. 100

Figure III-18 A schematic diagram of a CO_2 laser calorimeter is shown.....103

Figure III-19 ΔT is plotted as a function of time for a 14.7 mm $Ag_{25}As_{40}Se_{35}$ glass rod irradiated with CO_2 laser radiation for 120 s. 104

Figure III-20 The transmission loss of the HE_{11} mode is plotted as a function of N for CO_2 laser radiation propagating in a As_2Se_3/PEI (red) Omniguide HBF and a $Ag_{25}As_{40}Se_{35}/Ge_{20}Se_{80}$ (blue) HBF. a = 350 μm and λ_o = 10.6 μm. 106

Figure III-21 A schematic diagram of the thermal evaporation set-up used to deposit chalcogenide glass films on the outside of a rotating aluminum tube. 110

Figure III-22 A schematic diagram of the front (left) and side (right) of the polymer cladding set-up used to consolidate PEI films to form a

protective coating for chalcogenide glass films deposited on the outside of and aluminum mandrel. 111

Figure III-23 A reflected light micrograph of the cross section of an aluminum substrate tube (a) with three layers; $As_{40}Se_{60}$ (b), $Ge_{20}Se_{80}$ (c), and $As_{40}Se_{60}$ (d) mounted in epoxy (e). 112

Figure III-24 A digital photograph of a hollow fiber preform consisting of a 1/4" inner diameter 1/16" wall thickness PEI tube with an inner $Ge_{20}Se_{80}$ coating. 113

Figure III-25 An optical micrograph of the cross section of a hollow PEI fiber with an inner $Ge_{20}Se_{80}$ coating. The fiber's inner and outer diameters are 200 μm and 460 μm, respectively. 113

Figure IV-1 The roughness of FCP films deposited on silver coated glass substrates as a function of coating velocity for various weight concentrations of the coating solution. 126

Figure IV-2 The thickness, *d*, of FCP films deposited on silver coated glass substrates as a function of square root of the coating velocity, $V^{1/2}$ for various weight concentrations of the coating solution. 126

Figure IV-3 Lines laid over the plot from Figure IV-1 illustrate the procedure for determining the coating velocities that produce films with roughness of 25 nm, 50 nm, and 85 nm for 5 wt. %, 7 wt. %, and 9 wt. % FCP solutions. 128

Figure IV-4 Constant roughness contours are laid over the plot from Figure IV-2. ... 128

Figure IV-5 The shear stress required to maintain a constant shear rate is plotted for a 25 wt. % PS/toluene solution. The slope of the solid line fit through the data is obtained by least squares regression and is equal to the viscosity, η. 131

Figure IV-6 The viscosity of FCP/perflourochemical and (red) and polystyrene/toluene (blue) solutions are plotted as a function of the concentration of the polymers measured in wt. %. 132

Figure IV-7 A schematic diagram of the apparatus used to deposit silver coatings via the electroless liquid phase chemical deposition (ELPCD) process. 136

Figure IV-8 A schematic diagram of the apparatus used to deposit polymer thin films by the liquid flow coating (LFC) process. 138

Figure IV-9 The measured coating velocity, *V*, is plotted a function of the revolution rate of the peristaltic pump head used draw PS/toluene solutions through 1.7 mm bore diameter Ag-coated HGWs..... 139

Figure IV-10 An optical micrograph of a 2.2 mm bore diameter Ag/PS HGW. 140

Figure IV-11 The infrared spectra of a 700 μm bore diameter, 1 m long, Ag–only HGW and Ag/COP HGW. 141

Figure IV-12 A schematic diagram of the FTIR spectroscopy set-up used to characterize Ag/PS HGWs. 143

Figure IV-13 The near infrared (NIR) spectra of 1.7 mm bore diameter Ag/PS HGWs with PS films deposited using various PS/toluene solution concentrations and coating rates. The vertical scale is offset for clarity. 144

Figure IV-14 The NIR absorption spectrum of a 1.7 mm bore diameter Ag/PS HGW (black) is compared to the absorption spectra of an Ag–only HGW (green), a free standing PS film (blue), and the calculated interference spectrum for a 7.7 μm thick polystyrene layer on silver (red). The vertical scale is offset for clarity. 147

Figure IV-15 The thickness, d_{PS}, of PS films is plotted as a function of the coating rate, $V^{1/2}$, for various concentrations of PS in toluene. Markers indicate measured data. Solid lines indicate the film thickness calculated from the empirical equation $d = 0.019 \cdot 10^{0.042 \cdot C} \cdot C \cdot \sqrt{V}$. 149

Figure IV-16 A schematic diagram of the SIFIR-50 CO_2 pumped CH_3OH laser system used to characterize Ag/PS HGWs. A thermopile detector is used for cutback loss measurements and a pyroelectric camera serves as the detector for mode profile measurements..... 150

Figure IV-17 A physical representation of the process by which a 9.69 μm photon is absorbed by a CH_3OH molecule resulting in the emission of a 119 μm photon. 151

Figure IV-18 The far-field spatial intensity variation of 119 μm radiation upon exiting 90 cm long 1.6 mm bore diameter Ag/PS HGWs. Images *a*, *b*, and *c* correspond to a waveguide with no PS film, whereas images *d*, *e*, and *f* correspond to a waveguide with a 10 μm PS film. Images *a* and *d* are obtained with a horizontal wire grid polarizer inserted between the output end of the waveguide and the camera. Images *c* and *f* are obtained using a vertical wire grid polarizer. 153

Figure IV-19 The far-field spatial intensity variations of 119 μm radiation upon exiting 90 cm long Ag/PS HGWs. The bore size, *a*, and PS film thickness, d_{PS}, of the HGW are given below each image. 154

Figure IV-20 Cut-back loss measurement data is shown for 119 μm radiation propagating in 1.7 mm bore diameter Ag/PS coated HGWs. The solid lines are linear fits to the data forced through the origin. 157

Figure IV-21 The measured transmission loss is plotted as a function of PS film thickness, d_{PS}, for 119 μm radiation propagating in 1.6 mm (blue),

1.7 mm (red), and 2.2 mm (green) bore diameter Ag/PS coated HGWs. 157

LIST OF TABLES

Table II-1 The values of the mode parameter u_{nm}. 14

Table II-2 The optical properties of some drawable materials. 41

Table II-3 The Drude parameters and optical constants of some metals. 55

Table II-4 Optimum metal thicknesses and HE_{11} mode loss for metal coated silica HGWs at 119 μm. 56

Table II-5 Experimental and calculated reflectivities of copper and silver at normal incidence for 512 μm radiation. 59

Table III-1 Absorption peaks of chalcogenide glasses 75

Table III-2 Density and thermal properties of Ag-As-Se glasses. 85

Table III-3 Selenium distillation heat treatment schedule 88

Table III-4 Ag and As SOR heat treatment schedule. 89

Table III-5 Glass melting heat treatment schedule. 91

Table III-6 Summary of FTIR results. 94

Table III-7 Inverse temperature coefficients of a type-T thermocouple for 0 °C to 400 °C. 103

Table III-8 A comparison of PVD techniques. 108

Table IV-1 Loss and coupling efficiency of Ag/PS HGWs 160

Table IV-2 Comparison of THz waveguides. 161

Chapter I Introduction

The primary goal of this study is to develop low loss waveguides for transmitting infrared (IR) to terahertz (THz) frequency radiation. It is difficult to fabricate core/clad optical fibers with low loss in this spectral range and this has motivated the development of hollow core waveguides (HCWs). This chapter reviews HCWs and some applications of IR and THz radiation. The chapter is concluded by describing the approach taken in this study to design and fabricate HCWs with low loss for IR and THz radiation.

Chapter I.A Background

Hollow core waveguides (HCWs) provide several advantages over solid core optical fibers because they transmit light in an air core. There are no Fresnel reflections from the end face of a HCW when radiation is coupled from free space into the air core, so they have low insertion loss. HCWs also have low non-linear effects, high laser damage threshold, and low materials absorption because most of the radiation they transmit is confined to the air core [1]. These advantages have lead to the use of HCWs in applications requiring the transmission of radiation at wavelengths where it is otherwise difficult to find materials that have the optical, thermal, and mechanical properties required for use in solid core fibers. This study focuses on the IR and THz spectrum, but HCWs have also been used to transmit ultraviolet and soft X-ray radiation [2-4].

There are two classifications of HCWs: attenuated total internal reflection (ATIR) waveguides and leaky-type HCWs. ATIR waveguides consist of a hollow core

surrounded by wall material with a refractive index, n, that is less than one for the transmitted wavelength [5-6]. ATIR waveguides guide light by total internal reflection in the same manner as the silica core/clad optical fibers used in the telecommunications industry. The spectral range where a material has $n < 1$ is called an anomalous dispersion region. In this region the extinction coefficient, k, is also high. Evanescent waves propagating in the wall material are attenuated due to the wall's high k, limiting the performance of ATIR guides. One example of an ATIR waveguide is the hollow sapphire fiber that transmits CO_2 laser radiation with a loss of approximately 0.5 dB/m [1].

The other type of HCW utilizes a highly reflective wall to confine light to the air core. Leaky modes propagate in these HCWs since the wall is not a perfect reflector, thus they are referred to as leaky-type HCWs. Increasing the wall's reflectivity increases the degree to which light is confined to the waveguide's air core, thus decreasing the attenuation of radiation propagating along its axis. Leaky-type HCWs can be divided into different categories based upon how the wall of the waveguide is designed to achieve high reflectivity. The most basic design is to use a smooth metal surface to form the inner wall of the waveguide [7-9]. This can be accomplished using a metal tube, or by depositing a metal film on the smooth inner surface of a glass or plastic tube. A dielectric layer is then added over the metal to provide enhanced reflectivity within specific wavelength ranges due to an interference effect [10-11]. These waveguides are called metal/dielectric HCWs. Multilayer metal/dielectric HCWs are fabricated by adding multiple dielectric layers over the metal to form an alternating high/low refractive index structure [12-13]. In the absence of materials absorption, roughness, and structural imperfections the transmission loss of these waveguides decreases exponentially as the

number of layer pairs increases [14]. For an infinite number of layer pairs radiation is completely confined to the air core and the metal is no longer necessary to achieve high reflectivity. A waveguide that consists of a hollow core surrounded by an alternating high/low refractive index dielectric structure with no metal layer is called a hollow Bragg fiber (HBF) [15]. Photonic crystal fibers (PCFs) utilize a two-dimensional periodic dielectric structure to confine light to the air core [16]. Also called holey-fibers, these waveguides generally consist of a series of air channels stretching along the length of the waveguide that are arranged in a hexagonal lattice. Several air holes are removed from the center of the waveguide to create a defect in which light can propagate with low loss. The seven types of HCWs and their refractive index profiles are shown schematically in **Figure I-1**.

Chapter I.B Applications of Infrared and THz Transmitting Waveguides

While IR waveguides have achieved widespread commercial application, only a handful of lab scale studies of THz waveguide applications have been conducted. Some applications of IR waveguides include laser surgery [17], printing / marking [18], cutting / welding [19], threat recognition and countermeasure [20], chemical and biological sensing [21], radiometry [22], and thermal imaging [23]. One of the challenges that remain in the development of IR waveguides is the fabrication of ultra low loss waveguides for the delivery of high power IR laser radiation.

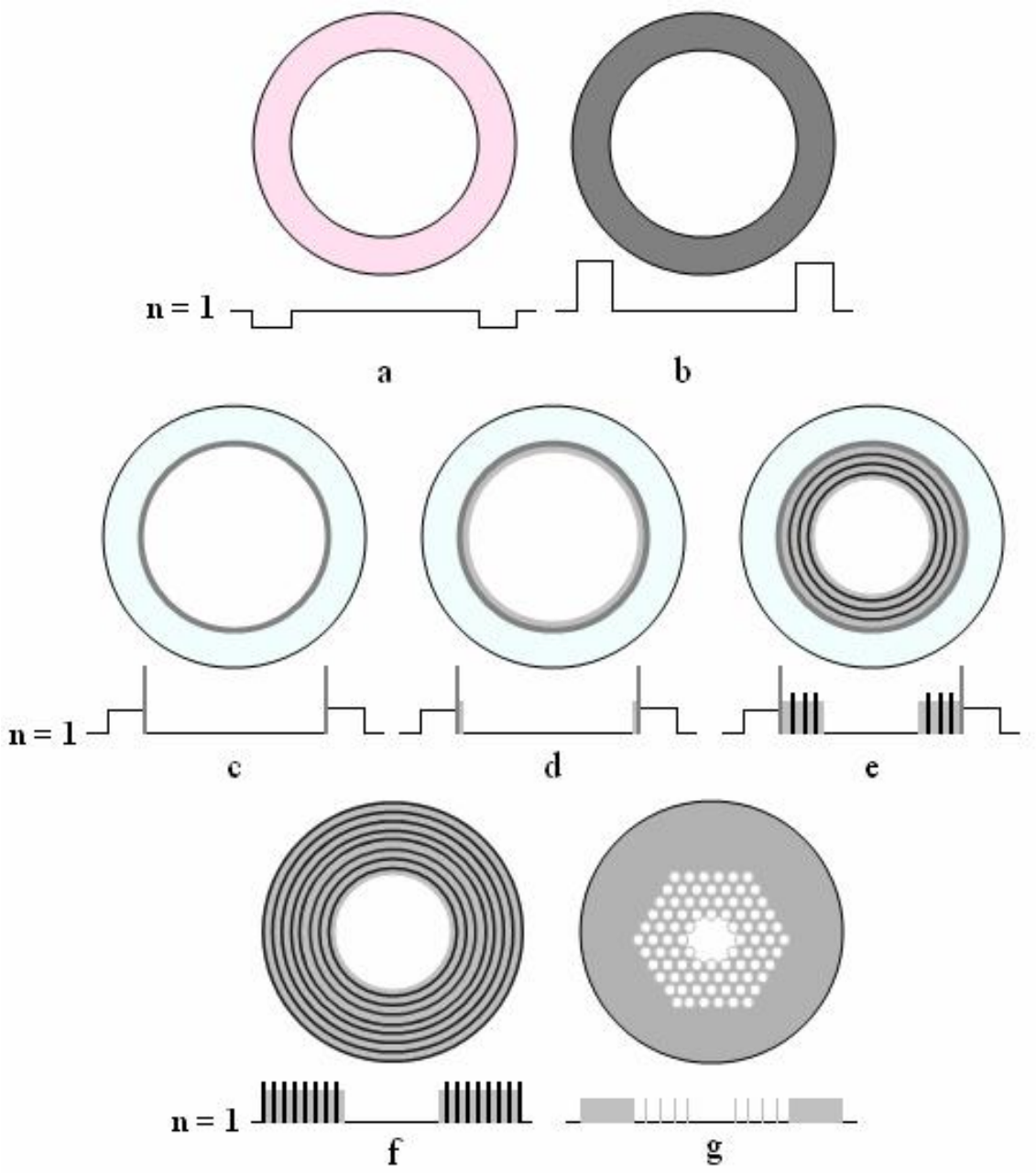

Figure I-1: Schematic cross sections and refractive index profiles of the seven types of hollow core waveguides: ATIR waveguide (a), metal tube (b), metal-coated hollow glass waveguide (HGW) or hollow polymer waveguide (HPW) (c), metal/dielectric HGW or HPW (d), multilayer metal/dielectric HGW or HPW (e), hollow Bragg fiber (HBF) (f), and photonic crystal fiber (g).

A Ag/AgI HGW has been used in conjunction with a water cooling jacket to deliver 2.6 kW CO_2 laser radiation with a wavelength of 10.6 μm [24]. This technology has yet to be adopted by industrial CO_2 laser delivery system manufacturers, despite its potential performance and cost benefits over the articulated arms and free space optics in use today. Reducing the transmission loss of the HCWs could be a driving force for their application in high power IR laser delivery systems. Single layer metal/dielectric waveguides are already fabricated with near theoretical loss for CO_2 laser radiation, so there is little room to improve their performance. George et al. have demonstrated lower losses by increasing the bore diameter of the HCW, but the mode quality of the waveguides is compromised [14]. Experimental observations and theoretical calculations indicate that the performance of multilayer metal/dielectric waveguides will be limited by the increase in roughness associated with increasing the number of dielectric layer pairs [13-14].

HBFs may have the most promise for CO_2 laser power delivery. The arsenic triselenide (As_2Se_3) glass/polyetherimide (PEI) HBF developed by MIT and commercialized by OmniGuide, Inc. is the first HBF to be used in CO_2 laser delivery for medical applications [25-28]. The OmniGuide HBF has a loss of 0.5 dB/m, which is significantly higher than the best Ag/AgI HCWs with losses as low as 0.017 dB/m [14]. The low loss of the OmniGuide HBF is remarkable because the loss of the low refractive index layer material, PEI, is on the order of 100,000 dB/m. Theoretical calculations indicate that the loss of an IR transmitting HBF could be reduced by several orders of magnitude simply by using lower loss materials [29].

The development of IR and THz waveguide technologies are at vastly different stages of maturity. THz radiation covers the spectral range from 100 μm to 3,000 μm (3 THz – 0.1 THz). Interest in THz radiation has grown considerably over the past ten years with the emergence of stronger transmitters and more sensitive receivers [30]. The unique interaction of THz radiation with matter, in particular gasses and materials that contain water, have led researchers to investigate applications in imaging and spectroscopy [31-33]. Molecules with similar chemical bonds can be difficult to distinguish using IR spectroscopy. The rotational transitions and associated THz absorption spectrum of molecules can be more readily distinguished. THz time domain spectroscopy (TDS) allows the rapid collection of an analyte's spectral response over the range of 0.1 THz to 3 THz. THz TDS spectroscopy is therefore a powerful tool in the chemical analysis of gasses and liquids.

It may be possible to achieve added functionality in systems utilizing THz radiation by incorporating low loss optical waveguides. For instance, a flexible waveguide could be coiled to create a small footprint, long path length cell for gas sensing using TDS. Many approaches have been taken to achieve low loss THz waveguides including photonic crystal fibers [34], hollow polymer fibers [35], metal tubes [8], Cu coated hollow polycarbonate waveguides (HPWs) [9], and metal wires [36]. With the exception of metal wires, all of these technologies have been adapted from IR transmitting waveguides. Taking this into consideration, it is interesting that the lowest loss IR wave guiding technology, the metal/dielectric HCW, has not yet been applied to fabricate THz waveguides.

Chapter I.C Approach and Organization of the Dissertation

The approach that we have used to study HCWs is similar for both IR and THz radiation. First the design of the waveguide is investigated theoretically. These calculations form a basis for the selection of materials for use in constructing the waveguide. Fabrication techniques that are capable of forming the selected materials into the proper structure are then developed.

The success of the OmniGuide HBF shows that its design principles are sound and that HBFs may be fabricated with precisely controlled microstructures. A shortcoming of the OmniGuide HBF is the high absorption of the materials from which it is made. This study seeks to build upon the Omniguide HBF technology by incorporating materials with low absorption into a waveguide with a similar design and using similar fabrication techniques. This effort requires the identification of two materials with high refractive index contrast (ratio of the high refractive index to the low refractive index), low extinction coefficient, and thermal properties that permit them to be co-drawn from a HBF preform. Chapter III details the efforts undertaken in this study to identify chalcogenide glasses that meet these three conditions for 10.6 μm radiation. The basic elements of a preform fabrication and drawing process to produce a chalcogenide glass HBF are also demonstrated.

The applications of THz radiation do not require the ultra low losses that are made possible by the complex structure of HBFs. Instead this study focuses on the application of the metal/dielectric HCW technology to THz waveguides. Theoretical calculations presented in Chapter II indicate that the simple, single dielectric-layer design may be

applied to THz radiation by increasing the dielectric film thickness in proportion to the wavelength of operation. This study focuses on 119 μm radiation because that is the strongest emission line of a Coherent SIFIR-50 laser that was available for use in these investigations through a collaboration with Oleg Mitrofanov at Alcatel-Lucent Bell Laboratories. The study did not require the synthesis of new materials because theoretical calculations indicate that the optical properties of silver and polystyrene (PS) should provide near minimum theoretical loss. Chapter IV describes the fabrication and characterization of Ag/PS HGWs for THz radiation.

The design studies for both IR and THz waveguides are presented in Chapter II. The materials selection and fabrication efforts for IR and THz waveguides are discussed separately in Chapters III and IV, respectively. Chapter V summarizes the work completed in this study and provides some perspective on future investigations that could be conducted.

Chapter I.D References

1. J. A. Harrington, *Infrared Fibers and Their Applications*, SPIE (2003).

2. Y. Matsuura, D. Akiyama, and M. Miyagi, "Beam homogenizer for hollow-fiber delivery system of excimer laser light," *Appl. Optics*, Vol. 42, No. 18, pp. 3505-3508 (2003).

3. H. S. Eckhardt, H. Dominick, M. Frank, K. T. Grattan, and K. Klein, "Gas analysis in the UV region: a hollow-core waveguide sensor system," *Proc. SPIE*, Vol. 5502, No. 1, pp. 267-270 (2004).

4. Y. Matsuura, T. Oyama, and M. Miyagi, "Soft-X-ray hollow fiber optics with inner metal coating," *Appl. Optics*, Vol. 44, No. 29, pp. 6193-6196 (2005).

5. M. Miyagi, "Consideration on realization of low-loss total reflection-type hollow-core fiber at mid-infrared," *Proc. SPIE*, Vol. 843, pp. 76-79 (1988).

6. J. A. Harrington and C. C. Gregory, "Hollow sapphire fibers for the delivery of CO_2 laser energy," *Opt, Lett.*, Vol. 15, pp. 541-543 (1990).

7. E. Garmire, T. McMahon, and M. Bass, "Flexible infrared waveguides for high-power transmission," *IEEE J. Quantum Electron.*, Vol. QE-16, pp.23-32 (1980).

8. G. Gallot, S. P. Jamison, R. W. McGowan, and D. Grischkowsky, "Terahertz waveguides," *J. Opt. Soc. Am. B*, Vol. 17**,** pp. 851-863 (2000).

9. J. A. Harrington, R. George, P. Pedersen, and E. Mueller, "Hollow polycarbonate waveguides with inner Cu coatings for delivery of terahertz radiation," *Opt. Express*, Vol. 12, pp. 5263-5268 (2004).

10. Y. Matsuura, T. Abel, and J.A. Harrington, "Optical properties of small-bore hollow glass waveguides," *Appl. Optics*, Vol. 34, pp. 6842-6847 (1995).

11. R. George and J. A. Harrington, "Infrared transmissive, hollow plastic waveguides with inner Ag-AgI coatings," *Appl. Optics*, Vol. 44, No. 30, pp. 6449-6455 (2005).

12. V. Gopal, “New dielectric coatings for low-loss hollow glass waveguides and bundles,” Ph.D. Thesis, Rutgers University (2003).

13. Y. Matsuura and J. A. Harrington, “Hollow glass waveguides with three-layer dielectric coating fabricated by chemical vapor deposition,” *J. Opt. Soc. Am. A*, Vol. 14, pp. 1255-1259 (1997).

14. R. George, "New dielectric thin film coatings for Ag and Cu coated hollow infrared waveguides," Ph.D. Thesis, *Rutgers University*, (2004).

15. Yeh, A. Yariv, and E. Marom, “Theory of Bragg Fiber,” *J. Opt. Soc. Am.*, Vol. 68, No. 9, pp. 1196-1201 (1978).

16. G. J. Pearce, J.M. Pottage, D.M. Bird, P.J. Roberts, J.C. Knight, P. St.J. Russell, “Hollow-core PCF for guidance in the mid to far infra-red,” *Opt. Express*, Vol. 13, No. 18, pp. 6937-6946 (2005).

17. I. Gannot, A. Inberg, M. Oksman, R. Waynant, N. Croitoru, “Current status of flexible waveguides for IR laser radiation transmission,” *IEEE J. Sel. Top. Quant.*, Vol. 2, No. 4, pp. 880-889 (1996).

18. D. Beu-Zion, A. Inberg, N. Croitoru, S. Shalem, A. Katzir, “Hollow glass waveguides and silver halide fibers as scanning elements for CO_2 laser marking systems,” *Opt. Eng*., Vol. 39, No. 5, pp. 1384-1390 (2000).

19. W. Penn, “Trends in laser material processing for cutting, welding, and metal deposition using carbon dioxide, direct diode, and fiber lasers” *Proc. SPIE*, Vol. 5706, pp. 25-37 (2005).

20. J.S. Sanghera, I.D. Aggarwal, L.D. Busse, P.C. Pureza, V. Q. Nguyen, L.B. Shaw, F. Chenard, “Chalcogenide optical fibers target mid-IR applications,” *Laser Focus World*, Vol. 41, No. 4, pp. 83-87 (2005).

21. R. Kellner, R. Gobel, R. Gotz, B. Lendl, B. Edl-Mizaikoff, M. Tacke, A. Katzir, “Recent progress on mid-IR sensing with optical fibers” *Proc. SPIE*, Vol. 2508, pp. 212-223 (1995).

22. D. C. Tran, K.H. Levin, R. Mossadegh, S. Koontz, “IR fiber temperature sensing system,**”** *Proc. SPIE*, Vol. 843, pp. 148-154 (1988).

23. I. Gannot, A. Goren, E. Rave, A. Katzir, V. Gopal, G. Revezin, J. A. Harrington, "Thermal imaging through infrared fiber/waveguides bundles," *Proc. SPIE*, Vol. 5317, No. 1, pp. 94-100 (2004).

24. A. Hongo, K. Morosawa, K. Matsumoto, T. Shiota, and T. Hashimoto, "Transmission of kilowatt-class CO_2 laser light through dielectric-coated metallic hollow waveguides for materials processing," *App. Opt.*, Vol. 31, pp. 5514-5120 (1992).

25. B. Temelkuran, S. D. Hart, G. Benoit, J.D. Joannopoulos, Y. Fink, "Wavelength-scalable hollow optical fibres with large photonic band gaps for CO_2 laser transmission", *Nature*, Vol. 420, pp. 650-653 (2002).

26. C. Anastassiou, G. Dellemann, O. Weisberg, and U. Kolodny, "Fibers deliver CO_2 laser beams for medical applications," *Photon. Spectra*, Vol. 38, No. 3, pp. 108-109 (2004).

27. L. P. Tate Jr. and Y. A. Elce, "Transedoscopic application of CO_2 laser irradiation using the OmniGuide fiber," *Proc. SPIE*, Vol. 5686, No. 1, pp. 612-619 (2005).

28. D. Torres, O. Weisburg, G. Shapira, C. Anastassiou, B. Temelkuran, M. Shurgalin, S. A. Jacobs, R. U. Ahmad, T. Wang, U. Kolodny, S. M. Shapshay, Z. Wang, A. K. Devaiah, U. D. Upadhyay, J. A. Koufman, "OmniGuide photonic bandgap fibers for delivery of CO_2 laser energy for laryngeal and airway surgery," *Proc. SPIE*, Vol. 5686, No. 1, pp. 310-321 (2005).

29. S. Johnson, M. Ibanescu, M. Skorobogatiy, O. Weisberg, T. Engeness, M. Soljacic, S. Jacobs, J. Joannopoulos, Y. Fink, "Low-loss asymptotically single-mode propagation in large-core OmniGuide fibers," *Opt. Express*, Vol. 9, No. 13, pp. 748-779 (2001).

30. D. Mittleman, ed., *Sensing with Terahertz Radiation*, Springer (2003).

31. Dragoman and M. Dragoman, "Terahertz fields and applications," *Prog. Quant. Electron.*, Vol. 28, pp. 1-66 (2004).

32. J. Zhang and D. Grischkowsky, "Waveguide terahertz time-domain spectroscopy of nanometer water layers," *Opt. Lett.*, Vol. 29, No. 14, pp. 1617-1619 (2004).

33. H. Kurt, D. S. Citrin, D.S. “Photonic crystals for biochemical sensing in the terahertz region,” *Appl. Phys. Lett.*, Vol. 87, No. 4, pp. 41108-1 - 411081-3 (2005).

34. H. Han, H. Park, M. Cho, and J. Kim, “Terahertz pulse propagation in a plastic photonic crystal fiber,” *Appl. Phys. Lett.*, Vol. 80, pp. 2634-2636 (2002).

35. T. Hidaka, H. Minamide, H. Ito, S. Maeta, and T. Akiyama, "Ferroelectric PVDF cladding terahertz waveguide," *Proc. SPIE*, Vol. 5135, pp. 70-77 (2003).

36. J. Deibel, K. Wang, M. Escarra, and D. Mittleman, “Enhanced coupling of terahertz radiation to cylindrical wire waveguides,” *Opt. Express*, Vol. 14, pp. 279-290 (2006).

Chapter II Design of Hollow Core Waveguides

II.A Background

This study focuses on leaky-type hollow core waveguides (HCWs) that consist of a low refractive index core, for example air, surrounded by a higher refractive index reflective wall. The design of the HCW's reflective wall has evolved over time. Initially, researchers focused on metallic tubes with circular or rectangular cross-sections [1]. Marcatili and Schmeltzer (MS) solved Maxwell's equations for electromagnetic (EM) radiation propagating in air-core cylindrical waveguides under the assumptions that the bore size is much larger than the wavelength and the propagation constant, β_{lm}, is approximately equal to the wavevector, k [2]. The dependence of the modal power attenuation constants (henceforth referred to simply as loss), α_{nm}, on the wall's complex refractive index, $\tilde{n}$, are given by

$$\alpha_{lm} = 2 \cdot \left(\frac{u_{nm}}{2 \cdot \pi} \right)^2 \cdot \frac{\lambda^2}{a^3} \operatorname{Re}\left\{ \begin{array}{ll} \dfrac{1}{\sqrt{\tilde{n}^2 - 1}}, & \text{for } \mathrm{TE}_{0\mathrm{m}} \text{ modes} \\ \dfrac{\tilde{n}^2}{\sqrt{\tilde{n}^2 - 1}}, & \text{for } \mathrm{TM}_{0\mathrm{m}} \text{ modes} \\ \dfrac{\tilde{n}^2 + 1}{2 \cdot \sqrt{\tilde{n}^2 - 1}}, & \text{for } \mathrm{HE}_{\mathrm{nm}} \text{ modes} \end{array} \right\} \qquad \text{Eq.(II.1)}$$

where λ is the wavelength, a is the radius of the air core, and u_{nm} is the mode parameter. The values of u_{nm} for the lowest order modes are given in **Table II-1**. The practical implication of Eq.(II.1) is that low loss waveguides can be realized by coupling radiation to the lowest order modes, those with small u_{nm}, with large bore radius waveguides. This principle is true for all leaky-type HCWs. There are two issues with metallic HCWs that

limit their usefulness: the lowest loss mode is the TE_{01} mode, which cannot be coupled efficiently to the TEM_{00} output of laser sources, and there is a significant increase in loss when these waveguides are bent. MS showed that this increase in loss on bending is proportional to $1/R^2$, where R is the bend radius, for large bend radii.

m / n	1	2	3	4
0	3.8317	7.0156	10.1735	13.3237
1	2.4048	5.5201	8.6537	11.7915
2	3.8317	7.0156	10.1735	13.3237
3	5.1356	8.4172	11.6198	14.7960
4	6.3802	9.7610	13.0152	16.2235

Table II-1: The values of the mode parameter u_{nm}.

The next step in the evolution of HCW design was the realization that one or more dielectric layers deposited over a metallic substrate tube could greatly enhance its reflectivity and, thus, lower the waveguide's losses [3,4]. Miyagi and Kawaki (MK) characterized the transmission modes of these hybrid metal/dielectric HCWs by their surface impedance and admittance and developed an expression for the modal loss as,

$$\alpha_{lm} = 2 \cdot \left(\frac{u_{nm}}{2 \cdot \pi} \right)^2 \cdot \frac{\lambda^2}{a^3} \cdot \left(\frac{n}{n^2 + k^2} \right) \cdot F_{film} \qquad \text{Eq.(II.2)}$$

where n and k are the refractive index and extinction coefficient of the metal ($\tilde{n} = n - i \cdot k$). MS and MK theories predict the same dependences of the modal loss on the mode

parameter, wavelength, and bore size. A significant difference between the two equations is the inclusion of the term F_{film} that describes the loss reduction upon the addition of a dielectric film given by

$$F_{film} = \left\{ \begin{array}{ll} 1 + \dfrac{n_d^{\,2}}{\sqrt{n_d^{\,2} - 1}}, & \text{for } \mathrm{TE}_{0m} \text{ modes} \\ \dfrac{n_d^{\,2}}{\sqrt{n_d^{\,2} - 1}} \cdot \left(1 + \dfrac{n_d^{\,2}}{\sqrt{n_d^{\,2} - 1}} \right), & \text{for } \mathrm{TM}_{0m} \text{ modes} \\ \dfrac{1}{2} \cdot \left(1 + \dfrac{n_d^{\,2}}{\sqrt{n_d^{\,2} - 1}} \right), & \text{for } \mathrm{HE}_{nm} \text{ modes} \end{array} \right\} \qquad \text{Eq.(II.3)}$$

where n_d is the refractive index of the dielectric, which is assumed to be lossless, i.e. $\tilde{n}_d = n_d - i \cdot 0$. The loss of the hybrid modes is minimized when n_d is equal to 1.41. The bend loss for small bend radii was described by MK and shown to be proportional to $1/R$ [5]. The transition from the large bend radius behavior described by MS to the MK small bend radius behavior occurs at the critical bend radius where radiation couples to whispering gallery modes. MK also indicate that the loss of hybrid metal/dielectric waveguides can be decreased by adding additional quarter wave thickness dielectric layers in an alternating high refractive index, n_H, / low refractive index, n_L, configuration. The intensity of the EM fields penetrating into the metal decreases exponentially as more dielectric layers are added over the metal surface. If a sufficient number of dielectric layer pairs are added, the metal can be removed without increasing the loss significantly. Such a fiber is the hollow Bragg fiber (HBF) first described by Yeh and Yariv [6].

HBFs consist of an air core surrounded by alternating quarter wave thickness n_L and n_H layers. HBFs support similar TE, TM, and HE modes to those that propagate in metallic HCWs. Three analysis methods have been employed to determine the complex

propagation constants of the modes in HBFs: the transfer matrix method [6,7], the asymptotic method [8,9], and the Galerkin method [10,11]. A key result of these studies has been the identification of the refractive index contrast (n_H/n_L) as a key design parameter for HBFs. High refractive index contrast reduces the number of layers needed to provide low loss; increases the materials absorption suppression (ratio of the materials absorption to the fiber's transmission loss); and allows for omnidirectional reflection [12,13] where light of any polarization state and angle of incidence is perfectly reflected from the waveguide's wall. The implications of omnidirectional reflection are discussed in more detail in Section II.G-3.

Miyagi's ray optical treatment [14] of the modal loss in HCWs is far less complex than any of the above mentioned analysis techniques yet provides the flexibility to analyze the modal loss characteristics of any leaky-type HCW. The basic approach is to determine the incidence angles corresponding to the propagation constants of each mode; calculate the reflectivity of the waveguide's wall for the mode's polarization state and angle of incidence; and then determine the loss of radiation traveling in a given mode based on the distance each wavefront travels between interactions with the wall and how much intensity is lost with each interaction. The calculation of the reflectivity coefficients of multilayer thin films is thoroughly described in several texts [15,16] and there are many optical thin film analysis software packages available, making ray optics calculations easy to employ. The accuracy of the ray optics formulation has been verified in a number of studies [17,18]. One drawback of ray optics calculations is that they are limited to analysis of the modal loss, whereas the wave optics methods can provide information about both the attenuation and dispersion of the modes.

This study is concerned primarily with the identification of materials and fabrication techniques for HCWs that transmit infrared to THz laser power. The ray optics method is an excellent tool for evaluating HCW designs for these applications because it provides accurate modal attenuation constants and its results are easy to obtain and interpret.

II.B Ray Optics Calculations for Hollow Core Waveguides

An optical ray coupled into a HCW within a plane intersecting the center of the waveguide's cross section is called a meridional ray. Meridional rays are guided in the waveguide's core via successive reflections at an angle θ_z measured from the ray to the normal of the reflective wall. The distance between consecutive reflections, L, is given by the equation

$$L = 2 \cdot a \cdot \tan(\theta_z) \qquad \text{Eq.(II.4)}$$

where a is the radius of the waveguide's core. The propagation of a meridional ray in a HCW is shown schematically in **Figure II-1**. If the wall of the waveguide is not a perfect reflector there will be some loss of intensity each time the ray is incident upon the wall. Neglecting any reduction in loss due to the Goos-Hänchen shift, the power attenuation coefficient, or simply loss, α, is given by the equation

$$\alpha = \frac{1-R}{L} = \frac{1-R}{2 \cdot a \cdot \tan(\theta_z)} \qquad \text{Eq.(II.5)}$$

where R is the polarization specific reflectance of the wall. When the orientation of the electric field of the light ray is parallel to the plane in which it is traveling (the plane of incidence) the light is said to be p-polarized and the parallel reflectance, R_p, is substituted

for R in Eq.(II.5). When the orientation of the electric field is perpendicular to the plane in which the ray is traveling the light is s-polarized and the perpendicular reflectance, R_s, is used. If the light is unpolarized the average reflectance, R_{avg}, is substituted for R in Eq.(II.5). R_{avg} is given by

$$R_{avg} = \frac{R_p + R_s}{2} \qquad \text{Eq.(II.6)}$$

The calculation of reflectance is discussed in Section II.D.

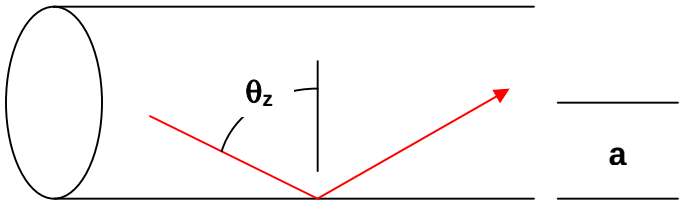

Figure II-1: A schematic diagram of a hollow core waveguide that indicates the bore radius, a, and mode angle, Θ_z.

II.C Modes in Hollow Core Waveguides

Ray optics is a useful tool for understanding the attenuation characteristics of optical waveguides, but does not provide a complete description of the light's propagation. An electromagnetic analysis, in which each ray is associated with a transverse electromagnetic (TEM) plane wave, can be used to understand light propagation in hollow core waveguides in more detail [19]. The sum of plane waves associated with each ray determines the electromagnetic field in the waveguide. It is instructive to first examine the case of a waveguide consisting of two planar infinite lossless mirrors in the x-y plane separated by a lossless dielectric of thickness, $2 \cdot a$, and

refractive index, *n*, as shown in **Figure II-2**. A monochromatic TEM plane wave propagating in the *y*-*z* plane at an angle, θ_z, is guided in the *z* direction without loss. This wave has a wavelength $\lambda = \lambda_o / n$, wavenumber $k = n \cdot k_o$, and phase velocity $c = c_o / n$. The TEM wave is reproduced after every other bounce when its bounce angle satisfies the equation

$$\theta_z = \theta_m = \cos^{-1}\left(m \cdot \frac{\lambda}{4 \cdot a} \right) \qquad \text{Eq.(II.7)}$$

where *m* is an integer and θ_m is the mode angle corresponding to *m*. There are only two distinct plane waves propagating in the waveguide when Eq.(II.7) is satisfied. The superposition of these two waves results in a field distribution across the waveguide's cross section (the *x*-*y* plane) that does not change with *z*. Such fields are called the modes of the waveguide. The modes are called transverse-electric (TE) modes when the TEM waves are polarized in the *x* direction (the electric field is parallel to the mirrors). The modes are referred to as transverse-magnetic (TM) modes when the TEM waves are polarized in the *y*-*z* plane (the magnetic field is parallel to the mirrors). The value of *m* is used as a subscript to distinguish between individual TE and TM modes, for instance, TE_1, designates the TE mode for $m = 1$.

Hollow core waveguides consisting of cylindrical lossless dielectric core of radius, *a*, and refractive index, n_0, surrounded by a perfectly reflecting mirror confine light in two dimensions and support radially symmetric TE and TM modes and hybrid HE and EH modes. Both the electric and magnetic fields of the hybrid modes have transverse components. The bounce angles corresponding to the modes propagating in cylindrical hollow core waveguides are given by [14]

$$\theta_z = \cos^{-1}\left(\frac{\lambda_0 \cdot u_{nm}}{2 \cdot \pi \cdot n_0 \cdot a}\right) \qquad \text{Eq.(II.8)}$$

where u_{nm} is the mode parameter of the nm^{th} mode and λ_0 is the freespace wavelength of the radiation propagating in the waveguide's core. The value of u_{nm} is equal to the m^{th} root of the $J_{n-1}(x)$ Bessel function. The HE_{11} mode angles for 10.6 μm and 119 μm radiation are plotted as a function of bore diameter in **Figure II-3**. Combining Eq.(II.5) and Eq.(II.8) yields an equation that can be used to calculate the modal attenuation constants:

$$2\alpha_{nm} = \frac{1-R}{2 \cdot a \cdot \tan\left(\cos^{-1}\left(\frac{\lambda_0 \cdot u_{nm}}{2 \cdot \pi \cdot n_0 \cdot a}\right)\right)} \qquad \text{Eq.(II.9)}$$

where $R = R_s$ for TE modes, $R = R_p$ for TM modes, and $R = R_{avg}$ for HE and EH modes.

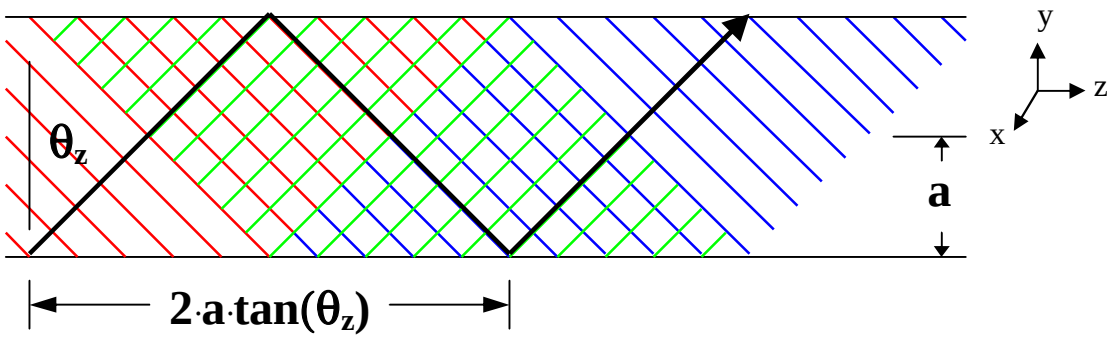

Figure II-2: A TEM plane wave propagating between two planar mirrors that satisfies the condition of self-consistency. The wavefronts of the initial plane wave, reflected plane wave, and twice reflected plane wave are shown in red, green, and blue, respectively. The diamond shaped pattern formed by the intersection of the wavefronts is analogous to a waveguide mode.

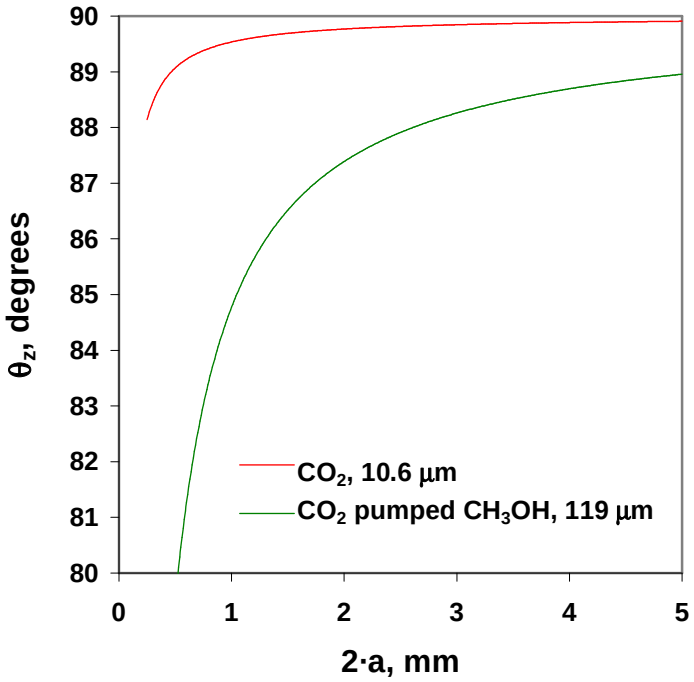

Figure II-3: The HE_{11} mode angle, θ_z, is plotted as a function of bore diameter $2 \cdot a$ for HCWs transmitting CO_2 laser infrared radiation at 10.6 μm and CO_2 pumped CH_3OH THz radiation at 119 μm.

II.D Coupling to the HE_{11} Mode

Commercially available laser sources operating in the infrared to THz spectral range are commonly designed to emit a TEM_{00} linearly polarized Gaussian beam, henceforth referred to as a TEM_{00} beam. Of the modes supported by HCWs, the HE_{11} most closely matches the intensity distribution and polarization of the TEM_{00} beam. Therefore the radiation from a laser that emits a TEM_{00} beam can be coupled most efficiently to the HE_{11} mode of a HCW. The relative electric field distribution of the TEM_{00} beam is given by:

$$\frac{E(r)}{E_0} = e^{-r^2/\omega^2} \qquad \text{Eq.(II.10)}$$

where r is the radial distance measured from the center of the mode, ω is half the beam diameter of the TEM_{00} beam taken as the value of r where $E(r)/E_0$ is equal to $1/e$. The relative electric field distribution of the HE_{11} mode in the core ($0 < r < a$) of a HCW with a circular cross section is given by

$$\frac{E(r)}{E_0} = J_0\left(\frac{u_{11} \cdot r}{a}\right) \qquad \text{Eq.(II.11)}$$

The axial variations of the relative intensity, $I(r)/I_0 \propto \left(E(r)/E_0\right)^2$, for the HE_{11} mode in a HCW of bore radius, a, and the TEM_{00} beam with a beam radius $\omega = 0.64 \cdot a$ are plotted in **Figure II-4**. The optimum coupling efficiency from the TEM_{00} beam to the HE_{11} waveguide mode is 98% and is achieved when $\omega/a = 0.64$ [20]. The total loss of the waveguide depends on the coupling efficiency and the characteristic loss of each mode. Thus the insertion loss is not necessarily minimized under the condition of optimum coupling to the HE_{11} mode, particularly for short waveguides. Nubling and Harrington show that for 1 m long Ag/AgI HGWs the minimum insertion loss for 10.6 μm CO_2 laser radiation is achieved for values of ω/a that are slightly less than 0.64 [20].

It is fortunate that the TEM_{00} beam is coupled most efficiently to the HE_{11} HCW mode because it is the lowest loss mode for the HGWs and HBFs examined in this study. Referring to Eq.(II.8) it is clear that higher order modes (high u_{nm}) have lower θ_z, which results in increased loss due to a shorter length per bounce and lower reflectance. Since the TEM_{00} beam can be coupled most efficiently to the HE_{11} mode, which is also the lowest loss mode of HCWs, the remainder of this study focuses on the transmission losses of the HE_{11} mode exclusively.

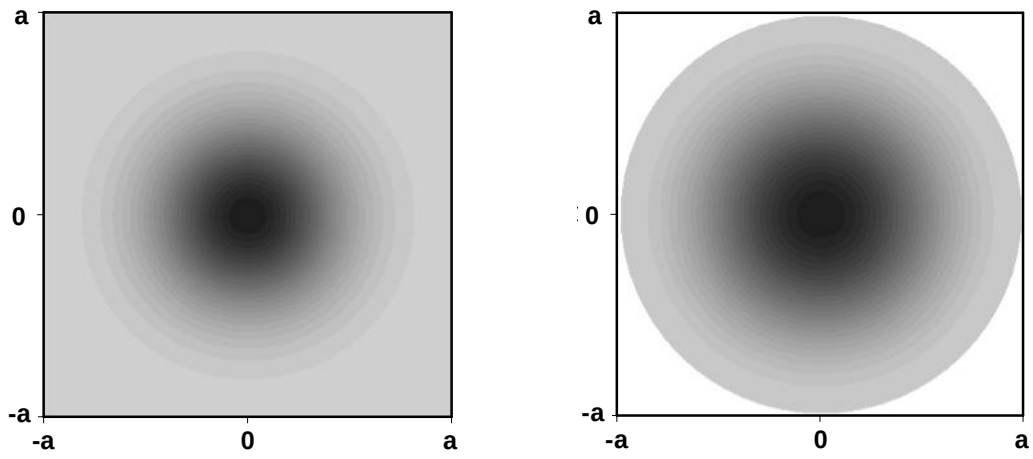

(a) (b)

Figure II-4: The relative intensity distributions of the TEM_{00} Gaussian beam (a) with beam diameter, $\omega = 0.64 \cdot a$, and the HE_{11} mode (b) propagating in a HCW with bore diameter, a. The darkest regions correspond to the greatest intensities.

II.E Calculation of Reflectivity Coefficients

There are several methods that may be employed to determine the reflectance of the HCW wall. George [21] has applied Rouard's [15] method. The calculation is initiated by replacing the outermost layer of the wall with a single surface having the same Fresnel coefficient and phase shift. Rouard's method proceeds by similar replacement of the layers in order from the outermost layer to the layer nearest the core until all layers have been replaced by a single surface. The Fresnel coefficient of this surface is equal to that of the collection of thin films that make up the HCW wall. There are also two matrix methods that are often employed to calculate the reflectance of a HCW wall. The transfer matrix method relates the positive going and negative going electric field vectors in successive layers to a 2 X 2 transfer matrix [22]. The elements of

the transfer matrix for each film are determined using Abele's equations for the electric field vectors in successive layers expressed in terms of their Fresnel coefficients [15]. The reflectivity coefficients of the system of layers are related to the product of the transfer matrices for each layer. In this study, the reflectivity of the HCW's wall is determined using a variation of the transfer matrix method in which the tangential components of the electric and magnetic field vectors at adjacent interfaces are related by another 2 X 2 matrix. In this case, the elements of the matrix are determined by expressing the tangential components of the electric and magnetic field vectors in terms of the characteristic admittance of each layer [16]. In a similar fashion to the transfer matrix method, the matrix associated with each film is multiplied together to obtain the characteristic matrix of the system allowing the determination of the reflectance. This method is discussed in detail below.

Consider a plane wave incident from a medium with a complex refractive index, $\tilde{n}_0 = n_0 - i \cdot k_0$, onto a multilayer thin film at an angle, θ_z, consisting of *J* layers with complex refractive indices, $\tilde{n}_j = n_j - i \cdot k_j$, supported by a substrate with a complex refractive index $\tilde{n}_s = n_s - i \cdot k_s$ as shown in **Figure II-5**. The subscript *j* takes on a value between 1, for the film nearest the incident medium, and *J*, for the film nearest the substrate. The coordinate system is chosen such that the layers are parallel to the y-axis and perpendicular to the z-axis. The tangential components of the plane wave's electric and magnetic vectors, E_{tan} and H_{tan}, are continuous at the interface between each layer.

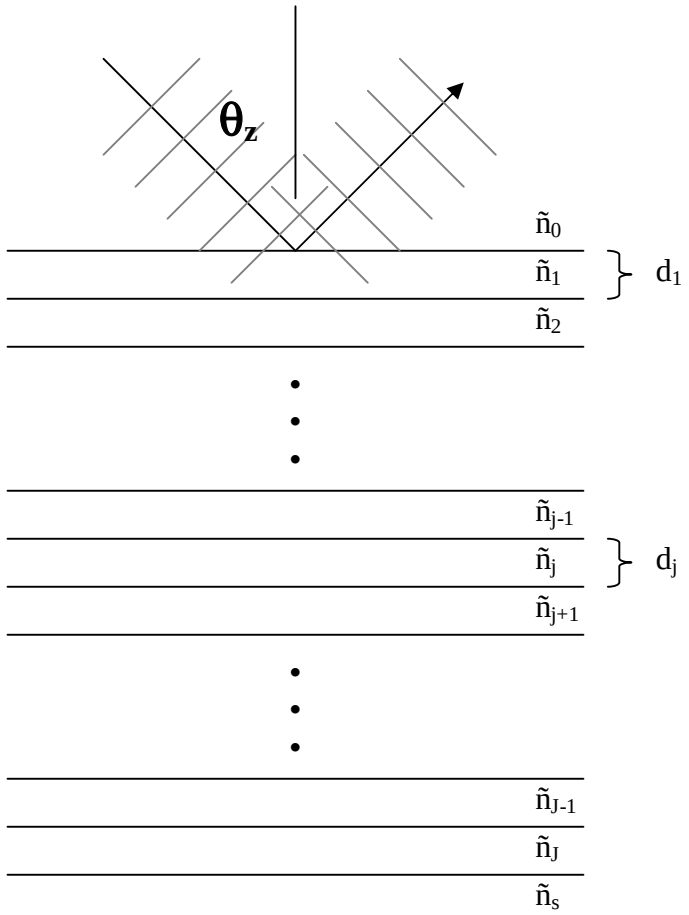

Figure II-5: A schematic diagram of a plane wave incident on a multilayer thin film.

The ratio $E_{\tan}/H_{\tan}$ thus varies continuously and is related to the optical impedance, *Z*, and admittance, *Y*, by

$$Z = \frac{1}{Y} = \frac{E_{\tan}}{H_{\tan}} \qquad \text{Eq.(II.13)}$$

The reflectance of the system is given by

$$R = \left(\frac{\eta_0 - Y}{\eta_0 + Y}\right) \cdot \left(\frac{\eta_0 - Y}{\eta_0 + Y}\right)^* \qquad \text{Eq.(II.14)}$$

where η_0 is the polarization specific characteristic admittance of the incident medium, and *Y* is the polarization-specific characteristic admittance of the system of thin films and

substrate. η_0 is given by,

$$\eta_0 = \tilde{n}_0 \cdot \cos(\theta_z) \qquad \text{Eq.(II.15)}$$

for s-polarization and is given by,

$$\eta_0 = \frac{\tilde{n}_0}{\cos(\theta_z)} \qquad \text{Eq.(II.16)}$$

for p-polarization. To determine the admittance of the system it is first necessary to determine the relationship between the tangential components of the electric and magnetic vectors at the two interfaces associated with any layer *j*. This relationship can be represented in matrix form:

$$\begin{pmatrix} E_{j-1} \\ H_{j-1} \end{pmatrix} = \begin{pmatrix} \cos\delta_j & i \cdot \frac{\sin\delta_j}{\eta_j} \\ i \cdot \eta_j \cdot \sin\delta_j & \cos\delta_j \end{pmatrix} \cdot \begin{pmatrix} E_j \\ H_j \end{pmatrix} \qquad \text{Eq.(II.17)}$$

where E_{j-1} and H_{j-1} are the tangential components of the electric and magnetic field vectors at the interface between layer *j* and layer *j-1*, E_j and H_j are the tangential components of the electric and magnetic vectors at the interface between layer *j* and layer *j+1*, δ_j is the optical phase shift associated with layer *j*, and η_j is the polarization specific characteristic impedance of layer *j*. δ_j is given by,

$$\delta_j = \frac{2 \cdot \pi \cdot d_r \cdot \sqrt{\tilde{n}_r^{\,2} - \tilde{n}_0^{\,2} \cdot \sin(\theta_z)}}{\lambda}. \qquad \text{Eq.(II.18)}$$

η_j is given by,

$$\eta_j = \sqrt{\tilde{n}_r^{\,2} - \tilde{n}_0^{\,2} \cdot (\sin(\theta_z))^2} \qquad \text{Eq.(II.19)}$$

for s-polarization and;

$$\eta_j = \frac{\tilde{n}_r^{\,2}}{\sqrt{\tilde{n}_r^{\,2} - \tilde{n}_0^{\,2} \cdot \sin(\theta_z)^2}} \qquad \text{Eq.(II.20)}$$

for p-polarization. The matrix:

$$(M_j) \equiv \begin{pmatrix} \cos\delta_j & i \cdot \frac{\sin\delta_j}{\eta_j} \\ i \cdot \eta_j \cdot \sin\delta_j & \cos\delta_j \end{pmatrix} \qquad \text{Eq.(II.21)}$$

is called the characteristic matrix of the thin film *j*. The tangential components of the electric and magnetic field vectors at any two interfaces can be determined by multiplying the characteristic matrices of all of the layers separating them. Thus the E_0 and H_0 are related to E_J and H_J by

$$\begin{pmatrix} E_0 \\ H_0 \end{pmatrix} = \prod_{j=0}^{J} \begin{pmatrix} \cos\delta_j & i \cdot \frac{\sin\delta_j}{\eta_j} \\ i \cdot \eta_j \cdot \sin\delta_j & \cos\delta_j \end{pmatrix} \cdot \begin{pmatrix} 1 \\ \eta_s \end{pmatrix} \cdot \begin{pmatrix} E_J \\ H_J \end{pmatrix} \qquad \text{Eq.(II.22)}$$

where η_s is the characteristic admittance of the substrate given by

$$\eta_s = \sqrt{\tilde{n}_s^{\,2} - \tilde{n}_0^{\,2} \cdot (\sin(\theta_z))^2} \qquad \text{Eq.(II.23)}$$

for s-polarization and

$$\eta_s = \frac{\tilde{n}_s^{\,2}}{\sqrt{\tilde{n}_s^{\,2} - \tilde{n}_0^{\,2} \cdot \sin(\theta_z)^2}} \qquad \text{Eq.(II.24)}$$

for p-polarization. The characteristic matrix of the film and substrate assembly is then given by

$$\begin{pmatrix} B \\ C \end{pmatrix} = \prod_{j=0}^{J} \begin{pmatrix} \cos\delta_j & i \cdot \frac{\sin\delta_j}{\eta_j} \\ i \cdot \eta_j \cdot \sin\delta_j & \cos\delta_j \end{pmatrix} \cdot \begin{pmatrix} 1 \\ \eta_s \end{pmatrix} \qquad \text{Eq.(II.25)}$$

where the elements B and C are related to the systems admittance by

$$Y = \frac{C}{B} \qquad \text{Eq.(II.26)}$$

Combining Eq.(II.14) and Eq.(II.26) yields the polarization-specific reflectance of the multilayer film when the properly defined characteristic admittances for the incident medium, substrate, and layers are used.

Equations Eq.(II.9) and Eq.(II.14) through Eq.(II.26) can be readily incorporated into program for calculating the modal attenuation of the HCWs using a calculation management suite such as Mathcad or Matlab. In this study, Mathcad v.13.1 was used to write programs to determine the transmission loss of the HE_{11} mode for HBFs and HGWs operating in the infrared to THz spectral range. The results of these calculations have been checked against the reflectance calculated using the optical thin film analysis software IMD v. 4.1 [23]. This software package calculates the reflectance of arbitrary multilayer structures using Rouard's method. IMD was also very useful in calculating reflectance bandgap diagrams in which the reflectance is obtained as a function of wavelength and angle of incidence. This is because the IMD software is capable of efficiently handling large data sets.

II.F Optimized Hollow Core Waveguide Structures

There is a vast array of reflector designs described in the literature that could be applied to HCWs [15,16]. Any reflector design devised with real materials in mind, i.e. the refractive index of each layer is complex, must consider two effects that reduce the reflectivity coefficients: transmission of energy though the system, *T*, and absorption of energy by the system, *A*. A simple definition of the reflectivity of the system is thus:

$$R = 1 - T - A \qquad \text{Eq.(II.27)}$$

Metallic reflectors have high R due to the high refractive index and extinction coefficients of the metals commonly used as reflectors such as, Ag, Au, Cu, and Al. In the case of a metallic reflector, $T = 0$ as long as the metal is thicker than its skin depth. A is non-zero because any radiation that is not reflected is absorbed by the metal. Greater R values can be achieved using multilayer dielectric reflectors. The layer thicknesses of a multilayer reflector are designed to achieve very low T for specific wavelengths. A is also low when dielectrics with low extinction coefficients are chosen. Hybrid metallic/dielectric mirrors have one or more dielectric layers deposited over a metallic substrate. High R can be obtained using a hybrid reflector design with fewer layers than an all-dielectric design. Hybrid reflectors have been successfully applied to HGWs and Hollow Polycarbonate Waveguides (HPWs) operating in the infrared spectral range [24,25]. This study is focused on the two reflector designs that have received the most widespread application in HCWs and have the greatest potential for future applications; the single dielectric thin film on a metal substrate hybrid reflector and the all-dielectric multilayer Bragg reflector.

II.F-1 All-dielectric hollow Bragg fibers

HBFs are based upon the design of the multilayer Bragg reflector which is shown in **Figure II-6**. The Bragg reflector design consists of alternating high refractive index, n_H, / low refractive index, n_L, layers. The Bragg reflector is also characterized by the number of layer pairs, N, of in the dielectric stack. Structures with n_L layers nearest the

incident medium and substrate, thus having a total of $2 \cdot N+1$ layers, have higher reflectance at near grazing incidence (a characteristic of the low loss modes) than those with an even number of layers or those with n_H layers at the incident medium and substrate interfaces. In the context of the nomenclature describing the arbitrary multilayer film discussed in Section II.C, the j = odd layers have the refractive index n_L and the j = even layers have the refractive index n_H.

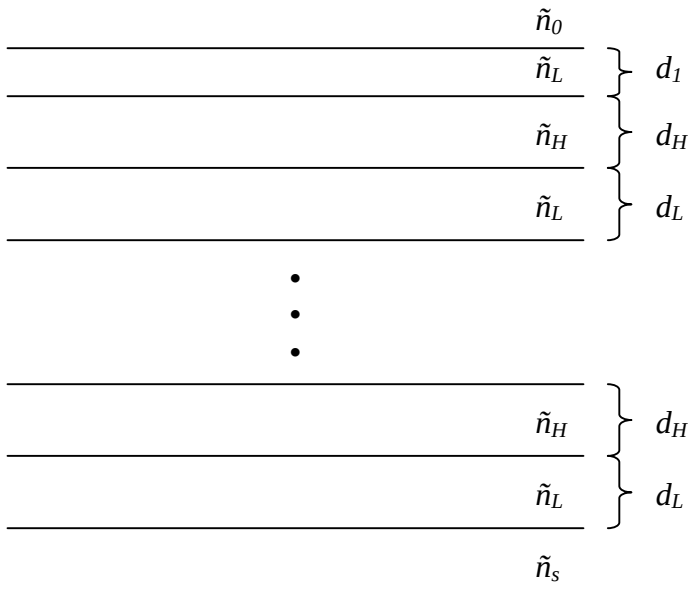

Figure II-6: A schematic diagram of the multilayer alternating n_L/n_H all dielectric Bragg reflector design.

Under the assumption that the layers are non-absorbing (k = 0) the optimum thickness of each layer, with the exception the layer nearest the incident medium (j = 0), is given by the quarter wave condition at glancing incidence [4]

$$d_H = \frac{\lambda_o}{4 \cdot \sqrt{n_H{}^2 - 1}}, \qquad \text{Eq.(II.28)}$$

where d_H is the thickness of the n_H layers (j = 2…J-1) and

$$d_L = \frac{\lambda_o}{4 \cdot \sqrt{n_L{}^2 - 1}} \qquad \text{Eq.(II.29)}$$

where d_L is the thickness of the $j \neq 1$ n_L layers (j = 3…J). The thickness of the $j = 1$ layer is given by

$$d_1 = \frac{\lambda_0}{2 \cdot \pi \cdot \sqrt{n_L{}^2 - 1}} \cdot \tan^{-1}\left[\frac{n_L}{\left(n_L{}^2 - 1\right)^{1/4}} \cdot \left(\frac{n_L}{n_H} \right)^N \cdot \left(\frac{\left(n_L{}^2 - 1\right)}{\left(n_H{}^2 - 1\right)} \right)^{-N/2} \cdot \left(\frac{n_S}{n_S{}^2 - 1} \right)^{-1/2} \right]$$

Eq.(II.30)

It is important to consider the magnitude of the reflectance and its spectral variation when designing coatings for a HCW for practical use. If the waveguide is to be used for laser power delivery it is critical to design coatings to achieve maximum reflectivity, providing the lowest loss, at the laser's operating wavelength. The small spectral width of laser sources dictates that the HCW needs only to have low loss over a narrow spectral region centered on the operating wavelength. The HBF suits this criterion well. A wall design that provides low loss over a broad range of wavelengths is favorable for waveguides that are intended for spectroscopic applications. Metal/dielectric HGWs and HPWs have the flexibility to provide low loss at a single design wavelength and relatively low-loss over spectral range that extends from the design wavelength to longer wavelengths.

II.F-2 Metal/dielectric hollow glass waveguides

The design of the single dielectric layer on metal reflector, as shown in **Figure II-7**, is very simple and is the basis for the design of metal/dielectric HGWs. The

thickness of the metal, d_{metal}, must be thicker than its skin depth to prevent radiation leakage through the metal. For example the skin depth of silver in IR is between 10 nm and 30 nm. A dielectric added over the metal greatly enhances its reflectivity. The HE_{11} mode propagates at near glancing incidence for practical waveguide geometries as indicated by **Figure II-3**. The optimum thickness, d_d, at glancing incidence of a non-absorbing ($k = 0$) dielectric film on a metal substrate is given by [4]

$$d_d = \frac{\lambda_o}{2 \cdot \pi \cdot \sqrt{n_d^{\,2} - 1}} \cdot \tan^{-1}\left[\frac{n_d}{\left(n_d^{\,2} - 1\right)^{1/4}}\right] \qquad \text{Eq.(II.31)}$$

where λ_0 is the design wavelength and n_d is the refractive index of the dielectric.

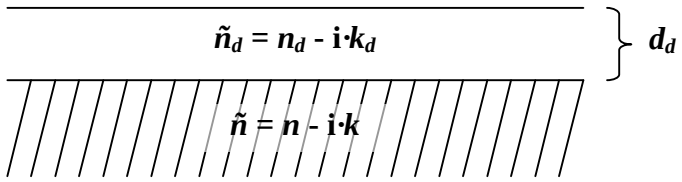

Figure II-7: A schematic diagram of the reflector design single dielectric layer on a metal substrate.

II.G Characteristics of the OmniGuide Hollow Bragg Fiber

The concept of the HBF was first proposed by Yeh and Yariv in 1978 [6]. One of the most interesting features of HBFs is that their transmission losses can be much lower than the materials from which they are made. The Bragg reflector design of the HBF walls results in a photonic bandgap centered on λ_0. The term photonic bandgap refers to a spectral region where the electromagnetic field intensities decrease exponentially with

depth into the multilayer Bragg reflector wall. As the ratio of n_H/n_L, termed the refractive index contrast, increases the fields decay more rapidly with depth into the HBFs inner wall. Any radiation with a wavelength within the bandgap and propagating along the axis of the fiber is confined to its hollow core. The fraction of the radiation confined to the core can reach near unity for an HBF with high refractive index contrast and many layer pairs. Since the core can be filled with dry air, inert gas or vacuum HBFs can be tuned over a broad spectral range to achieve low loss at a discreet wavelength by changing the layer thicknesses according to Eq.(II.28) through Eq.(II.30).

II.G-1 Structure and fabrication of OmniGuide fibers

The first practical demonstration of a HBF was accomplished in 2002 by researchers at MIT [26]. This HBF, termed the "OmniGuide" fiber, consists of a hollow core surrounded by alternating layers of arsenic triselenide (As_2Se_3) glass, $\tilde{n} = 2.74 - i1.3\times10^{-6}$, and polymer polyetherimide (PEI), $\tilde{n} = 1.69 - i0.046$ [27], supported by a thick outer PEI cladding as shown in **Figure II-8**. The fabrication of the fiber begins with the thermal evaporation of As_2Se_3 glass on either side of a PEI film. The coated film is then rolled into a spiral and covered with a thick PEI cladding to form a drawable preform that closely approximates the ideal HBF structure. An interesting feature of the OmniGuide fabrication process is its wavelength scalability. It is obvious by inspection of Eq.(II.28) and Eq.(II.29) that the ratio d_H/d_L does not change with λ_0. During the draw process the Omniguide HBF preform is heated and pulled reducing the inner and outer diameters and layer thicknesses in proportion. Since the ratio of the As_2Se_3 layer

thickness to the PEI layer thickness does not change during the draw process, the OmniGuide fiber's low loss wavelength can be adjusted simply by changing the diameter of the final hollow waveguide. The draw speed can be altered during the draw process allowing fibers that operate at many different wavelengths to be drawn from a single preform.

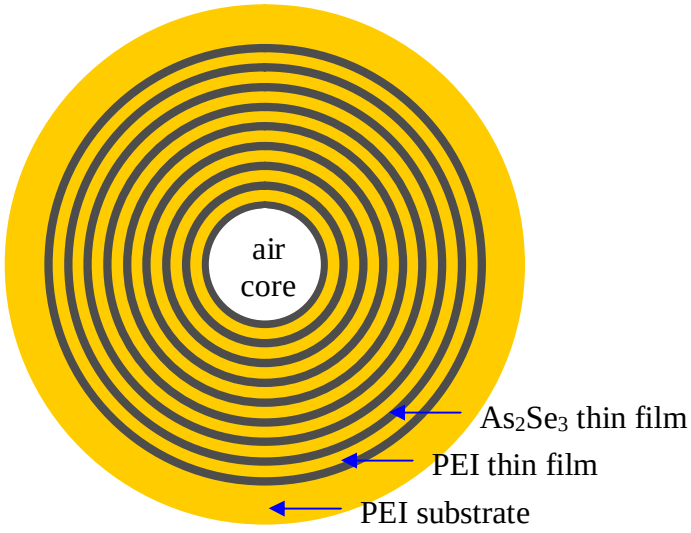

Figure II-8: A schematic of the OmniGuide HBF cross section.

II.G-2 Transmission of CO_2 laser radiation in OmniGuide fibers

The ray optics formulation is used to calculate the theoretical loss of the HE_{11} mode at 10.6 μm as a function of N for the Omniguide fiber. **Figure II-9** shows a comparison of the loss computed under the assumption of no materials absorption, i.e. $\tilde{n} = n - i \cdot 0$, and the loss computed when the complex refractive indices are considered. In the absence of materials absorption the transmission losses of the OmniGuide HBF can

be reduced arbitrarily by adding more layer pairs. When the complex refractive indices are used in the calculation it is apparent that materials absorption limits the decrease in loss upon the addition of layer pairs beyond N = 7. A minimum theoretical loss of 0.18 dB/m is achieved for N > 10.

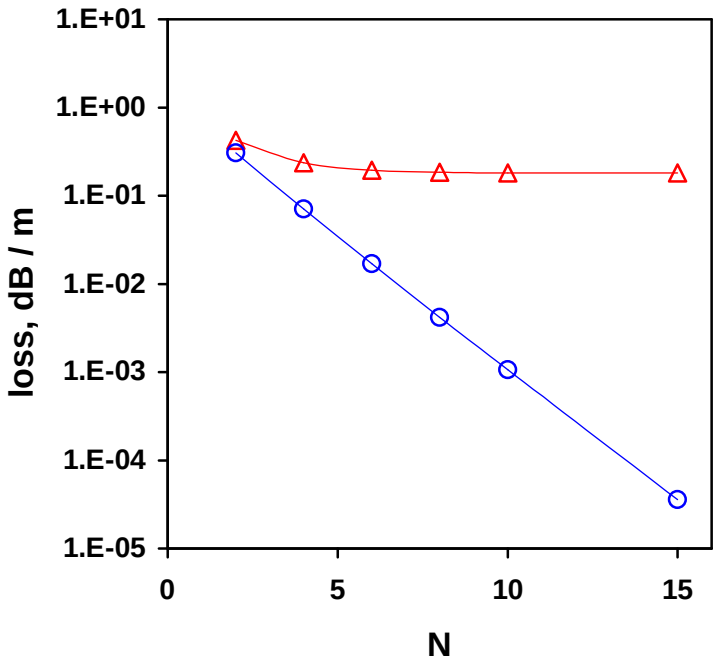

Figure II-9: The transmission loss of the HE_{11} mode for 10.6 μm CO_2 laser radiation propagating in an OmniGuide fiber is plotted as a function of the number of layer pairs, N, that form the waveguide's reflective inner wall. The red curve indicates the loss when the complex refractive indices of the materials are considered. Only the real indices are considered in the calculation of the blue curve. a = 350 μm and λ_o = 10.6 μm.

In practice, Omniguide HBFs with a = 350 μm tuned for transmission at 10.6 μm have losses as low as 0.5 dB/m [28]. The loss of the real fiber is expected to be higher than the calculated HE_{11} mode loss due to the presence of some higher order modes and structural imperfections from the fabrication process. The low loss of the OmniGuide

HBF at 10.6 μm is remarkable in light of the fact that the extinction coefficient of PEI at 10.6 μm corresponds to materials absorption of over 200,000 dB/m. To put this in perspective, CO_2 laser radiation focused on the outside of an OmniGuide HBF can ignite its PEI cladding. The low loss of the OmniGuide HBF, despite its high materials absorption, is possible because of its high refractive index contrast (n_H/n_L = 2.74/1.69 = 1.62).

II.G-3 Omnidirectional reflection

The OmniGuide HBF derives its name from the fact that over a range of wavelengths the bandgap of its Bragg reflector wall is omnidirectional, meaning that it extends over all angles of incidence and polarizations [12,13]. IMD optical thin film analysis software is used to study the variation of the OmniGuide wall reflectivity with wavelength and angle of incidence. **Figure II-10** shows R_{avg} of the OmniGuide's wall plotted as a function of wavelength and angle of incidence under the assumption that the extinction coefficients of the layers are equal to zero. **Figure II-11** shows a similar plot except that it is calculated using the true extinction coefficients of the materials. In the absence of materials absorption, the fundamental bandgap appears as a white band (indicating high reflectivity) stretching from 10 μm to 14 μm at normal incidence and from 9.5 μm to 11.5 μm at glancing incidence. The omnidirectional bandgap thus extends from 10 μm to 11.5 μm, a range to midrange ratio (RTMR) of 14 %. These calculations provide similar information to the projected band structure diagrams of OmniGuide HBFs presented by researchers at MIT [26]. The RTMRs calculated using these methods

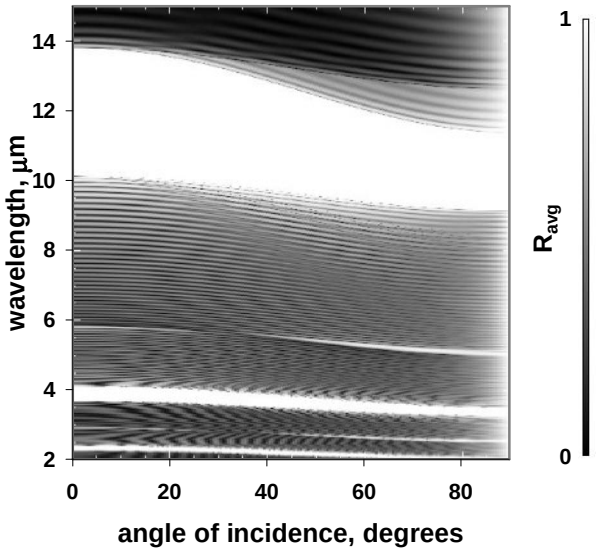

Figure II-10: The average reflectivity coefficient, R_{avg}, of an OmniGuide fiber is plotted on a color scale within a wavelength vs. angle of incidence coordinate system. The extinction coefficients of the materials are ignored. The high reflectivity photonic bandgap regions appear as white bands in the diagram. N = 35, k = 0, and λ_o = 10.6 μm.

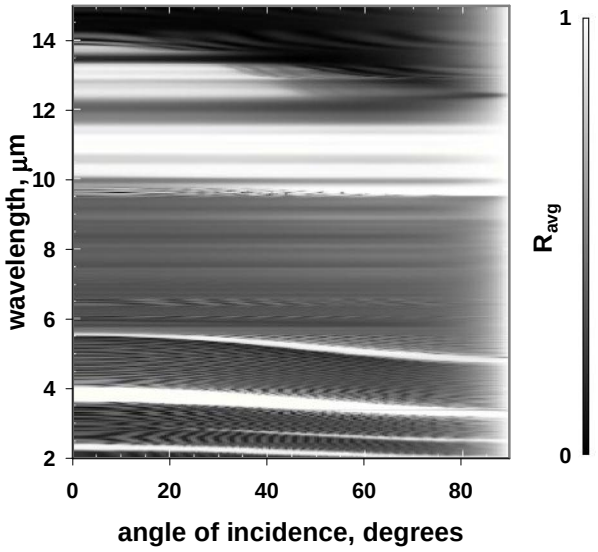

Figure II-11: The average reflectivity coefficient, R_{avg}, of an OmniGuide fiber is plotted on a black-to-white scale within a wavelength vs. angle of incidence coordinate system. The complex refractive indices of the materials are used in the calculations. Horizontal bands correspond to the absorption bands of PEI. N = 35 and λ_o = 10.6 μm.

are in good agreement [12]. When the materials' complex refractive indices are used in the calculation, the omnidirectional bandgap is largely eliminated due to materials absorption. Bands stretching horizontally across the diagram correspond to the strong infrared absorption bands of PEI. These calculations agree with the observed spectral response the OmniGuide HBF [26].

The significance of omnidirectionality is its potential to reduce bend losses in HCWs. The coupling of energy to higher order (hence higher loss) modes is responsible for increased loss on bending and is fundamental to all HCWs. There are two contributions to bend loss: Eq.(II.6) shows that a higher mode parameter fundamentally indicates higher loss; and the value of R_{avg} decreases as θ_z decreases for most HCW reflective wall designs. Bend losses are highest in metal coated HGWs because the reflectivity of the metal decreases dramatically as θ_z approaches the metals principle angle of incidence [29]. As shown in **Figure II-12**, a dielectric AgI layer added over an Ag coated HGW increases the wall's reflectivity at 10.6 μm for incidence angles near silver's principle angle of incidence and thus reduces the HGWs bend loss. Also shown in **Figure II-12** is the dependence of R_{avg} at 10.6 μm on θ_z for the walls of the Omniguide HBF. If materials absorption is ignored, R_{avg} of the OmniGuide HBF is near unity for all angles of incidence which would provide reduced bend losses with respect to Ag and Ag/AgI coated HGWs. Inclusion of the materials' extinction coefficients shows that the omnidirectionality of the OmniGuide's wall is diminished due to materials absorption. The bend loss of the OmniGuide at 10.6 μm has been found to increase linearly with the inverse of the bend radius at a rate of 0.015 dB·m for a 2.5 m long 700 μm diameter fiber subjected to 90 degree bends initiated 15 cm from the output [26]. The observation of

increased loss on bending proportional to the inverse of the bend radius is consistent with theory and experimental observations of other HCWs. Bend loss measurements are very sensitive to the details of the measurement set-up so it is unclear if the OmniGuide fiber has improved bend loss over Ag/AgI HGWs operating at 10.6 μm. The observed increased loss on bending does indicate that the full potential of omnidirectional reflection is not been realized in the OmniGuide fiber due to materials absorption.

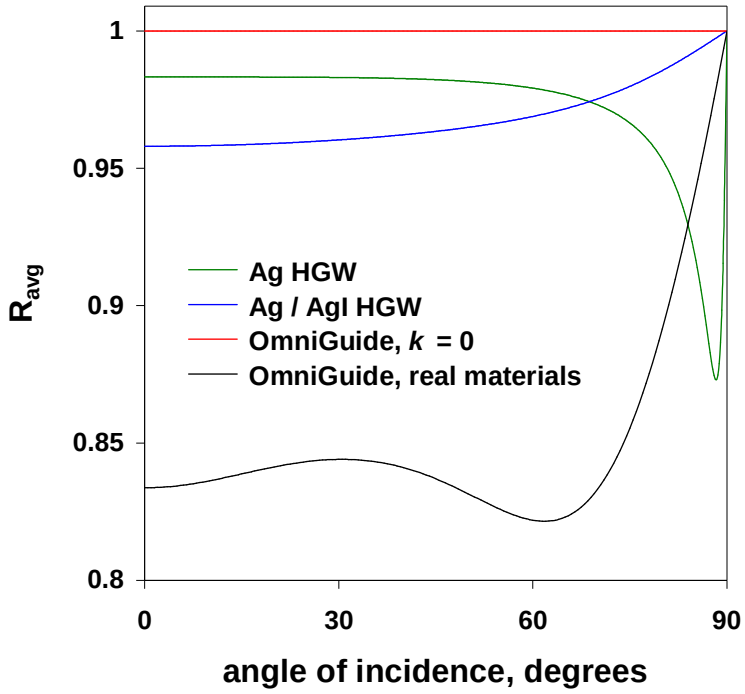

Figure II-12: The average reflectivity coefficient, R_{avg}, is plotted as a function of angle of incidence for the wall of a Ag coated HGW, a Ag/AgI coated HGW, and the OmniGuide fiber with and without materials absorption.

The fabrication techniques for the OmniGuide HBF have been refined to the point that fibers with near theoretical losses can be produced and they are gaining acceptance in the medical community for the delivery of CO_2 laser radiation for surgical applications

[30-31]. The OmniGuide HBF may not be able to meet the low loss requirements of high power CO_2 laser delivery applications like laser cutting and welding due to limitations imposed by its materials absorption and the low power threshold of the polymer layers. Application of the OmniGuide manufacturing techniques to materials with high index contrast and low absorption is a logical step towards the demonstration of even lower loss HBFs.

II.H Materials Selection for Infrared Transmitting Hollow Bragg Fibers

Improvement upon the OmniGuide fiber requires the incorporation of low loss materials, while maintaining high index contrast, into a similar fabrication process. One of the key elements in the fabrication of OmniGuide fibers is the fiber draw process. The fabrication of a preform with thick layers followed by a reduction in aspect ratio via the draw process naturally results in more accurate film thicknesses than a fiber that is fabricated to its final geometry directly. Additionally, the draw process has the effect of reducing the roughness of the layers in the preform as it is stretched into long lengths of fiber. The benefits of the draw process dictate that the search for new n_H and n_L materials for the fabrication of HBFs be limited to those which can be co-drawn, i.e. their working ranges must overlap [32].

There are several types of materials that can be drawn into optical fibers [33-35]. Oxide glasses, such as fused silica, are the basis for long haul telecommunications fibers. Heavy metal fluoride glasses like ZBLAN received much attention in the 1980s due to their low theoretical loss in the near infrared, but interest has waned due to difficulties in

fabricating fibers that are free of inclusions. Chalcogenide glasses, which include arsenic trisulfide, have been used in infrared transmitting fibers. Chalcohalide glasses, for instance TeX, are also of interest for infrared transmission and have applications in rare earth doped fiber amplifiers. Optical fibers made from thermoplastic optical polymers like PMMA and CYTOP are being implemented in low bandwidth telecommunications applications as a low cost alternative to fused silica fiber. The refractive index ranges and maximum transmission windows of the types of materials listed above are summarized in **Table II-2**.

material	refractive index	transmission window
oxide glasses	1.4 – 2.0	0.2 μm – 6 μm
fluoride glasses	1.4 – 1.6	0.5 μm – 8 μm
chalcogenide and chalcohalide glasses	2.0 – 3.4	0.7 μm – 30 μm
polymers	1.3 – 1.8	0.4 μm – 2 μm

Table II-2: The optical properties of some drawable materials.

The only materials that are drawable and have low transmission losses for CO_2 laser radiation are chalcogenide and chalcohalide glasses. The similarities of chalcogenide and chalcohalide glasses does allow them to be co-drawn, so it may be possible to fabricate a HBF with alternating layers of each glass type. The range of refractive indices from which to choose the n_L and n_H materials for a HBF operating at 10.6 μm may thus be taken as 2.0 to 3.4. The scientific community has devoted little

effort to the identification of high refractive index chalcogenide glasses. Infrared transmitting crystalline chalcogenides, such as PbSe, n = 4.74 at 10.6 μm [36], can have much higher refractive indices than those demonstrated in glass forming chalcogenides. In anticipation of the possible discovery of higher refractive index chalcogenide glasses, calculations of the optical behavior of HBFs with n_H up to 3.8 are presented in Section II.I.

II.I Chalcogen Based Hollow Bragg Fibers

The loss of the HE_{11} mode propagating in HBFs with $2.0 \leq n_L \leq 2.5$ and $2.8 \leq n_H \leq 3.8$ is examined in this section. This study is conducted for the purpose of assessing the potential for low loss transmission of CO_2 laser radiation in HBFs with a reflective wall constructed from chalcogen based glasses. The effect of the materials' optical constants, number of layers in the structure, and layer thickness errors on the HE_{11} loss is studied to provide a basis for materials selection and the evaluation of potential fabrication techniques. In anticipation of economics dictating that a chalcogenide HBF be fabricated with a minimum number of layers, a HBF structure is proposed that consists of an air core surround by alternating layers of chalcogen based glasses supported by a thick polymer coating. The structure of the proposed chalcogenide HBF is shown in **Figure II-13**. PEI is selected as the substrate material because its ability to be co-drawn with chalcogenide glasses has already been demonstrated. The complex optical constants of PEI are used for n_s and k_s in all the calculations presented in this section.

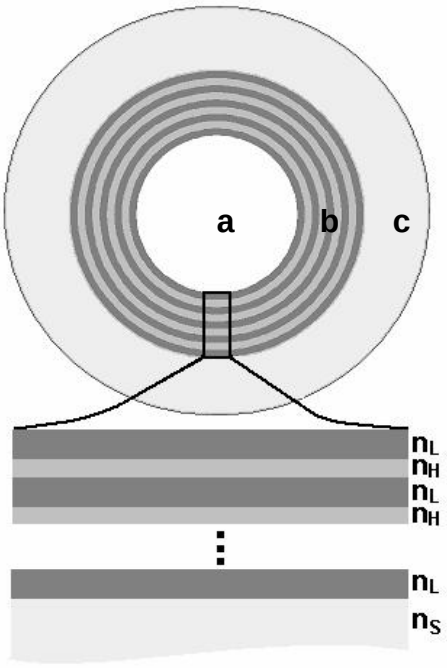

Figure II-13: A schematic diagram of the proposed fiber cross-section showing its air core (a), chalcogenide glass Bragg reflector film (b), and thick polymer coating (c). A schematic of the film's layered structure and polymer substrate is shown below the cross section.

II.I-1 Loss and refractive index contrast

The study is initiated using ray optics calculations to determine the theoretical loss of the HE_{11} mode at 10.6 μm for HBFs with $2.0 \leq n_L \leq 2.5$ and $2.8 \leq n_H \leq 3.8$, a = 500 μm, and N = 25 layer pairs. The reflectivity coefficients required for the ray optics calculations are determined using the impedance transfer matrix method as described in Section II.E. The loss, expressed in dB/m is plotted as contours in an n_H vs. n_L coordinate system in **Figure II-14**. n_H is taken in increments of 0.2 while n_L is taken in increments of 0.1. The theoretical transmission loss of the lowest contrast pair,

n_L = 2.5 / n_H = 2.8, is $2.5 \cdot 10^{-2}$ dB/m while the loss of the highest contrast pair, n_L = 2.0 / n_H = 3.8, is $3.7 \cdot 10^{-12}$ dB/m. The loss contours shown in **Figure II-14** are linear and have a slope that is similar to that of the refractive index contrast contours plotted in the same coordinate system as shown in **Figure II-15**. Thus the information contained in **Figure II-14** can be summarized by plotting loss as a function of refractive index contrast as shown in **Figure II-16**. The correlation between refractive index contrast and loss is obvious and it is apparent that the loss decreases exponentially with increasing refractive index contrast. This type of plot is useful because it allows the comparison all refractive index combinations while varying other important quantities, such as the number of layers and the materials extinction coefficient.

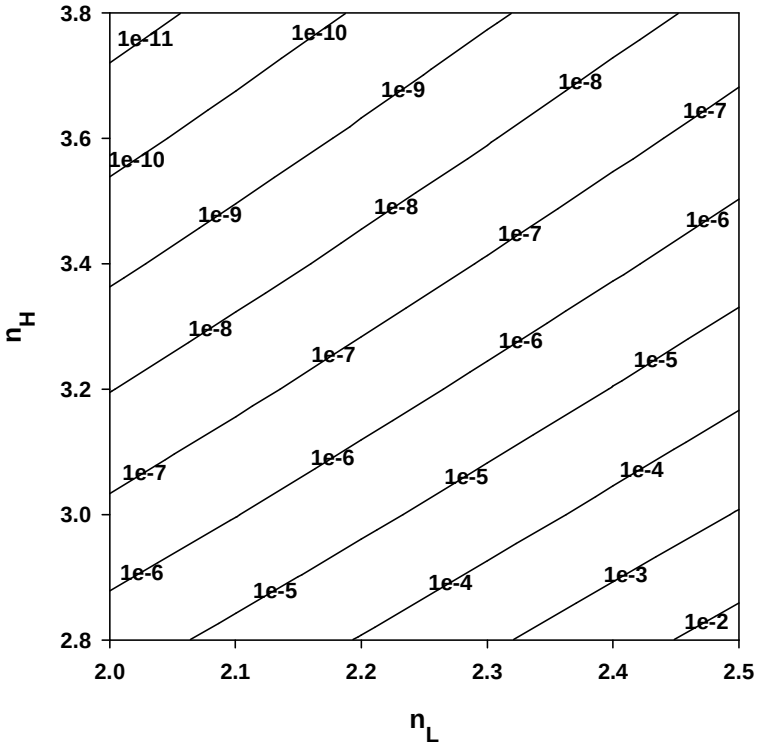

Figure II-14: HE_{11} transmission loss contours for CO_2 laser radiation are plotted in an n_H vs. n_L coordinate system for HBFs. Loss values are expressed in dB/m. a = 500 μm, k = 0, N = 25, and λ_o = 10.6 μm.

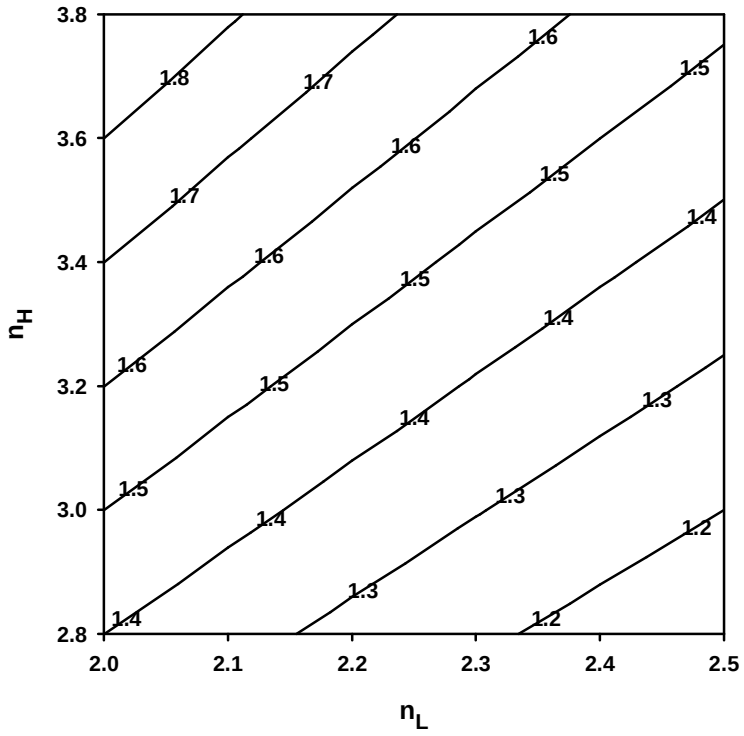

Figure II-15: Refractive index contrast n_H/n_L contours are plotted in an n_H vs. n_L coordinate system.

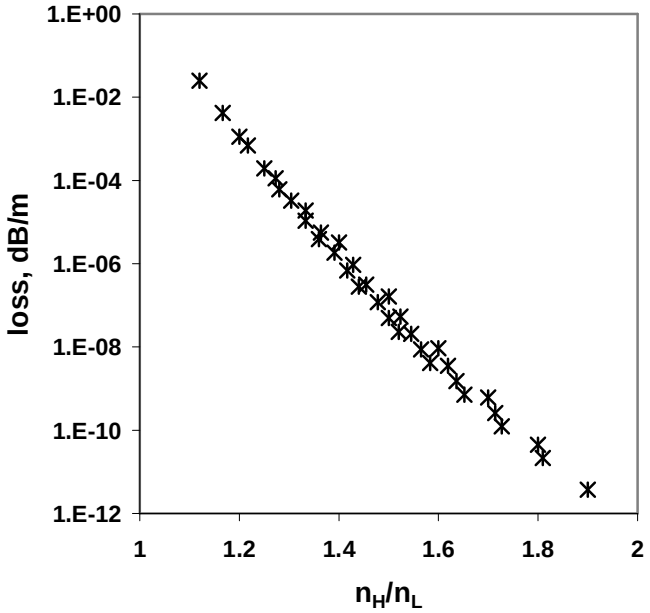

Figure II-16: Theoretical HE_{11} mode transmission loss for CO_2 laser radiation is plotted as a function of refractive index contrast n_H/n_L for HBFs with $2.0 \leq n_L \leq 2.5$ and $2.8 \leq n_H \leq 3.8$. $N = 25$, $a = 500$ μm, $k = 0$, and $\lambda_o = 10.6$ μm.

II.I-2 Effect of additional layer pairs

The HE_{11} loss is plotted as a function of refractive index contrast for N = 5, 10, 15, 20, and 25 layers pairs in **Figure II-17**. Again the extinction coefficient of the layers is assumed to be zero. The loss decreases exponentially with refractive index contrast for all values of N. The loss also decreases exponentially as N increases for constant refractive index contrast as was the case when the materials absorption of the Omniguide was ignored. Referring back to Eq.(II.5), the loss is linearly related to the transmittance, $T = 1\text{-}R$, of the multilayer stack. It is well know that T decreases exponentially as N and refractive index contrast increase [16]. Losses below that of the real ($k \neq 0$) OmniGuide are possible for any contrast value when N is greater than 15 layer pairs, and moderate contrasts of 1.2 and 1.4 are required to improve on the Omniguide for N = 5 layer pairs and N = 10 layer pairs, respectively.

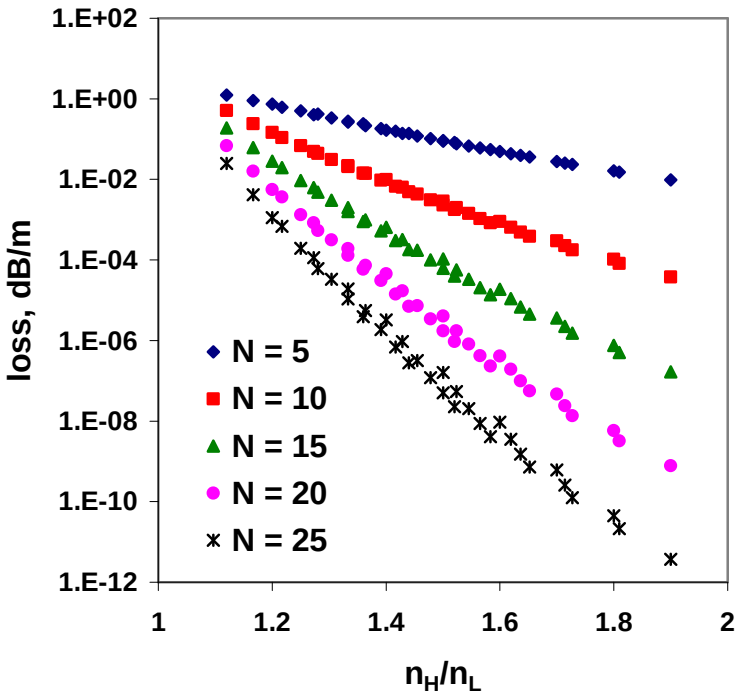

Figure II-17: Theoretical HE_{11} mode transmission loss for CO_2 laser radiation is plotted as a function of refractive index contrast n_H/n_L for HBFs with $2.0 \leq n_L \leq 2.5$ and $2.8 \leq n_H \leq 3.8$ for various numbers of layer pairs, N. a = 500 μm, k = 0, and λ_o = 10.6 μm.

II.I-3 Effect of materials absorption

The analysis of the OmniGuide fiber presented in Section II.G-2 indicates that materials absorption is a critical factor in the design of HBFs. **Figure II-18** shows the theoretical HE_{11} loss at 10.6 μm for chalcogen based HBFs plotted as a function of index contrast for various degrees of materials absorption. The value of N = 25 layer pairs was held constant in the loss calculation for extinction coefficient values of $k = k_L = k_H = 10^{-3}$, 10^{-5}, 10^{-7}, and 0. Each layer is assumed to have the same extinction coefficient for simplicity. The effect of materials absorption is most obvious for high index contrasts. The loss calculated for the highest contrast pair, n_L = 2.0 and n_H = 3.8, increases by many

orders of magnitude upon increasing k from 0 to 10^{-7} and increases even more going to higher values of k. The effect is much less dramatic for lower refractive index contrast. The magnitude of k defines the range of index contrasts where the loss of HBFs with non zero k becomes higher than those with zero k. In effect, materials absorption limits the benefit of increasing refractive index contrast of the layer materials in HBFs.

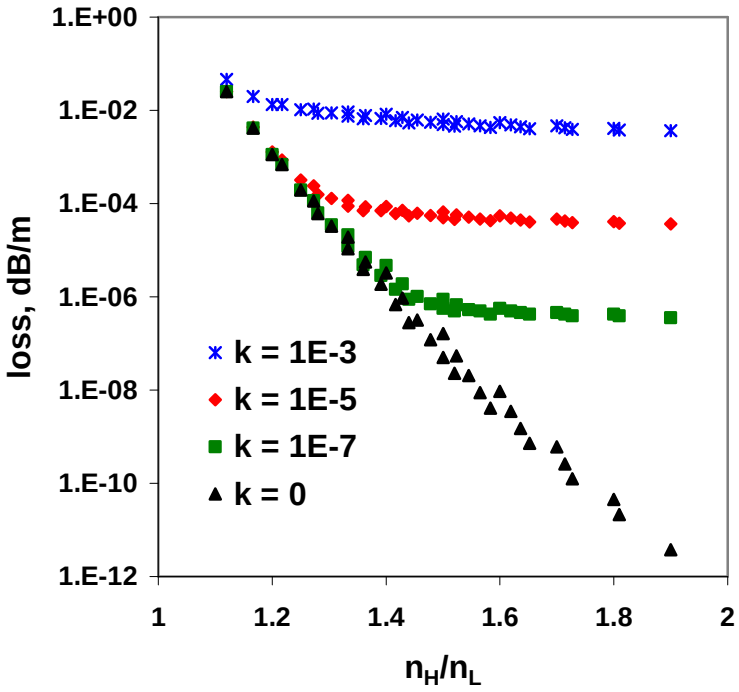

Figure II-18: Theoretical HE_{11} mode transmission loss for CO_2 laser radiation is plotted as a function of refractive index contrast n_H/n_L for HBFs with $2.0 \leq n_L \leq 2.5$ and $2.8 \leq n_H \leq 3.8$ for various extinction coefficients, k, of the layer pairs. a = 500 μm, N = 25, and λ_o = 10.6 μm.

Referring back to Eq.(II.27) it is apparent that the inclusion of materials absorption, resulting in a higher value of A, decreases wall reflectivity and contributes to higher calculated losses. A dominates the reflectivity term in Eq.(II.9) when k is high. T dominates when k is low. The transition between these two regimes is apparent in

Figure II-19 where the HE_{11} loss at 10.6 μm of an n_L = 2.4 / n_H = 3.2 HBF is plotted as a function of N for various values of k. The loss decreases exponentially as N increases for k = 0 and k = 10^{-5}. Attenuation of radiation propagating in these HBFs is limited by leakage through the walls. Adding more layers decreases the leakage exponentially. The loss decreases exponentially only up to 10 layer pairs for k = 10^{-3}. Beyond 10 layer pairs the decrease in loss become less significant as A becomes large relative to T. The fields are fully extinguished (T = 0) by absorption at depths beyond 20 layer pairs for k = 10^{-1}. Since A is independent of N, the loss is constant at 7.5×10^{-3} beyond 20 layer pairs. As was the case with the OmniGuide fiber, these calculations indicate that materials absorption limits the extent to which loss can be reduced by adding layer pairs to the structure of HBFs.

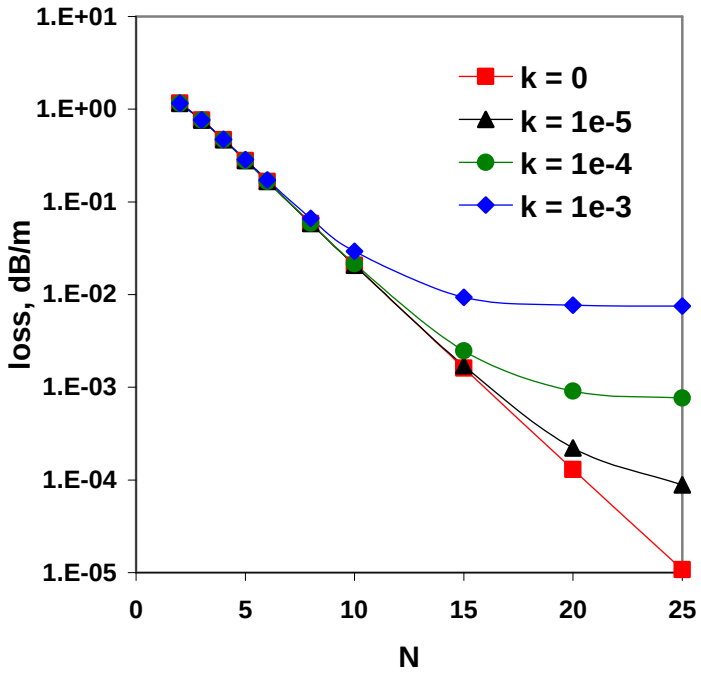

Figure II-19: The theoretical HE_{11} mode transmission loss for CO_2 laser radiation is plotted as a function of the number of layer pairs, N, for a n_L = 2.4 / n_H = 3.2 HBF for various extinction coefficients, k, of the layer pairs. a = 500 μm and λ_o = 10.6 μm.

II.I-4 Layer thickness uniformity

The calculations presented thus far have shown that a chalcogen based HBF with low materials absorption could transmit CO_2 laser radiation with lower losses than any fiber presently available. To achieve such low losses in practice would require the fabrication of a fiber that is free of structural defects and errors in layer thickness. Any real process will result in some degree of imperfection. To account for random variation in layer thickness along the length of an HBF the reflectivity of the wall is averaged over many randomized structures. The calculation is initiated by defining a layer structure with thicknesses assigned randomly based on a normal distribution of mean, μ, equal to the optimum layer thickness and standard deviation, σ. The ratio σ/μ is held constant for each layer and is used as a variable to quantify layer thickness error. A high value of σ/μ corresponds to a large variation in layer thickness along the length of the HBF. The reflectivities of a minimum of 5000 structures are averaged to obtain the true mean reflectivity for a given value of σ/μ. Additional randomized structures are incorporated until the mean reflectivity has not changed by more than 0.1% over the previous 1000 iterations. 5000 iterations were typically enough to satisfy this criterion for $\sigma/\mu < 0.05$, but in the case of $\sigma/\mu = 0.1$ as many as 15,000 iterations were required.

Figure II-20 shows the loss of the HE_{11} mode at 10.6 μm plotted as a function of refractive index contrast for HBFs with various magnitudes of layer thickness error expressed as σ/μ. The values $N = 10$, $k = 0$, and $a = 500$ μm were held constant for each calculation. Up to $\sigma/\mu = 5$ % there is very little change in the loss. Above 5 % the magnitude of the loss increase is uniform for all values of refractive index contrast. With

σ/μ = 10 % the increase in loss over the perfect structure is only about one half of an order of magnitude. Based upon these results one may conclude that variations in layer thickness inherent in any practical fabrication technique should not be prohibitive to the production of low loss chalcogen based HBFs for CO_2 laser radiation. For practical applications, the increased loss due to layer error would be most significant at low refractive index contrast because it corresponds to a greater decrease in the percentage of power transmitted by the waveguide.

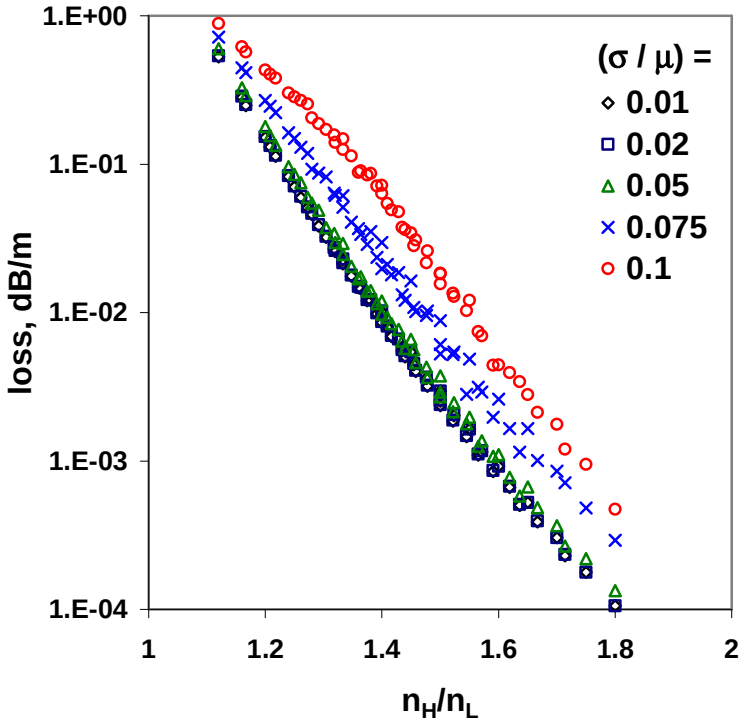

Figure II-20: The theoretical HE_{11} mode transmission loss for CO_2 laser radiation propagating in HBFs with $2.0 \leq n_L \leq 2.5$ and $2.8 \leq n_H \leq 3.8$ is plotted as a function of refractive index contrast n_H/n_L for various magnitudes of error, σ/μ, in their layer thicknesses as measured by the standard deviation, σ, of each layer's thickness divided by it's optimum thickness, μ. a = 500 μm, N = 10, and λ_o = 10.6 μm.

II.J Design of Metal/Dielectric Hollow Glass Waveguides for THz Radiation

Metal/dielectric HGWs consist of a glass capillary tube with an inner a metallic coating and thin dielectric film. The structure of a metal/dielectric HGW is shown schematically in **Figure II-21**. Metals that are commonly employed in HGWs include silver, copper, gold, and aluminum. The dielectric layer is formed either by a subtractive process [37] in which the metal is reacted with other chemicals to form a dielectric, as is the case with Ag/AgI and Cu/CuI HGWs, or the dielectric is added directly over the metal surface as in Ag/CdS [38] and Ag/COP HGWs [39]. Metal/Dielectric HGWs are most commonly used for the delivery of infrared laser radiation. **Figure II-22** shows a comparison of the experimentally-determined loss of real Ag/AgI coated HGWs [24] to the loss calculated using the MK formulation and the loss calculated as part of this study using ray optics. The optical constants measured by George [25] for Ag ($\tilde{n}$ = 4.97 – i·33.9) and AgI ($\tilde{n}$ = 1.95 – i·0) at 10.6 μm are used in the ray optics calculation. The agreement between both theoretical calculations and the experimental data confirms that ray optics calculations are applicable to metal/dielectric coated HGWs.

Metal/dielectric HGW technology has not been applied to the transmission of THz radiation, but referring back to Eq.(II.31) it is apparent that the layer thickness of the dielectric need only be scaled proportionally to achieve low loss at the desired wavelength so long as the metal is thicker than its skin depth for the radiation that is to be transmitted in the waveguide. Since wavelengths in the THz spectrum are one to two orders of magnitude longer than those in the infrared, a corresponding increase in film thicknesses is necessary. Stresses induced during deposition prevent films of such large

thickness from being deposited by the subtractive iodization process or the additive process used to create metal sulfide films. The dynamic liquid phase deposition process used to create polymer films is therefore the best candidate for scaling to the thicknesses required for THz radiation.

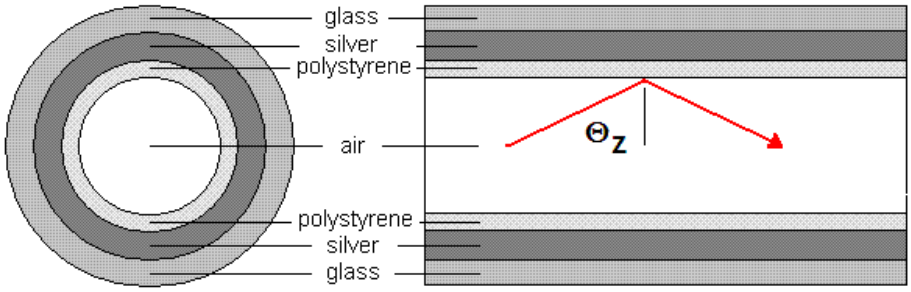

Figure II-21: A schematic diagram of the axial (left) and longitudinal (right) cross sections of a metal (Ag) / dielectric (PS) coated HGW.

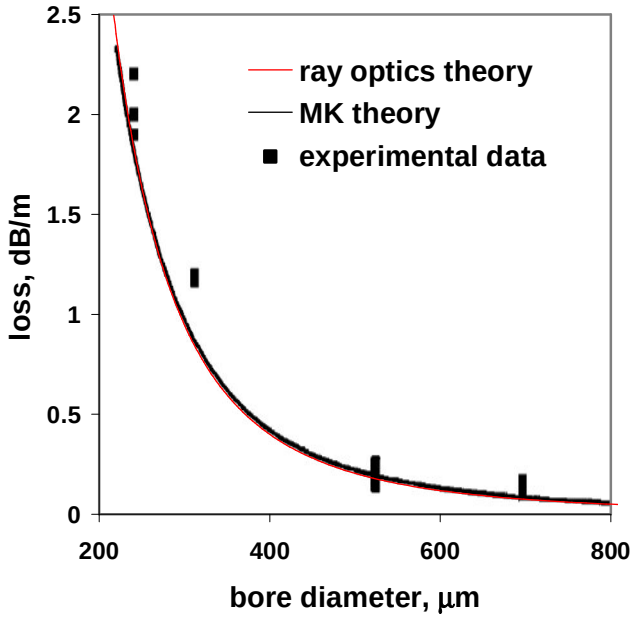

Figure II-22: The transmission loss for CO_2 laser radiation propagating in Ag/AgI coated HGWs is plotted as a function of their bore diameter, $2 \cdot a$. The red curve indicates the HE_{11} mode loss calculated using the ray optics method. The Miyagi-Kawakami impedance / admittance formulation is used to calculate the black curve. Black squares indicate experimental data.

II.J-1 Metal selection for THz hollow glass waveguides

Ag, Al, Au, and Cu have all been used in metal coated HGWs. At optical frequencies the metals have optical constants that are defined in the same manner as dielectrics, i.e. $\tilde{n} = n - i \cdot k$. The optical constants of metals in the infrared to THz spectral range are well described by the Drude model [40]. The Drude parameters are the plasma frequency ω_p and the damping frequency ω_τ and are related to the metal's optical constants by the equations:

$$\omega_\tau = \frac{2 \cdot \omega \cdot n \cdot k}{1 - n^2 + k^2} \qquad \text{Eq.(II.32)}$$

and

$$\omega_p{}^2 = \left(1 - n^2 + k^2\right) \cdot \left(\omega^2 + \omega_\tau{}^2\right) \qquad \text{Eq.(II.33)}$$

The values of the Drude parameters as well as calculated *n* and *k* at 119 μm for Ag, Al, Au, and Cu are given in **Table II-3**. The difference in the metals' Drude parameters corresponds to very different dependence of the optical constants on wavelength in the THz spectrum as shown in **Figure II-23**, in which *n* is plotted as a function of wavelength, and **Figure II-24**, where *k* is plotted as a function of wavelength. The calculated reflectivity coefficient at normal incidence at 512 μm for Ag and Cu is compared to experimental data to confirm the veracity of the calculated optical constants [41]. The results of this analysis are summarized in **Table II-4**. The similarity of the calculated and experimentally determined reflectivity coefficients indicates that it is appropriate to use the calculated optical constants in theoretical calculations of the loss of HGWs designed to transmit THz radiation.

metal	ω_p, cm^{-1}	ω_τ, cm^{-1}	n @ 119 μm	k @ 119 μm
Ag	$7.25 \cdot 10^4$	$1.45 \cdot 10^2$	305	529
Al	$1.19 \cdot 10^5$	$6.47 \cdot 10^2$	335	382
Au	$7.25 \cdot 10^4$	$2.16 \cdot 10^2$	293	429
Cu	$6.38 \cdot 10^4$	$2.78 \cdot 10^2$	243	328

Table II-3: The Drude parameters and optical properties of some metals.

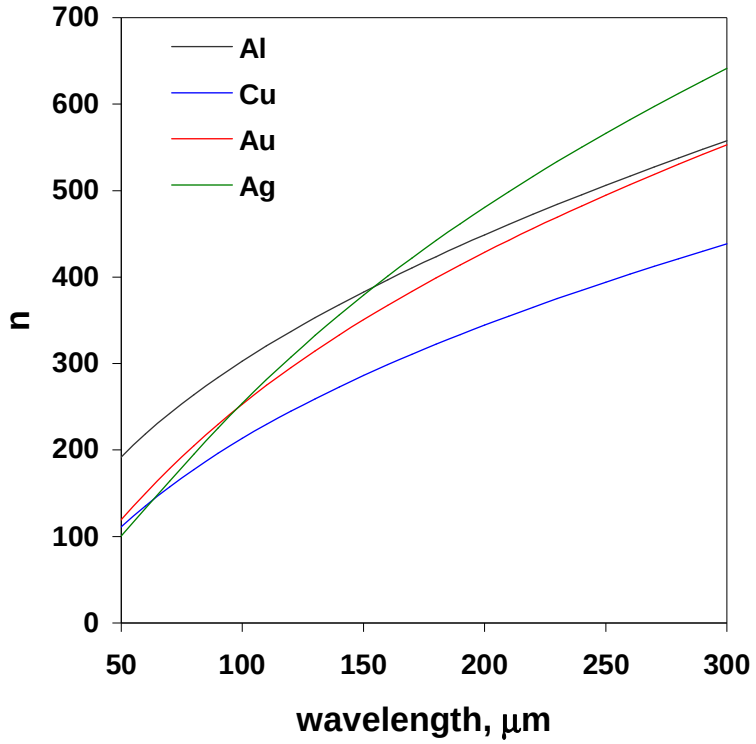

Figure II-23: The refractive indices, n, of some metals commonly used as reflective coatings for HGWs are plotted as a function of wavelength. The values are calculated from each metal's Drude coefficients.

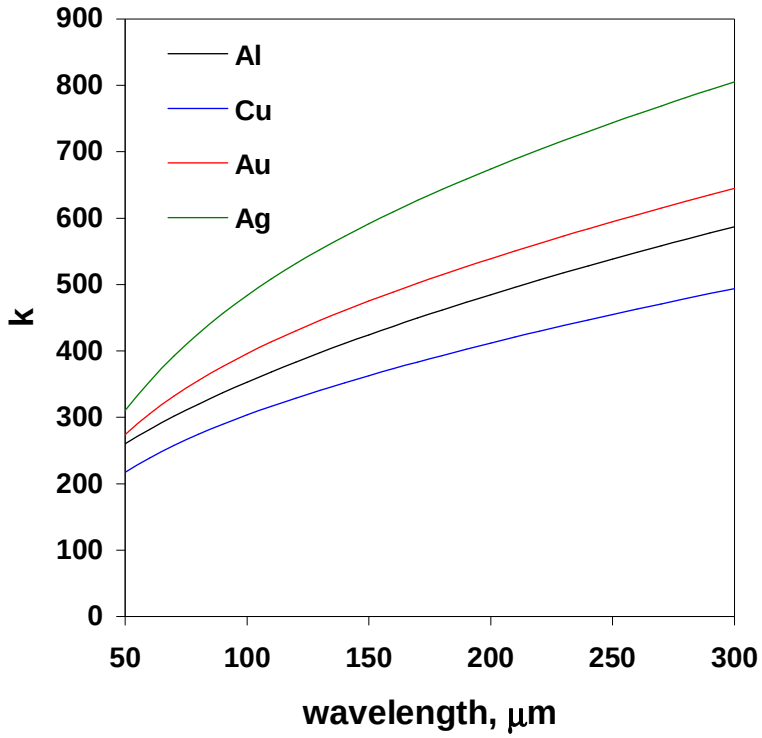

Figure II-24: The extinction coefficients, *k*, of some metals commonly used as reflective coatings for HGWs are plotted as a function of wavelength. The values are calculated from each metal's Drude coefficients.

metal	R (experimental)	R (calculated)
Ag	0.996	0.9981
Cu	0.997	0.9969

Table II-4: Experimental and calculated reflectivities of copper and silver at normal incidence for 512 μm radiation.

The loss of the HE_{11} mode propagating in metal coated HGWs at 119 μm is plotted as a function of bore diameter, $2 \cdot a$, in **Figure II-25**. The metal thickness is assumed to be of infinite thickness. The loss increases rapidly with decreasing bore size, consistent with $1/a^3$ dependence predicted by the MS and MK theories. Silver has the lowest loss for all bore sizes. In practice it is favorable to utilize the thinnest metal coating possible not only to reduce raw materials cost and fabrication time, but more importantly because the roughness of the metal surface increases with thickness, causing a corresponding increase in loss. The loss of the HE_{11} mode propagating in a = 900 μm metal coated HGWs at 119 μm is plotted as a function of the metal thickness, d_{metal}, in **Figure II-26**. The substrate material is taken as silica glass with a complex refractive index $\tilde{n} = 1.58 - i \cdot 0.0036$ [36]. The metal thickness require to reach the minimum loss are summarized in **Table II-5**. These values are approximately equal to the skin depth. All of the investigated metals reach a constant loss beyond 200 μm. The predicted HE_{11} mode loss ranges from 3.79 dB/m, for Ag, to 6.43 dB/m, for Cu. The calculated losses for the HE_{11} mode are significantly higher than those predicted for the TE_{01} mode by Roser et al. [42]. For a = 1000 μm they calculate a loss of 0.08 dB/m for a Cu waveguide. Such low losses have not been demonstrated in practice due to the inefficient coupling of THz laser radiation to the TE_{01} mode. Of the metals investigated, Ag is the easiest to deposit and provides the lowest calculated loss for the HE_{11} mode, which can be coupled readily to a THz laser source. Ag coatings are therefore the best choice for HGWs designed for THz radiation.

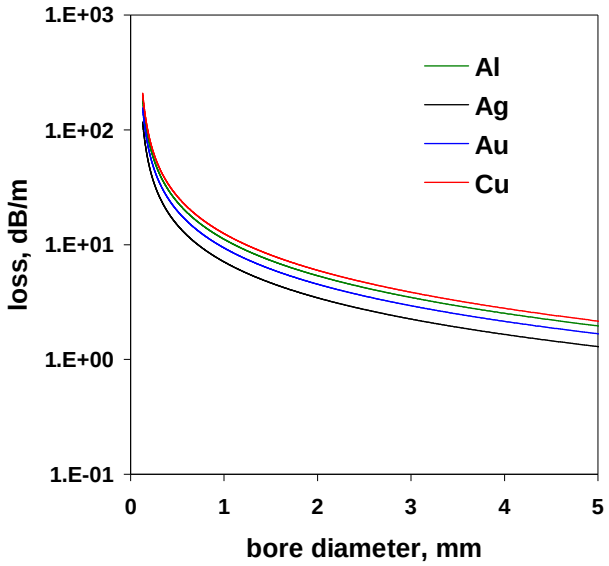

Figure II-25: The theoretical HE_{11} mode transmission loss for CH_3OH laser radiation at 119 μm is plotted as a function of bore diameter for metal-coated HGWs. Each curve represents a different metal commonly used in reflective coatings for HGWs.

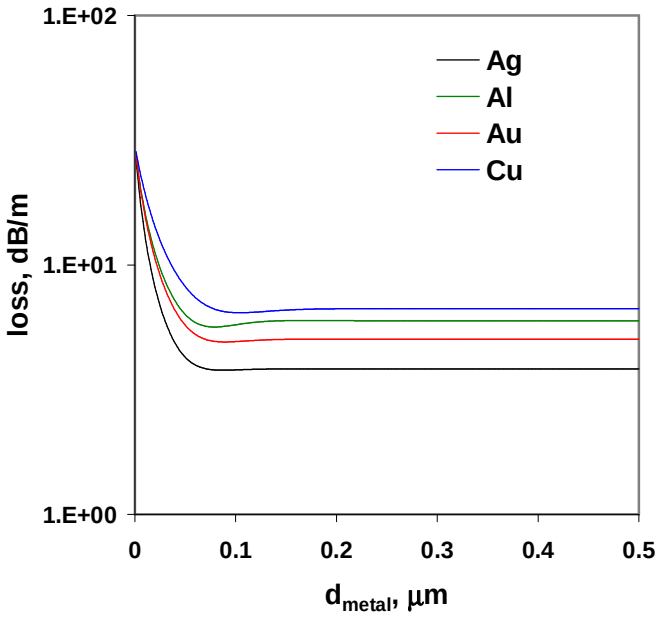

Figure II-26: The theoretical HE_{11} mode transmission loss for CH_3OH laser radiation at 119 μm is plotted as a function of the metal layer thickness, d_{metal}, for metal coated HGWs. Each curve represents a different metal commonly used in reflective coatings for HGWs. a = 900 μm.

metal	d_{metal}, nm	loss, dB/m
Ag	87	3.79
Al	79	5.64
Au	89	4.91
Cu	104	6.43

Table II-5: Optimum metal thicknesses and HE_{11} mode loss for metal coated silica HGWs at 119 μm.

II.J-2 Evaluation of dielectrics for THz hollow glass waveguides

Ag/dielectric HGWs with arbitrarily chosen values of n_d and k_d are compared in this section to establish a basis for evaluating materials for use as the dielectric layer to lower the loss. The loss of a = 900 μm Ag/dielectric HGWs at 119 mm is plotted as a function of n_d in **Figure II-27** for k_d equal to 0, 10^{-4}, 10^{-3}, 10^{-2}, and 10^{-1}. The addition of any dielectric film with $1.3 \leq n_d \leq 5$ and $k \leq 10^{-2}$ results in a loss reduction over the Ag-only HGW studied in Section II.I-1. The maximum loss reduction is achieved for n_d = 1.41 and k_d = 0 which is consistent with MK theory [4]. Losses in Ag/dielectric HGWs with k_d = 0 are attributed to absorption in the metal only, so it may be concluded that n_d = 1.41 minimizes the field intensity going into the metal surface. The minimum loss increases as k_d increases because of absorption in the dielectric film. The value of n_d that provides the minimum loss also increases. As n_d increases beyond 1.41 there is a trade-off between increased field intensity going into the surface of the metal, hence increased absorption by the metal, and decreased field intensity within the dielectric,

hence decreased absorption in the dielectric film. The value of n_d that provides optimum balance of absorption in the film and absorption in the metal increases as k_d increases. The optimum value of n_d is plotted as a function of k_d in **Figure II-28**. The optimum n_d is constant at 1.41 up to $k_d = 10^{-5}$ then grows exponentially for $k_d > 10^{-3}$ as the loss transitions from being dominated by absorption in the metal to being dominated by the absorption in the dielectric.

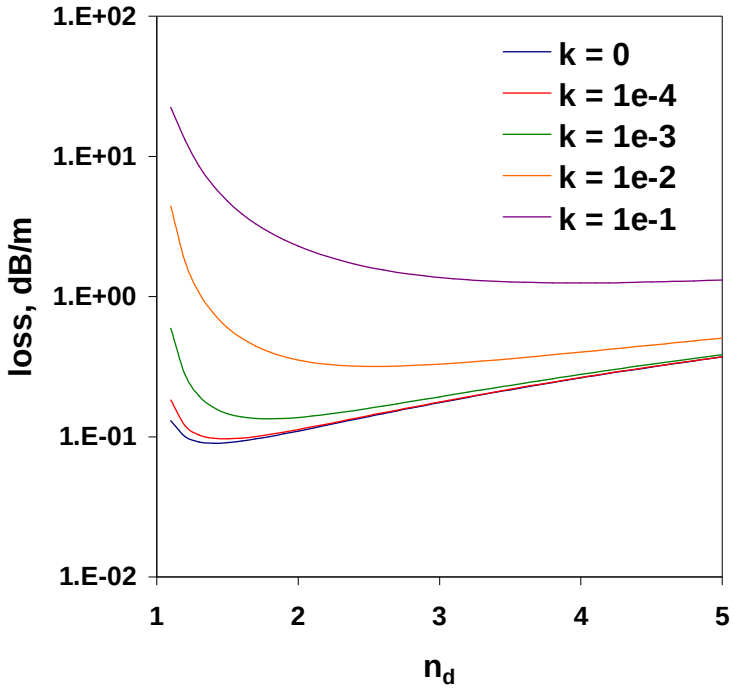

Figure II-27: The theoretical HE_{11} mode transmission loss for CH_3OH laser radiation at 119 μm is plotted as a function of the refractive index of the dielectric film, n_d, for Ag/dielectric coated HGWs. Each curve is calculated assuming a different value for the extinction coefficient of the dielectric. a = 900 μm and λ_o = 119 μm.

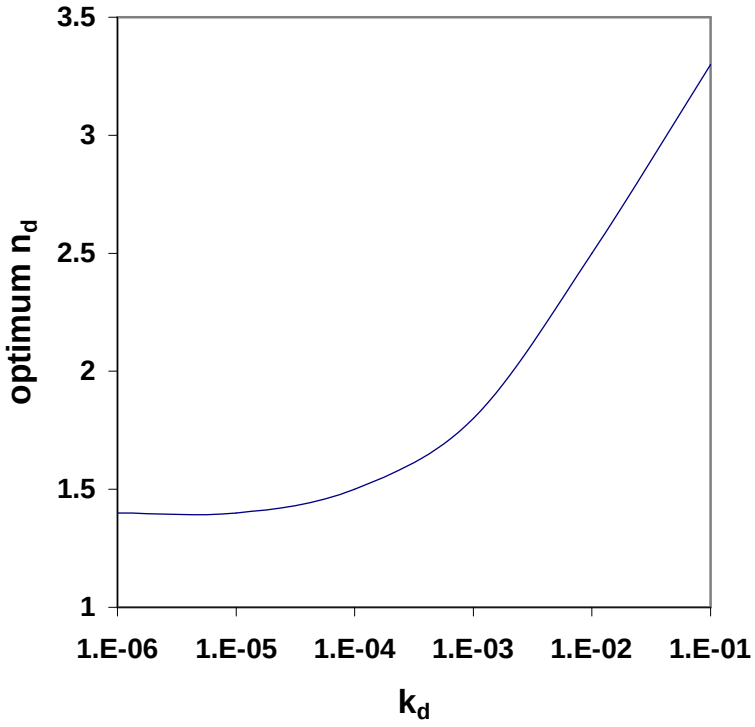

Figure II-28: The optimum dielectric refractive index, n_d, for a Ag/dielectric coated HGW is plotted as a function of the dielectric's extinction coefficient k_d.

The lowest losses for Ag/dielectric coated hollow waveguides correspond to low k_d and $1.3 \leq n_d \leq 2.0$. The optical properties of polymers closely match this criterion for THz radiation. The refractive index and extinction coefficients of polystyrene (PS) in the high frequency range of the THz spectrum are plotted as a function of wavelength in **Figure II-29** and **Figure II-30** [43]. The complex refractive index of PS at 119 μm falls well within the range of the combinations of n_d and k_d that result in Ag/dielectric HGWs with significantly lower loss than Ag-only HGWs.

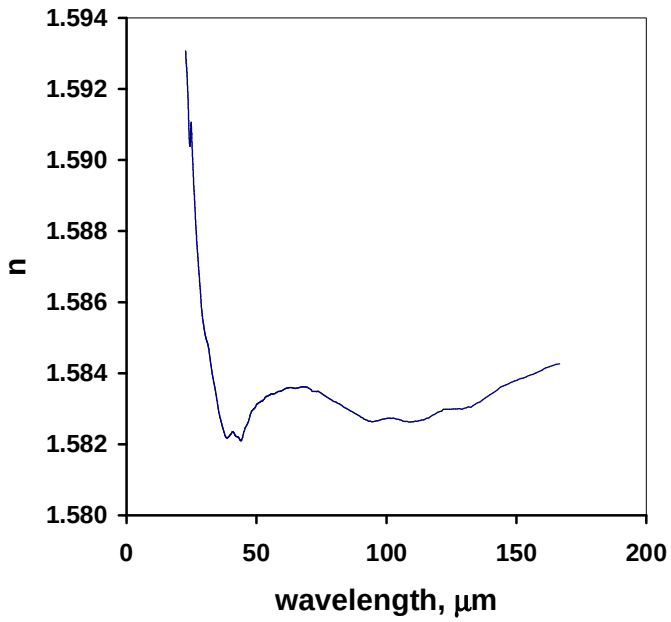

Figure II-29: The refractive index, *n*, of PS is plotted as a function of wavelength [43].

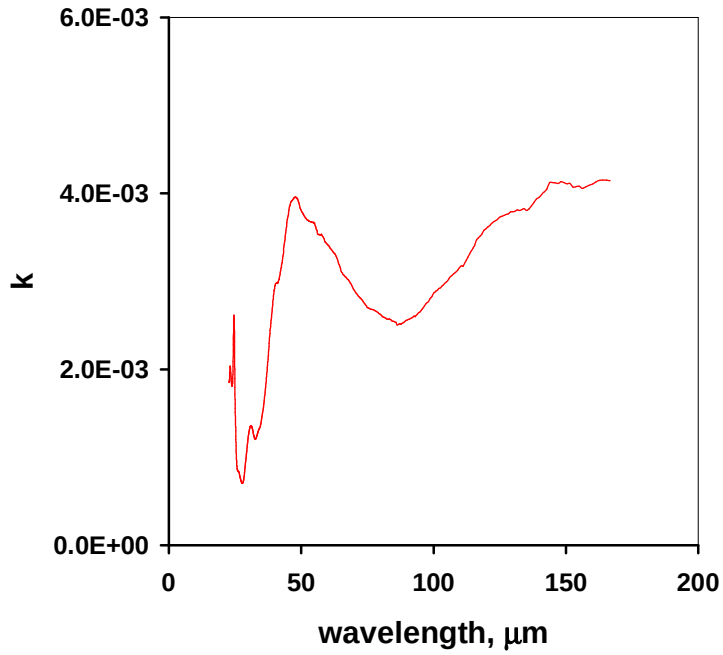

Figure II-30: The extinction coefficient, *k*, of PS is plotted as a function of wavelength [43].

II.J-3 Silver/polystyrene hollow glass waveguides for THz radiation

Figure II-31 shows the calculated loss of the HE_{11} mode at 119 μm propagating in an a = 900 μm Ag/PS HGW plotted as a function of PS film thickness, d_d. The loss decreases rapidly from d_d = 0 μm (metal only) until it reaches a minimum of 0.25 dB/m, over an order of magnitude improvement over the Ag-only HGW, at d_d = 12.7 μm. The loss increases to a maximum at about 25 μm. The spectral dependence of the loss for d_d = 0 μm, 5 μm, 12.7 μm and 25 μm is plotted in **Figure II-32**. There is a broad spectral range for which the loss of Ag/PS coated HGWs is lower than that of the Ag-only HGW. The minimum loss wavelength increases in proportion to the film thickness as is expected by inspection of Eq.(II.31). d_d = 25 μm corresponds to the PS thickness where the first order interference band of the dielectric film occurs at 119 μm, which explains the maximum loss observed for this thickness in **Figure II-30**.

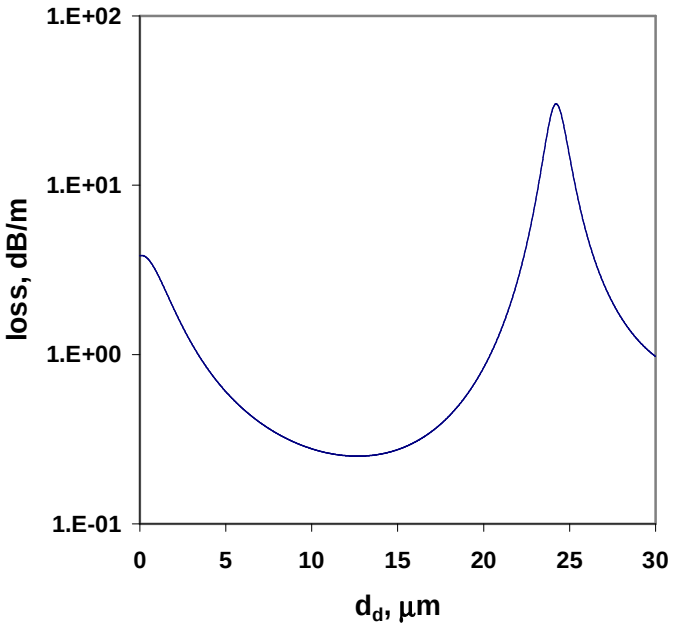

Figure II-31: The theoretical HE_{11} mode transmission loss for CH_3OH laser radiation at 119 μm is plotted as a function of different PS film thickness, d_d, for Ag/PS coated HGWs. a = 900 μm and λ_o = 119 μm.

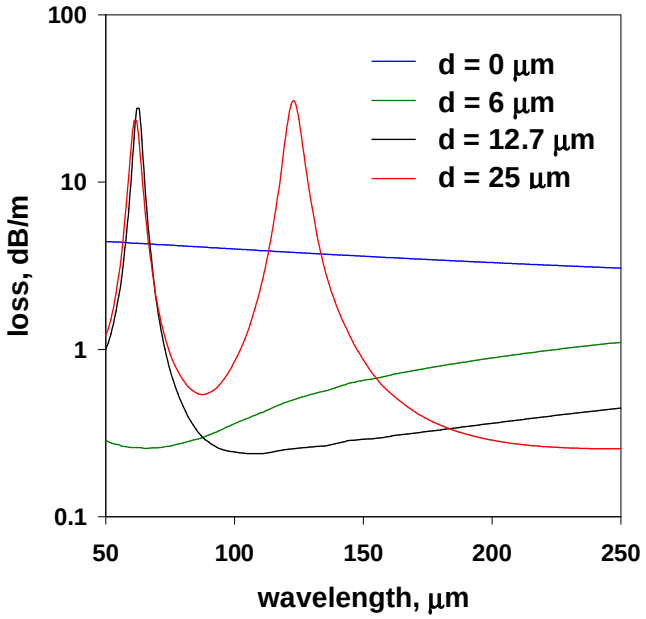

Figure II-32: The theoretical HE_{11} mode transmission loss for CH_3OH laser radiation at 119 μm is plotted as a function of wavelength for Ag/PS coated HGWs. Each curve represents a different PS film thickness d_d. a = 900 μm.

The fabrication and characterization of Ag/PS HGWs by dynamic liquid phase coating methods is described in **Chapter IV**. In light of the difficulties experienced by other researchers [44] in obtaining uniform films designed for 10.6 μm radiation it is important to consider the impact of non-uniformity of the PS layer thickness for Ag/PS HGWs designed to transmit THz radiation. As was the case in Section II.I-4, the magnitude of the layer error is defined by the ratio σ/μ. The loss of the HE_{11} mode at 119 μm propagating in Ag/PS HGWs with a = 900 μm is plotted as a function of σ/μ in **Figure II-33**. The increase in loss with layer non-uniformity is modest up to σ/μ = 20%. The resistance of the Ag/PS HGW structure to increased loss due to layer non-uniformity can be attributed to fact that for any given thickness the spectral width of low loss wavelengths is up to 50% of the design wavelength. The loss starts to increase rapidly only when the magnitude of the thickness variation is great enough to incorporate the primary interference peak.

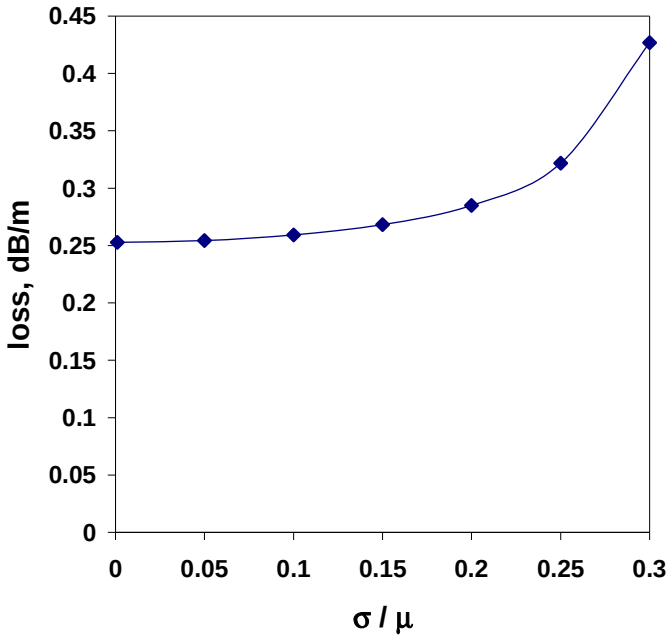

Figure II-33: The theoretical HE_{11} mode transmission loss for CH_3OH laser radiation at 119 μm propagating in Ag/PS-coated HGWs is plotted as a function of the magnitude of error, σ/μ, in the PS layer thicknesses, as measured by the standard deviation σ of each layer's thickness divided by it's optimum thickness. a = 900 μm and λ_o = 119 μm.

The interference peaks in the near infrared (NIR) spectrum of Ag/PS HGWs designed for THz radiation is very sensitive to film thickness uniformity. Small changes in thickness result in large phase shifts for wavelengths corresponding to the high order interference peaks observed in the NIR. The calculated NIR interference spectra of Ag/PS HGWs with d_d = 12.7 μm and layer error defined by σ/μ of 0, 0.1 %, 0.5 %, and 1 % are shown in **Figure II-34**. There is very little change in the NIR interference spectra going from 0 to 0.1 % layer error. At 0.5 % error the high order peaks beyond 6000 cm^{-1} begin to decompose. The NIR interference spectrum is essentially lost for a layer error of just 1%. The NIR interference spectra thus can be used as a metric to evaluate the uniformity of PS coatings for THz Ag/PS HGWs.

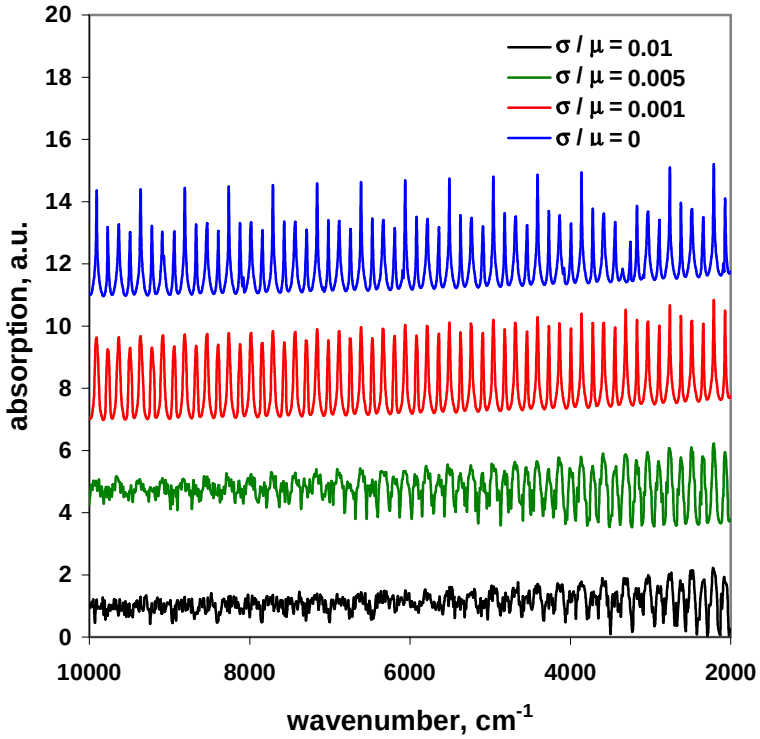

Figure II-34: The theoretical NIR absorption spectrum is plotted for Ag/PS-coated HGWs designed to transmit 119 μm radiation. Each curve represents a different magnitude of error σ/μ in the PS layer thicknesses. The curves are offset vertically for clarity. a = 900 μm and λ_o = 119 μm.

II.K Summary

The ray optics theory for HCWs is simple, intuitive, and is applicable to both HBFs and HGWs. The loss of the HE_{11} mode predicted by ray optics is consistant with the performance of the OmniGuide HBF and Ag/AgI HGWs operating at 10.6 μm reported in the literature. In this study, ray optics calculations are applied to hypothetical chalcogen based glass HBFs operating at 10.6 μm and metal/dielectric coated HGWs for 119 μm radiation. The refractive index and extinction coefficient of the dielectrics

layer(s) of both structures are critical to the fabrication of low loss waveguides. Minimum loss is achieved for HBFs when the refractive index contrast is maximized and the extinction coefficients of the layers are minimized. Incorporating additional layer pairs results in an exponential decrease in loss to the extent that loss is limited by the extinction coefficients of the layers. For metal/dielectric HGWs it is shown that silver provides the lowest theoretical losses at 119 μm. The optimum values of the dielectric's optical constants are interdependent. The lowest theoretical losses are possible when the extinction coefficient is low and the refractive index of the dielectric layer is between 1.3 and 2.0. The dielectric polystyrene meets this criterion. In theory a Ag/PS HGW with a 12.7 μm PS has an HE_{11} mode loss of 0.25 dB/m representing over an order of magnitude improvement with respect to an Ag-only HGW. The effect of layer thickness variation along the length of the waveguide is evaluated by calculating the change in loss upon the inclusion random variations in the layer thicknesses for both waveguide types. Chalcogen HBFs have smaller low loss spectral bands and are therefore more sensitive to errors in layer thickness than HGWs. The calculated loss of Ag/PS HGWs designed to transmit 119 μm radiation is insensitive to layer thickness errors up to σ/μ = 20 % whereas 5 % error causes a significant increase in the loss of chalcogenide HBFs designed for 10.6 μm radiation. The impact of layer error on the theoretical loss of either guide should not be prohibitive to their practical fabrication. These theoretical calculations provide sufficient evidence and motivation to proceed with the identification of suitable chalcogen based glasses for HBFs designed for low loss at 10.6 μm, as described in **Chapter 3,** and to fabricate and characterize Ag/PS HGWs designed to transmit 119 μm radiation as described in **Chapter 4**.

II.L References

1. E. Garmire, T. McMahon, and M. Bass, "Flexible infrared waveguides for high-power transmission," *IEEE J. Quantum Electron.*, Vol. QE-16, pp.23-32 (1980).

2. E. A. J. Marcatili and R. A. Schmeltzer, "Hollow metallic and dielectric waveguides for long distance optical transmission and lasers," *Bell Syst. Tech. J.*, Vol. 43, pp. 1783-1809 (1964).

3. M. Miyagi, A. Hongo, and S. Kawakami, "Transmission characteristics of dielectric-coated metallic waveguide for infrared transmission: slab waveguide model," *IEEE J. Quantum Electron.*, Vol. QE-19, pp.136-144 (1983).

4. M. Miyagi and S. Kawakami, "Design theory of dielectric-coated circular metallic waveguides for infrared transmission," *J. Lightwave Technol.*, Vol. LT-2, pp. 16-126 (1984).

5. M. Miyagi and S. Kawakami, "Losses and phase constant changes caused by bends in the general class of hollow waveguides for the infrared," *Appl. Opt.*, Vol. 20, pp. 4221-4226 (1981).

6. P. Yeh, A. Yariv, and E. Marom, "Theory of Bragg Fiber," *J. Opt. Soc. Am.*, Vol. 68, No. 9, pp. 1196-1201 (1978).

7. A. Argyros, "Guided modes and loss in Bragg fibers," *Opt. Express*, Vol. 10, No. 24, pp. 1411-1417 (2002).

8. Y. Xu, R. K. Lee, and A. Yariv, "Asymptotic analysis of Bragg fibers," *Opt. Lett.*, Vol. 25, No. 24, pp. 1756-1758 (2000).

9. S. Johnson, M. Ibanescu, M. Skorobogatiy, O. Weisberg, T. Engeness, M. Soljacic, S. Jacobs, J. Joannopoulos, Y. Fink, "Low-loss asymptotically single-mode propagation in large-core OmniGuide fibers," *Opt. Express*, Vol. 9, No. 13, pp. 748-779 (2001).

10. S. Guo, F. Wu, K. Ikram, and S. Albin, "Analysis of circular fibers with an arbitrary index profile by the Galerkin method," *Opt. Lett.*, Vol. 29, No. 1, pp. 32-34 (2004).

11. S. Guo, S. Albin, and R. Rogowski, “Comparative analysis of Bragg fibers,” *Opt. Express*, Vol. 12, No. 1, pp. 198-207 (2004).

12. Y. Fink, J. N. Winn, S. Fan, J. Michel, C. Chen, J. D. Joannopoulos, and E. L. Thomas, “A dielectric omnidirectional reflector,” *Science*, Vol. 282, pp.1679-1682 (1998).

13. J. N. Winn, Y. Fink, S. Fan, and J. D. Joannopoulos, “Omnidirectional reflection from a one-dimensional photonic crystal,” *Opt. Lett.*, Vol. 23, No. 20, pp. 1573-1575 (1998).

14. M. Miyagi, “Waveguide loss evaluation in circular waveguides and its ray optical treatment,” *IEEE J. Lightwave Tehnol.*, Vol. LT-3, pp. 303-307 (1985).

15. O. S. Heavens, “Optical properties of thin solid films,” Dover, (1995).

16. H. A. Macleod, “Thin film optical filters,” Taylor & Franics, (2001).

17. T. Katagiri, Y. Matsuura, and M. Miyagi, “All-solid single-mode Bragg fibers for compact fiber devices,” *J. Lightwave Technol.*, Vol. 24, No. 11, pp. 4314-4318 (2006).

18. M. Saito, S. Sato, and M. Miyagi, “Loss characteristics of infrared hollow waveguides in multimode transmission,” *J. Opt. Soc. Am. A*, Vol. 10, pp. 277-282 (1993).

19. B. A. E. Saleh and M. C. Teich, “Fundamentals of Photonics,” Wiley-Interscience (2007).

20. R. K. Nubling and J. A. Harrington, "Launch conditions and mode coupling in hollow glass waveguides," *Opt. Eng.*, Vol. 37, pp. 2454-2458 (1998).

21. R. George, "New dielectric thin film coatings for Ag and Cu coated hollow infrared waveguides," Ph.D. Thesis, *Rutgers University* (2004).

22. C. Katsidis and D. Siapkas, “General transfer matrix method for optical multilayer systems with coherent, partially coherent, and incoherent interface,” *Appl. Optics*, Vol. 41, No. 19, pp. 3978-3987 (2002).

23. D. L. Windt, “IMD – Software for modeling the optical properties of multilayer films,” *Comput. Phys.*, Vol. 12, No. 4, pp. 360-370 (1998).

24. Y. Matsuura, T. Abel, and J. A. Harrington, "Optical properties of small-bore hollow glass waveguides," *Appl. Optics*, Vol. 34, 6842-6847 (1995).

25. R. George and J. A. Harrington, “Infrared transmissive, hollow plastic waveguides with inner Ag-AgI coatings,” *Appl. Optics*, Vol. 44, No. 30 (2005).

26. B. Temelkuran, S. D. Hart, G. Benoit, J.D. Joannopoulos, Y. Fink, "Wavelength-scalable hollow optical fibres with large photonic band gaps for CO_2 laser transmission", *Nature*, Vol. 420, pp. 650-653 (2002).

27. MIT Photonic Bandgap Fibers and Devices Group, Database of Optical Constants, <http://mit-pbg.mit.edu/pages/database.html>.

28. C. Anastassiou, G. Dellemann, O. Weisberg, and U. Kolodny, “Fibers deliver CO_2 laser beams for medical applications,” *Photon. Spectra*, Vol. 38, No. 3, pp. 108-109 (2004).

29. E. Hecht, *Optics*, Addison Wesley, (2002).

30. L. P. Tate Jr. and Y. A. Elce, “Transedoscopic application of CO_2 laser irradiation using the OmniGuide fiber,” *Proc. SPIE*, Vol. 5686, No. 1, pp. 612-619 (2005).

31. D. Torres, O. Weisburg, G. Shapira, C. Anastassiou, B. Temelkuran, M. Shurgalin, S. A. Jacobs, R. U. Ahmad, T. Wang, U. Kolodny, S. M. Shapshay, Z. Wang, A. K. Devaiah, U. D. Upadhyay, J. A. Koufman, “OmniGuide photonic bandgap fibers for delivery of CO_2 laser energy for laryngeal and airway surgery,” *Proc. SPIE*, Vol. 5686, No. 1, pp. 310-321 (2005).

32. A. K. Varshneya, “Fundamentals of inorganic glasses,” Academic Press, (1993).

33. J. Hecht, “Understanding fiber optics,” Prentice Hall, (2005).

34. J. A. Harrington, “Infrared fibers and their applications,” SPIE, (2003).

35. M. G. Kuzyk, “Polymer fiber optics: materials, physics, and applications,” CRC, (2006).

36. E. D. Palik (ed.), “Handbook of optical constants of solids,” Academic Press, (1985).

37. K. Matsuura, Y. Matsuura, and J. A. Harrington, "Evaluation of gold, silver, and dielectric-coated hollow glass waveguides," *Opt. Eng.*, Vol. 35, pp. 3418-3421 (1996).

38. V. Gopal and J. A. Harrington, “Deposition and characterization of metal sulfide dielectric coatings for hollow glass waveguides,” *Opt. Express*, Vol. 11, No. 24, pp. 3182-3187 (2003).

39. Y. Shi, Y. Wang, Y. Abe, Y. Matsuura, M. Miyagi, and S. Sato, “Cyclic olefin polymer-coated silver hollow glass waveguides for the infrared,” *Appl. Optics*, Vol. 37, No. 33, pp. 7758-7762 (1998).

40. M. A. Ordal, L. L. Long, R. J. Bell, S. E. Bell, R. R. Bell, R. W. Alexander, Jr., and C. A. Ward, “Optical properties of the metals Al, Co, Au, Fe, Pb, Ni, Pd, Pt, Ag, Ti, and W in the infrared and far infrared,” *Appl. Optics*, Vol. 22, No. 7, pp. 1099-1119 (1983).

41. A. J. Gatesman, R. H. Giles, and J. Waldman, “High-precision reflectometer for submillimeter wavelengths,” *J. Opt. Am. Soc. B*, Vol. 22, No.2 (1995).

42. H. P. Roser, M. Yamanaka, R. Wattenbach, and G. V. Schultz, "Investigations of optically pumped submillimeter wave laser modes," International J. Infrared and Millimeter Waves, Vol. 3, pp. 839-868 (1982).

43. J. R. Birch, “The far-infrared optical constants of polypropylene, PTFE, and polystyrene,” *Infrared Phys.*, Vol. 33, No. 1, pp. 33-38 (1992).

44. K. Iwai, M. Miyagi, Y. Shi, and Y. Matsuura, “Uniform polymer film formation in hollow fiber by closed loop coating method,” *Proc. SPIE*, Vol. 6083, pp. 60830J1-60830J8 (2006).

Chapter III Chalcogenide Glass Hollow Bragg Fibers

III.A Background

The technology used to fabricate the OmniGuide HBF has produced fibers with near theoretical losses that are much lower than the loss of the materials from which the fiber is made. The high refractive index contrast of the OmniGuide HBF allows it to transmit CO_2 laser radiation with low loss, because the fields are largely confined to fiber's air core. However, the study of the OmniGuide HBF in Chapter II clearly indicates that its performance as a waveguide for CO_2 laser radiation is limited by the high extinction coefficient of PEI. To achieve a fiber with ultra low losses for CO_2 laser radiation, it is proposed that the fabrication techniques used to make Omniguide HBFs be applied to a pair of materials with similar refractive contrast, but much lower extinction coefficients at 10.6 μm. Chalcogenide and chalcohalide glasses are the only glassy materials that have the requisite thermal and optical properties for this application.

Chalcogenide glasses have non-oxide compositions that contain at least one of the elements S, Se, and Te. These chalcogen elements (group 16) are commonly alloyed with elements from groups 14 and 15, such as Ge and As, to form thermally stable glasses [1]. Mott's 8-*N* rule provides a good approximation of average coordination around each atom in chalcogenide glasses [2]. The chalcogen elements are generally two coordinated and have the ability to form homopolar bonds creating chain-like structures linking the higher coordinated atoms. This bonding behavior is responsible for the wide range of compositions that form chalcogenide glasses. In contrast, oxide glasses have stricter

stoichiometry. Chalcohalide glasses are formed by adding halogen (group 17) elements to chalcogenide glass compositions [3]. The halides act as chain ending units, decreasing the connectivity of glass, and hence have the effect of reducing the glass transition temperature.

Chalcogenide glasses are formed by melting together the pure elemental constituents in an inert atmosphere or more commonly in an evacuated ampoule. These special atmospheric conditions are needed to prevent contamination of the glass with oxide impurities, which have strong absorption bands in the infrared. The elimination of oxide impurities is critical when fabricating chalcogenide glasses for use in the transmission of infrared radiation [4]. Some of the common impurity absorption bands and intrinsic absorption bands are summarized in **Table III-1**. The raw materials for chalcogenide glass fabrication can be subjected to special purification measures like distillation or surface oxide removal to achieve low levels of oxide impurities. The melting procedure for the glasses examined in this study is described in Section III.E-1.

Chalcogenide glasses have unique optical, thermal, and electronic properties that have led to their use in numerous applications. Chalcogenide glasses have good IR transparency so they have been applied in transmission windows, optical fibers, and chemical sensors operating in the 2 - 12 μm spectral range [6-7]. The photo-induced amorphous to crystalline phase transition behavior of some chalcogenide glasses has led to applications in optical memory devices [8-9]. Rare earth doped chalcogenide fibers are of interest for infrared fiber amplifiers and lasers [10-11]. Amorphous Materials, Inc. is a commercial provider of optical fibers and optical components made from chalcogenide glasses such as $Ge_{33}As_{12}Se_{55}$ (AMTIR-1) and $As_{40}S_{60}$ (C-1) [12].

Type	Species	Absorption Peaks (μm)
Extrinsic	H_20	2.29, 2.32, 6.3, 10.7
	OH^-	2.73, 2.78, 2.84, 2.9, 2.92
	CO_2	4.26
	S-H	2, 2.05, 2.1, 2.55, 3.09, 3.64, 3.69, 4, 4.1
	Se-H	3.45, 3.55, 4.1, 4.3, 4.45, 4.5, 4.57, 4.7, 4.9, 14.4
	Te-H	5
	As-O	8.9, 9.1, 9.5, 9.6, 10.2, 10.4, 10.7, 12.5, 12.7, 13, 14.1
	Se-O	10.7
	Ge-O	11.1, 12.5, 12.7, 13
	Te-O	13.6, 14.4
Intrinsic	S-S	10.2
	Se-Se	10.5, 11.9, 13.5, 13.6, 14.4, 14.5
	As-Se	11.4

Table III-1: Absorption peaks of chalcogenide glasses.

It is challenging to identify glass compositions that have a high index contrast and transparency at a common wavelength because their transmission windows, the range of wavelengths between their electronic band edge and the multiphonon edge, tend to correlate strongly with refractive index. For instance, oxide glasses have low refractive indices and transmit in the visible to near-infrared while telluride glasses have very high refractive indices and transmit only in the mid to far infrared. Among chalcogenide glass forming systems only those based on Se and Te have low absorption at 10.6 μm. The refractive index of selenide glasses is generally greater than 2.6, while tellurides have

refractive indices greater than 2.8. Chalcohalide glasses have significantly lower refractive indices yet still maintain good IR transparency [13]. From an optical standpoint chalcohalide glass compositions are ideal for the low index material of a HBF operating at 10.6 μm, but the high vapor pressure of the halogen atoms is prohibitive to the deposition of stoichiometric chalcohalide thin films. Since thin film deposition is a key element of the HBF fabrication process only chalcogenide glasses with no halide doping are considered in this study. It is thus necessary to identify a low refractive index chalcogenide glass with a transmission window that extends beyond 10.6 μm, effectively limiting the search to selenium-based chalcogenide glasses.

This chapter is devoted to the identification of a pair of chalcogenide glasses that can be used in a HBF designed for low loss at 10.6 μm. The criteria for selecting the chalcogenide glass pair are:

1. The compositions must have high refractive index contrast for 10.6 μm radiation.
2. Both compositions must have low absorption (low k) at 10.6 μm.
3. The compositions must be co-drawable, which implies that they have similar glass transition temperatures, T_g, and high crystallization temperatures, T_x.

Upon the identification of a pair of chalcogenide glasses that meet these criteria, the basic elements of a preform fabrication and draw process for chalcogenide glass HBFs is demonstrated.

III.B Germanium Selenide Glass

Germanium selenide ($Ge_{1-x}Se_x$) glasses have unique thermal and optical properties that make them an excellent candidate for the low refractive index composition in a chalcogenide glass HBF. One of the earliest investigations of Ge-Se glasses focused on compositions around the stoichiometric compound $GeSe_2$ [14]. Unlike the analogous SiO_2 glass, $GeSe_2$ does not readily go into the glassy state. Tronc et al. obtained glasses with $0 \leq x \leq 0.4$ and found that compositions between pure selenium and $GeSe_2$ formed glasses most readily [15]. Phillips sought to explain these observations using his constraint theory of glass formation [16-18], which proposes that optimum glass formation is realized when the number of constraints placed on each atom by the surrounding glass network is equal to its spatial degrees of freedom (3 for a 3-dimensional network). This condition is satisfied when the average coordination number, $<r>$, of each atom is 2.4. **Figure III-1** shows the glass forming difficulty in the Ge-Se glass forming system plotted as a function of mol % Ge. The composition $Ge_{20}Se_{80}$ corresponds to $<r> = 2.4$ and is in the range of Ge-Se compositions that form glasses most readily. The T_g of Ge-Se glasses increases continuously with increasing germanium content and takes on values from 125 ºC to 223 ºC over the range $0.75 < x < 0.85$ [19]. It is reasonable to conclude that Ge-Se glasses could be used in a similar fabrication method as the OmniGuide fiber based upon their thermal stability and the similarity of their T_g to As_2Se_3, which has a T_g = 173 ºC [20].

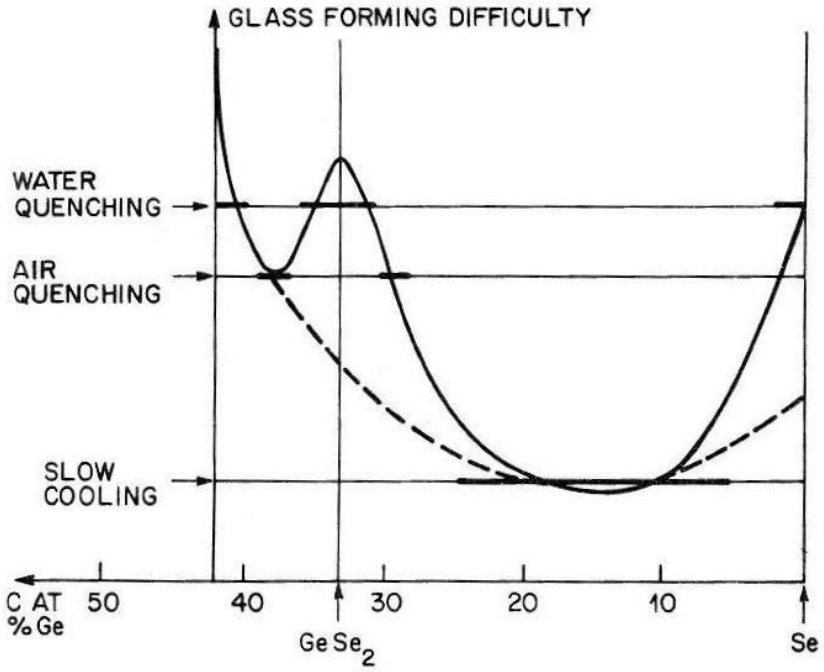

Figure III-I: The glass forming difficulty of Ge-Se glasses is plotted as a function of Ge content [17].

The transmission window of selenide-based glasses that are free of oxygen and hydrogen impurities typically extends beyond 10.6 μm, but their refractive indices are generally too high to be considered for the low refractive index material in an HBF. Ge-Se glasses have lower refractive indices than typical selenide glasses. The refractive indices of $Ge_{1-x}Se_x$ glasses reported by Nang et al. are plotted as a function of x in **Figure III-2** [21]. Ge-Se bonds have lower susceptibilities than either Se-Se or Ge-Ge, which explains the refractive index decrease upon the addition of Se to pure Ge, or Ge to pure Se. The fraction of Ge-Se bonds is maximized for the composition $GeSe_2$, which has a refractive index of 2.4 corresponding to the minimum value for Ge-Se glasses. The composition $Ge_{20}Se_{80}$ has a slightly higher refractive index of 2.46, but it is a much better

glass former. $Ge_{20}Se_{80}$ has a T_g of 152 °C [22] and does not crystallize below 422 °C [20]. Nishii measured a transmission loss, α, of 5.0 dB/m at 10.6 μm for a purified $Ge_{20}Se_{80}$ glass fiber [23]. Neglecting scattering losses, the extinction coefficient can be calculated from the transmission loss using the equation

$$k = \frac{(\alpha \cdot \lambda)}{(4 \cdot \pi)} \qquad \text{Eq.(III.1)}$$

where λ is the wavelength at which the absorption coefficient is measured [24]. Applying Eq.(III.1) to the transmission loss of $Ge_{20}Se_{80}$ glasses, an extinction coefficient of $9.7 \cdot 10^{-7}$ is calculated.

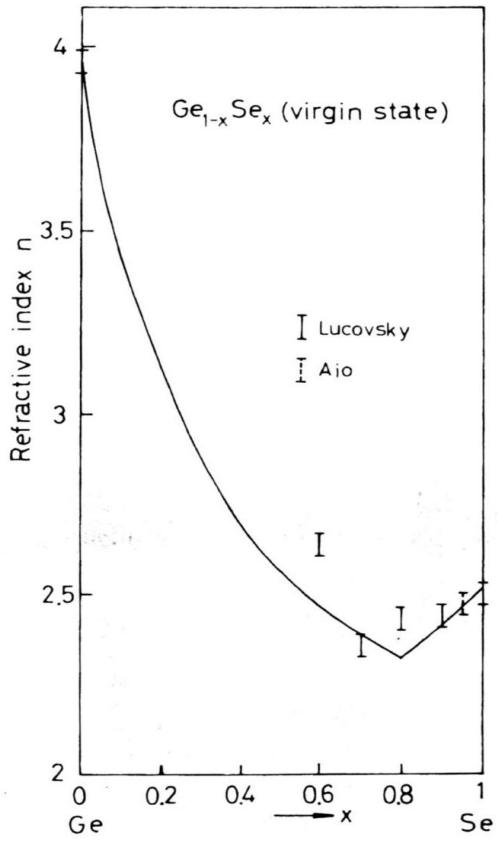

Figure III-2: The refractive index of $Ge_{1-x}Se_x$ glasses is plotted as a function of x [21].

The chalcogenide glass composition $Ge_{20}Se_{80}$ is an excellent glass former; has a relatively low refractive index among selenides based glasses; and has low transmission loss at 10.6 μm. Based upon this information, $Ge_{20}Se_{80}$ is proposed as the low refractive index composition for a chalcogenide glass HBF.

III.C Identifying High Refractive Index Chalcogenide Glasses

If n_L is taken as 2.45, n_H must be greater than 3.9 to equal the refractive index contrast of the OmniGuide fiber. The theoretical analysis in Section II.I indicates that a chalcogenide glass HBF with low materials absorption requires less refractive index contrast to achieve similar or even lower losses than the OmniGuide fiber. It is therefore not necessary to achieve an equal refractive index contrast to the OmniGuide fiber, but there are benefits to identifying a high refractive index composition to pair with $Ge_{20}Se_{80}$. One important benefit is a reduced number of layers pairs needed to achieve low loss.

The highest refractive index chalcogenide glasses are those containing the heavy elements like Sb, Te, Pb, and Tl, which are more polarizable than the lighter elements from the same groups. Glasses containing large mol fractions of these elements, however, tend to exhibit poor glass forming ability, not to mention high toxicity, thus limiting their usefulness for HBFs. Working with these elements requires sophisticated safety equipment that was not available for use in this study. Instead new high refractive index glass compositions that are free of Sb, Te, Pb, and Tl are sought.

Several models have been proposed in the literature to describe the dependence of refractive index, n, on density, ρ, of glasses [25]. **Figure III-3** shows n plotted as a

function of ρ for many chalcogenide glass compositions. The data for this plot is taken from the comprehensive chalcogenide glass texts of Borisova [20], Kokorina [4], and Popescu [26]. A linear fit to the data forced through the point, (n = 1, ρ = 0), has a slope of 0.36 and a correlation coefficient of 0.83. The refractive index of chalcogenide glasses is far less commonly reported than their density, but they are closely correlated. In the absence of optical property data, it is possible to identify potential high refractive index compositions in chalcogenide glass forming systems based upon their density.

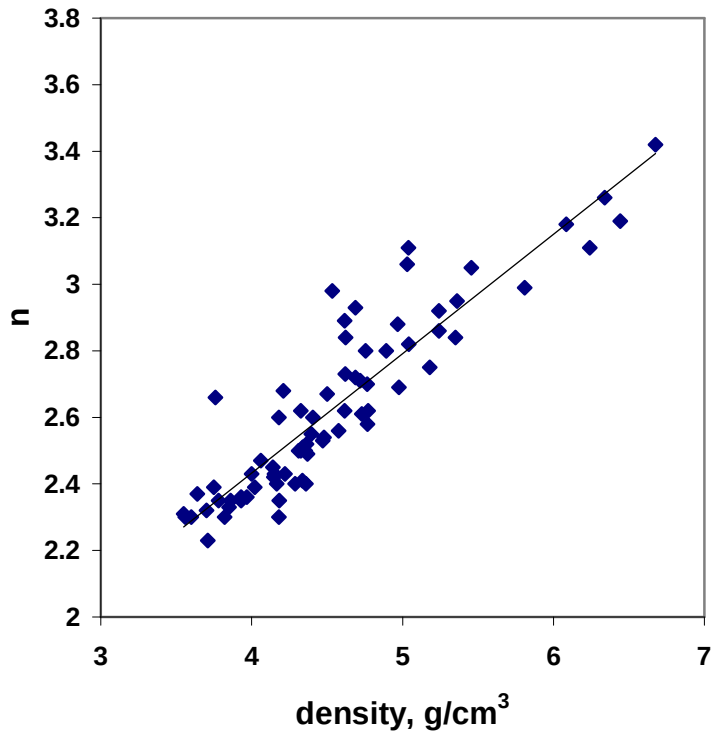

Figure III-3: The refractive indices of many chalcogenide glass compositions are plotted as a function of their density.

III.D Optical properties of Silver-Arsenic-Selenide Glasses

The Ag-As-Se system has high density and stable glass forming compositions with similar T_g to $Ge_{20}Se_{80}$, so it is logical to examine compositions in this system for possible use in chalcogenide HBFs. Glass forming in the Ag-As-Se system was first investigated by Kreidl and Patel [27]. Borisova and Rykova conducted a more detailed study and discovered two distinct regions of glass formation [28]. **Figure III-4** shows the glass forming regions in the Ag-As-Se system. The smaller of the glass forming regions contains compositions enriched with As and Ag that exhibit more stable glass formation than the compositions in the Se-enriched glass forming region. The T_g and T_x of these compositions are given in the ternary diagrams shown in **Figure III-5** and **Figure III-6**. The difference in T_g and T_x, denoted ΔT, is a good indication of the suitability of a glass composition for the fiber draw process. The glasses with high arsenic and silver content have high ΔT and similar T_g to $Ge_{20}Se_{80}$ indicating their potential to be co-drawn. The density of these glasses is close to 6 g/cm^3 indicating that their refractive index is likely to be greater than 3 based upon the correlation between the density and refractive index of chalcogenide glasses discussed in Section III.C. Borisova and Rykova's density and thermal analysis data are summarized in **Table III-2**. Of particular interest is the composition $Ag_{25}As_{41.7}Se_{33.3}$ that has ΔT = 159 °C, the highest of the glasses investigated, and a density of 5.93 g/cm^3.

Borisova's thermal and physical property data suggests that Ag-As-Se glasses are a good candidate for use with $Ge_{20}Se_{80}$ in a chalcogenide glass HBF, but there is very little data on the infrared optical properties of Ag-As-Se glasses in the literature. To

confirm the suitability of Ag-As-Se glass for use in an IR transmitting HBF several compositions in the Se-deficient region of glass formation are fabricated and characterized using Fourier Transform Infrared (FTIR) spectroscopy, CO_2 laser variable angle reflectometry (VAR), and CO_2 laser calorimetry.

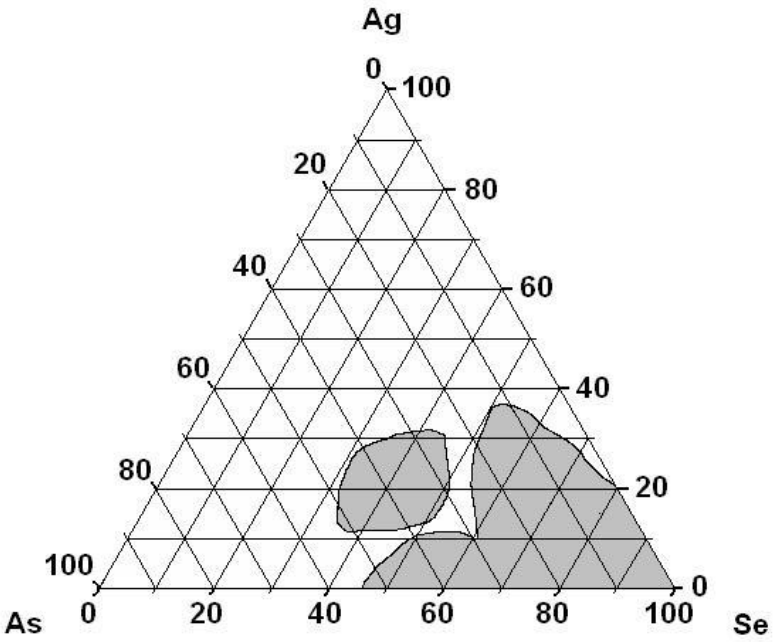

Figure III-4: The glass forming regions in the Ag-As-Se system [28].

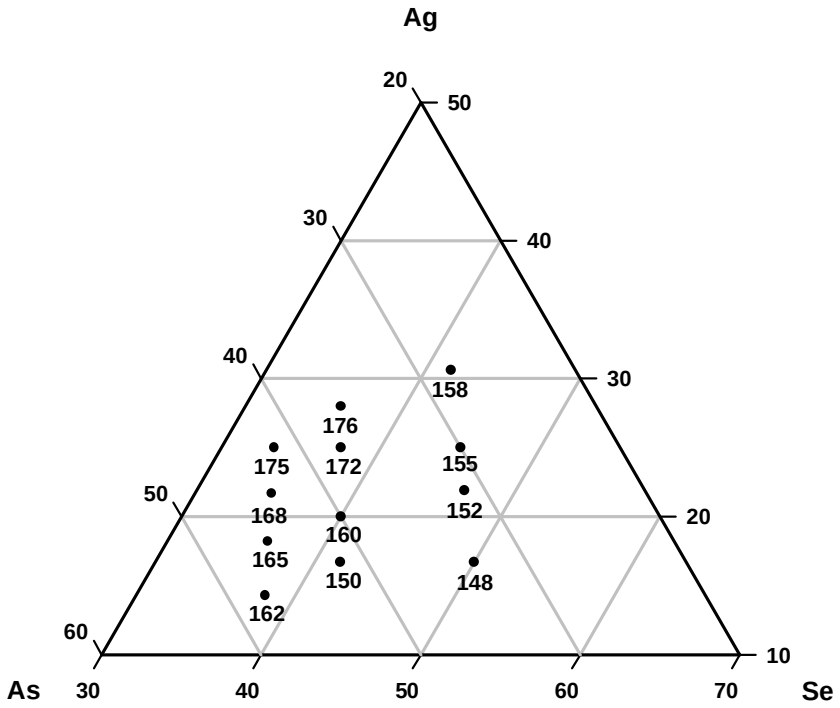

Figure III-5: The glass transition temperature is indicated for several compositions in the Se deficient region of Ag-As-Se glass formation [28].

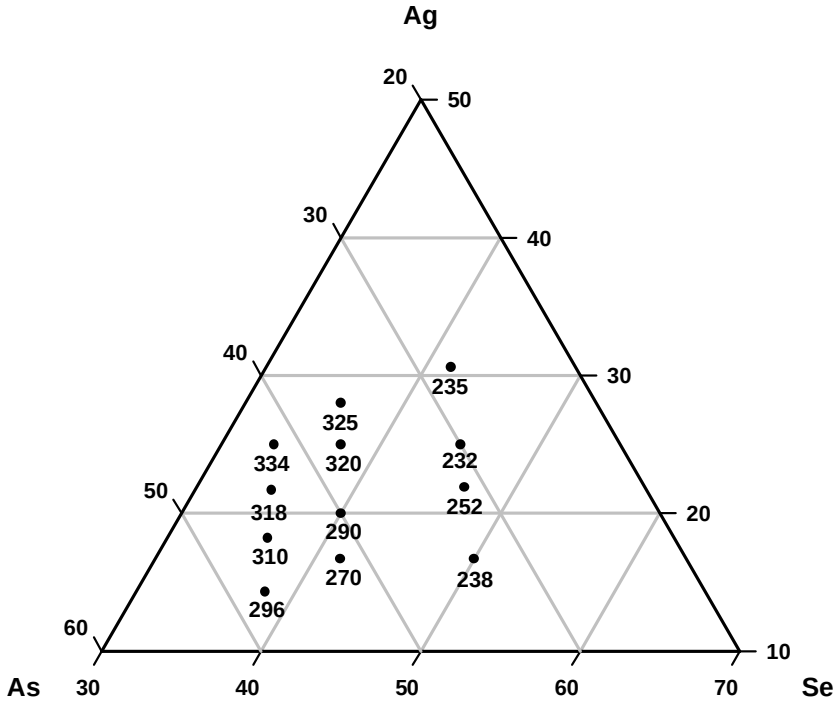

Figure III-6: The crystallization temperature is indicated for several compositions in the Se deficient region of Ag-As-Se glass formation [28].

Composition, mol %			ρ, g/cm^3	T_g, °C	T_x, °C	ΔT, °C
Ag	**As**	**Se**				
14.3	47.6	38.1	5.14	162	296	136
18.2	45.5	36.3	5.42	165	310	145
21.7	43.5	34.8	5.70	168	318	150
25	41.7	33.3	5.93	175	334	159
16.7	41.7	41.6	5.30	150	270	120
20	40	40	5.50	160	290	130
25	37.5	37.5	5.86	172	320	148
28	36	36	6.04	176	325	149
16.7	33.3	50	5.37	148	238	90
21.9	31.3	46.8	5.62	152	232	80
25	30	45	5.76	155	232	77
30	27.8	42.2	6.04	158	235	77

Table III-2: Density and thermal properties of Ag-As-Se glasses [20].

III.D-1 Glass fabrication

The first step in fabricating chalcogenide glasses for optical property measurements is purification of the raw materials. Distillation and surface oxide removal techniques are effective in reducing the extrinsic absorptions in chalcogenide glasses [29-30]. In this study, a surface oxide removal (SOR) treatment is performed on As and Ag, and Se is distilled before they are batched together and melted in an evacuated ampoule.

Figure III-7 shows a schematic diagram of the distillation furnace fabricated for use in this study. It consists of two furnaces stacked vertically and separated by sufficient insulating material to allow the top furnace to be maintained at a temperature that is several hundred degrees hotter than the bottom furnace. The distillation loop tube is passed through a small hole in the insulation at the bottom of the upper furnace. The distillation loop tube is fabricated from a 4' fused quartz tube, purchased from Technical Glass Products, Inc, with an outer diameter of 0.5" and wall thickness of about 1/16". First, the tube is divided into a 3' long section and a 1' long section using a propane-oxygen torch. The tube is rotated and gradually and twisted as it becomes viscous in the heat of the torch. Eventually the two sections can be separated forming tubes that are hermetically sealed on one end. The tubes are etched with a 10% HF solution in a fume hood for 20 minutes and then rinsed thoroughly with distilled deionized water. Upon drying in air, the 1' tube is reserved for use in the SOR treatment for Ag and As. The three foot tube is formed into a loop shape by heating small sections with the propane-oxygen torch and gradually bending the tube. The closed end of the tube extends about 6" below the loop, which is about 3.5" in diameter, and the open end extends about 8" above the loop. The distillation loop tube is transferred into an argon atmosphere glove box while it is still hot from the bending process to minimize the adsorption of water vapor. 25 g of 99.999 % purity 3 mm Se shot and 125 mg of 99.99% purity Mg metal strip, both purchased from Cerac, Inc., are added into the loop tube via its open end. The tube is capped and transferred out of the glove box where it is evacuated to 10^{-3} torr and backfilled several times with ultra-high purity (UHP) grade argon from Airgas, Inc.. Evacuation to at least 10^{-5} torr is typically preferred for the fabrication of infrared

transmitting chalcogenide glass, but a vacuum system capable of achieving this pressure was not available for use in this study. After the tube has been evacuated and backfilled three times it is evacuated once again and sealed above the loop and separated from the vacuum system using the propane oxygen torch. With the Se shot and Mg in the loop section, the distillation loop is placed in the dual zone furnace. The heat treatment schedules for the two furnace zones are given in **Table III-3**. Selenium vapors condense in the portion of the distillation loop that extends into the low temperature furnace zone leaving more refractory impurities like Si and C in the loop. The magnesium strip acts as an oxygen getter. Upon the completion of the heat treatment schedule, the distillation loop is removed from the furnace and quenched in air. The loop is transferred back into the glove box where it is broken open to remove the slug of purified selenium that is dark black metallic in color and has a glossy finish.

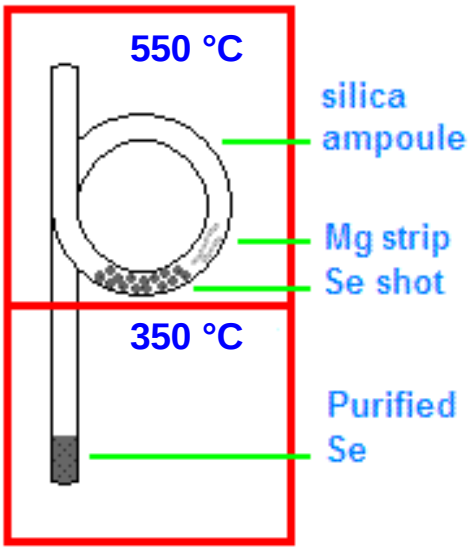

Figure III-7: A schematic diagram of the distillation furnace used to purify Se before chalcogenide glass batching.

Program step	Lower Zone			
	Type	**Set point, °C**	**Time. hr.**	**Rate, °C/min.**
1	ramp	350	-	5
2	hold	350	22.8	-
3	ramp	25	-	furnace cool
Program step	**Upper Zone**			
	Type	**Set point, °C**	**Time. hr.**	**Rate, °C/min.**
1	ramp	350	-	5
2	hold	350	3	-
3	ramp	550	-	5
4	hold	550	19.2	-
5	ramp	25	-	furnace cool

Table III-3: Selenium distillation heat treatment schedule.

The 1’ section of silica glass tubing reserved from the fabrication of the distillation loop is transferred into the Argon atmosphere glove box and filled with 25 g of either 99.99% purity 3 mm Ag shot or 99.9999 % purity 3-5 mm As lump and 250 mg of Mg strip, all purchased from Cerac, Inc.. The tube is capped and transferred out of the glove box where it is evacuated and backfilled with UHP Argon. After the tube has been evacuated and backfilled three times, it is evacuated once again and sealed approximately two inches above the portion of the tube where the Mg strip and As or Ag rest. The sealed ampoule is held upright in a furnace where it undergoes the heat treatment

schedule given in **Table III-4**. A schematic diagram of the SOR treatment furnace is shown in **Figure III-8**. While the furnace is held at 400 ºC the presence of the Mg strip creates a reducing atmosphere that removes the surface oxides from the As or Ag. Once the furnace is cooled the ampoule is removed and transferred to the glove box where it is broken to collect the purified material. The As lump is dull and black before the SOR treatment; after it is shiny and grey. Little change is observed in the Ag shot because there is limited surface oxide prior to the SOR treatment.

Program step	Type	Set point, ºC	Time. hr.	Rate, ºC/min.
1	ramp	400	-	5
2	hold	400	12	-
3	ramp	25	-	furnace cool

Table III-4: Ag and As SOR heat treatment schedule.

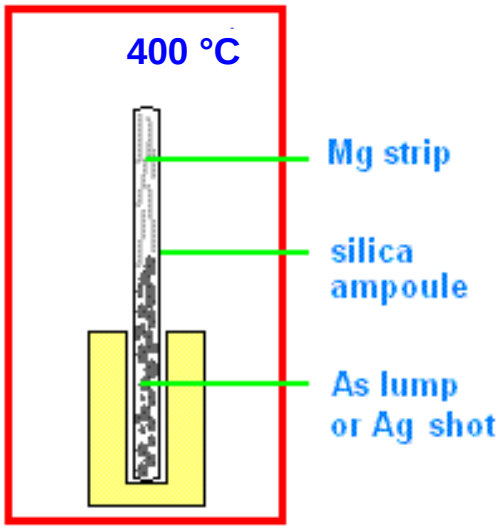

Figure III-8: A schematic diagram of the surface oxide removal furnace used to purify Ag and As before chalcogenide glass batching.

The following batch calculations are used to determine the mass of each of the purified elements required for a 15 g glass batch:

$$m_{Ag} = 15 \cdot \frac{[Ag] \cdot 107.9}{[Ag] \cdot 107.9 + [As] \cdot 74.92 + [Se] \cdot 78.96} \quad \text{Eq.(III.2)}$$

$$m_{As} = 15 \cdot \frac{[As] \cdot 74.92}{[Ag] \cdot 107.9 + [As] \cdot 74.92 + [Se] \cdot 78.96} \quad \text{Eq.(III.3)}$$

$$m_{Se} = 15 \cdot \frac{[Se] \cdot 78.96}{[Ag] \cdot 107.9 + [As] \cdot 74.92 + [Se] \cdot 78.96} \quad \text{Eq.(III.4)}$$

Each element is massed to greater than 0.1 % accuracy and placed in a 1' silica ampoule. After all three components are added to the ampoule it is transferred out of the glove box, evacuated and sealed using the same procedure described for the SOR treatment ampoules. The evacuated sealed ampoule is suspended in a rocking furnace, shown schematically in **Figure III-9**, using nichrome wire. The heat treatment schedule is given in **Table III-5**. The eutectic reactions in the Ag-As-Se system occur above 350 ºC, so a four hour hold at 450 ºC allows the more volatile Se to alloy with As and Ag, reducing the risk of the ampoule exploding as it is heated. The melt is maintained at a temperature of 975 ºC for 24 hours while the furnace is rocked to ensure homogenization. Upon completion of the 24 hr hold the furnace is turned upright and cooled to 650 ºC before the ampoule is removed and quenched in air. Before the glass is removed from its ampoule it is annealed at its T_g + 10 ºC for 24 hours and then cooled at a 1 ºC/min. The annealed glass is removed by carefully cracking the ampoule. The glass slug thus obtained is approximately 3 cm in length and is shiny dark grey metallic in color. **Figure III-10** shows a silica ampoule containing quenched Ag-As-Se glass and an annealed chunk of Ag-As-Se glass.

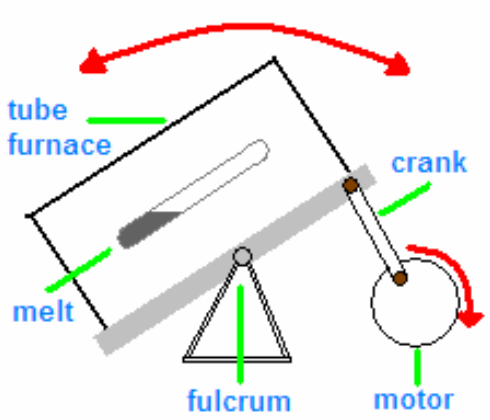

Figure III-9: A schematic diagram of the rocking furnace used to melt chalcogenide glasses.

Program step	Type	Set point, °C	Time. hr.	Rate, °C/min.
1	ramp	450	-	2
2	hold	450	4	-
3	ramp	975	-	2
4	hold	975	24	-
5	ramp	650	-	furnace cool
6	quench	25	-	air quench

Table III-5: Glass melting heat treatment schedule.

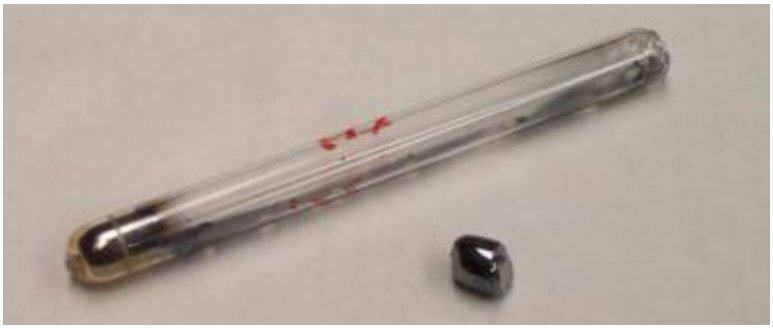

Figure III-10: A digital photograph of an ampoule (upper) used to melt chalcogenide glass compositions and a Ag-As-Se glass slug (lower).

III.D-2 Fourier Transform Infrared Spectroscopy

Fourier transform infrared (FTIR) spectroscopy is used to qualitatively analyze the infrared transparency of Ag-As-Se glasses. The analysis is performed on 3 mm plates with parallel polished faces. To obtain these plates, first a 5 mm section is cut from a 3 cm glass slug using a Buehler IsoMet low speed saw fitted with a 3" diameter X 0.006" wide diamond wafering blade. The faces are ground parallel using 600-grit SiC paper fixed to a low speed grinding wheel. Lapping oil is used as a lubricant instead of water to prevent modification of glass surface chemistry. The plates are ground with progressively finer grits up to 3000-grit. The final polishing step is accomplished using 0.03 μm alumina powder mixed with lapping oil on a polishing pad affixed to a stationary glass plate. The sample is traversed over the polishing pad in a figure-8 pattern creating a mirror finish. The samples thus obtained are 3 mm ± 0.1 mm in thickness with faces that are parallel to within 0.1º. A Thermo Nicolet Protégé 460 FTIR spectrometer with a tungsten glow bar source and DTGS KBr detector is used to obtain the transmission spectra of the Ag-As-Se plates in the 2.5 μm to 20 μm spectral range. The basic set-up of the FTIR for these measurements is shown in **Figure III-11**. First, a background spectrum is collected by measuring the spectral variation of the intensity passing through the sample holder's 5 mm aperture with no glass plate in place. The sample spectrum is collected with a glass plate centered on the aperture and held flush against it, so that its faces are perpendicular to the beam. The ratio of sample spectrum to the background spectra is calculated to determine the percent transmission of radiation through the sample as a function of wavelength. Five measurements are averaged for each sample.

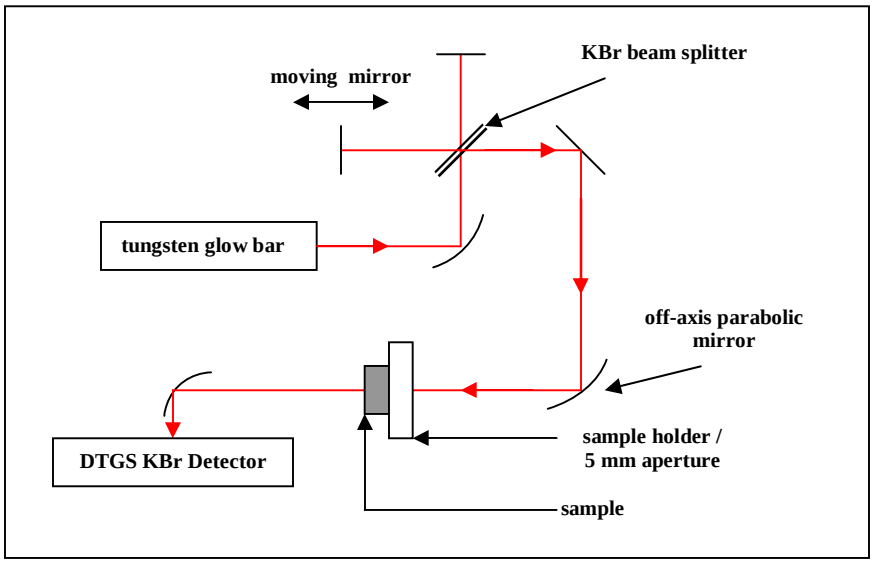

Figure III-11: A schematic diagram of the Nicolet Protégé 360 FTIR.

The infrared transmission spectra of $Ge_{20}Se_{80}$, $Ag_{25}As_{40}Se_{35}$, and $Ag_{15}As_{45}Se_{30}$ glasses are shown in **Figure III-12**. The intrinsic transmission window of $Ge_{20}Se_{80}$ extends from below 2 μm to about 16.5 μm. There are absorption peaks at 4.5 μm, 9.1 μm, and 13.2 μm. For $Ag_{25}As_{40}Se_{35}$ the intrinsic transmission window extends from below 2 μm to 18.1 μm, with absorption peaks at 9.3 μm, 12.7 μm, 13.5 μm, 15.2 μm, and 15.7 μm. The intrinsic transmission window of the $Ag_{20}As_{45}Se_{35}$ glass extends from 2.8 μm to 18.3 μm; this composition has absorption bands at 9.3 μm, 13.5 μm, 15.2 μm. The observed absorption peaks correspond to oxide impurity bands. The silver containing glasses have lower percent transmission than the Ge-Se glass because their refractive index is much higher and therefore have greater Fresnel reflection. The multiphonon edge and absorption peaks of the glasses examined in this study are given in **Table III-6**. There are no strong absorption bands at 10.6 μm for any Ag-As-Se glass or $Ge_{20}Se_{80}$, indicating the lost intensity at this wavelength is mainly due to Fresnel reflections and scattering. These glasses should have low extinction coefficients for CO_2 laser radiation.

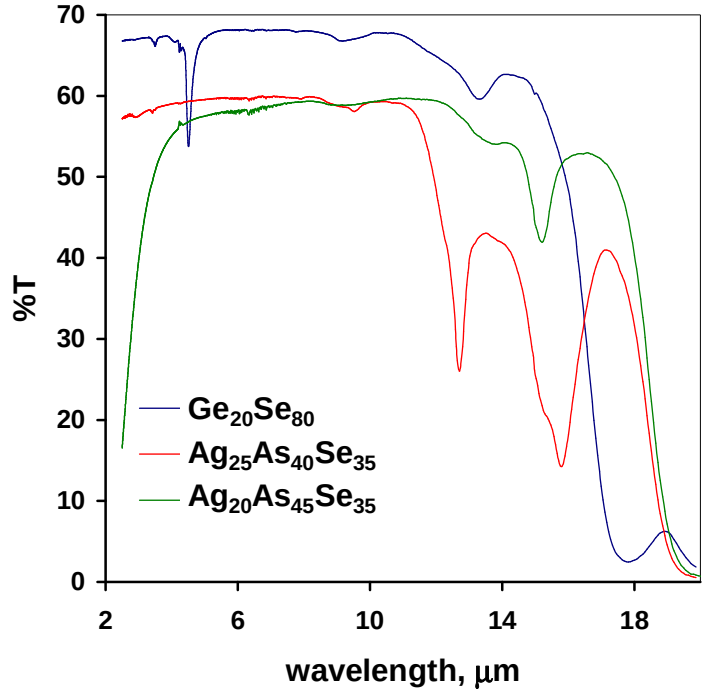

Figure III-12: The infrared transmission spectra of 3 mm thick chalcogenide glass plates.

Composition, mol %			Multiphonon edge, μm	Absorption peaks
Ag	As	Se		
18.3	43.3	38.4	20.1	13.6, 16.6
18.3	38.3	43.4	18.3	12.6, 13.5, 15.2
20	45	35	18.3	9.3, 13.5, 15.2
20	40	40	18.2	9.5, 12.7, 13.5, 15.2, 15.7
21.7	41.7	36.6	18.1	9.4, 12.7, 13.5, 15.2, 15.7
21.7	36.7	41.6	18.2	12.6 13.5, 15.2,
23.3	38.3	38.4	18.1	9.4, 12.6, 13.5, 15.2, 15.7
23.3	33.3	43.4	17.9	9.5, 12.6, 13.5, 15.2, 15.7
25	40	35	18.1	9.4, 12.7, 13.5, 15.2, 15.7
25	35	40	18.1	9.4, 12.6, 13.5, 15.7
26.7	36.7	36.6	18.0	9.4, 12.6, 13.5, 15.2, 15.7
26.7	31.7	41.6	18.1	9.5, 12.6, 13.5, 15.2, 15.8
28.3	33.3	38.4	17.9	9.4, 12.6, 13.5, 15.3, 15.7

Table III-6: Summary of FTIR results.

III.D-3 CO_2 Laser Variable Angle Reflectometry

Light incident on the interface between two dielectric materials is either reflected or transmitted. The reflectance, R, of the interface is defined as the ratio of the reflected power to the incident power. The polarization specific reflectances are R_p and R_s, where the subscripts s and p are used to distinguish between p-polarized and s-polarized radiation, respectively. The Fresnel equations describe the relationship of R_p and R_s to the refractive indices of the materials forming the interface and the angle of incidence, θ_0 [31]. The reflectance for s-polarization is given by

$$R_s = \left[\frac{n_0 \cdot \cos\theta_0 - n_1 \cdot \cos\left[\sin^{-1}\left(\frac{n_0}{n_1} \cdot \sin\theta_0 \right) \right]}{n_0 \cdot \cos\theta_0 + n_1 \cdot \cos\left[\sin^{-1}\left(\frac{n_0}{n_1} \cdot \sin\theta_0 \right) \right]} \right]^2 \qquad \text{Eq.(III.5)}$$

and the reflectance for p-polarization is given by

$$R_p = \left[\frac{n_1 \cdot \cos\theta_0 - n_0 \cdot \cos\left[\sin^{-1}\left(\frac{n_0}{n_1} \cdot \sin\theta_0 \right) \right]}{n_1 \cdot \cos\theta_0 + n_0 \cdot \cos\left[\sin^{-1}\left(\frac{n_0}{n_1} \cdot \sin\theta_0 \right) \right]} \right]^2 \qquad \text{Eq.(III.6)}$$

where n_0 is the refractive index of the dielectric medium from which the radiation is incident, n_1 is the refractive index of the material forming the interface with the incident medium. **Figure III-13** shows these equations plotted as a function of θ_0 for the cases where n_0 = 1 and n_1 = 2.8, and n_0 = 1 and n_1 = 3.2. In both cases R_s increases monotonically as the angle of incidence increases. R_p decreases with increasing angle of incidence up to the Brewster angle, $\theta_b = \tan^{-1}(n_1/n_0)$, and then increases to unity at

glancing incidence. Comparing the curves for each value of n_1 it is clear that the relative change in R_p is greater than the relative change in R_s, particularly for $25° < \theta < 65°$. Since R_p is so sensitive to changes in n_1, the refractive index of materials can be determined precisely by measuring the value of R_p over a range of angles and then fitting the data to Eq.(III.6). Stagg and Charalampopulos have reached similar conclusions in their study of the sensitivity of reflection techniques for the determination of the optical constants of bulk materials [32].

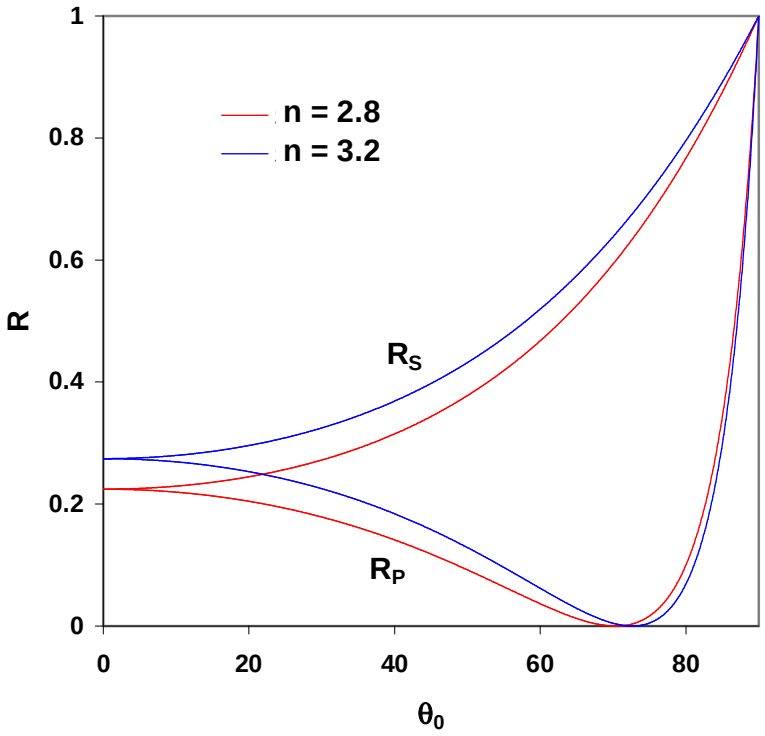

Figure III-13: R_s, and R_p are plotted as a function of θ_0 for the interface between air and dielectrics with n = 2.8 (red curves) and n = 3.2 (blue curves).

The refractive index of Ag-As-Se glasses at 10.6 μm is determined by fitting the dependence of R_p on the angle incidence for CO_2 laser radiation. The variable angle reflectometer used to determine R_p is shown schematically in **Figure III-14**. Radiation

emitted from the MPB CO_2 laser is polarized vertically. The rotating stage is oriented so that radiation striking the sample is polarized in the plane of incidence (p-polarization). The range of motion of the stage allows R_p to be measured from 25º to 65º. The 3 mm plates from FTIR measurements are used for these measurements as well. One face of the plate is dulled using 600-grit SiC paper to minimize reflections from the back face. Since the alignment is critical to obtain accurate reflectivity measurements, a special sample holder is used. The sample holder consists of a 1.5" X 1.5" X ¼" metal plate with a 1" diameter hole bored through it. Epoxy fixes a glass slide to its back surface. Enough modeling clay is placed in the bore of the plate on the glass slide, so that a sample placed upon it (the dull side in contact with the clay) rests slightly above the surface of the metal plate. The sample is pressed into the modeling clay using a flat surface covered with lens paper until it is flush with the surface of the metal plate. The process for aligning the sample in the plate is shown schematically in **Figure III-15**. The metal plate is held in three point contact with the rotating stage maintaining the alignment of the sample.

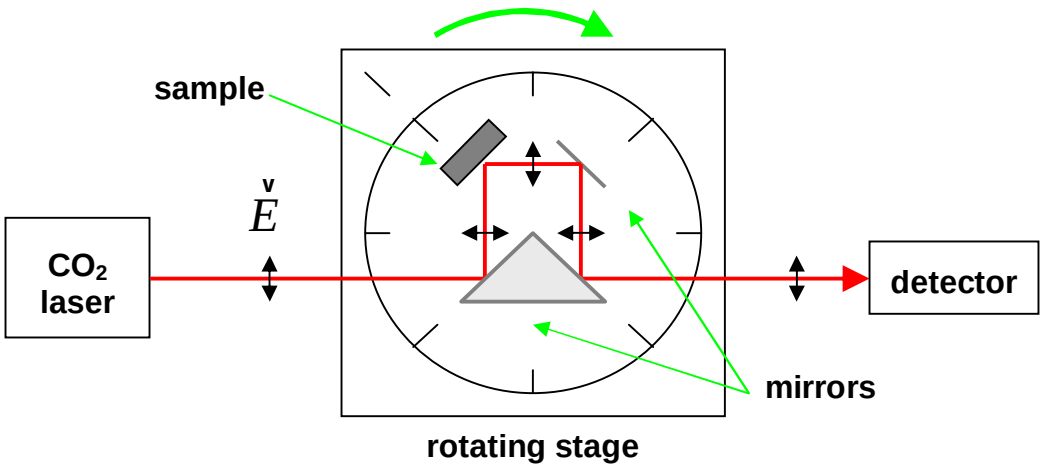

Figure III-14: A schematic diagram of a variable angle reflectometer.

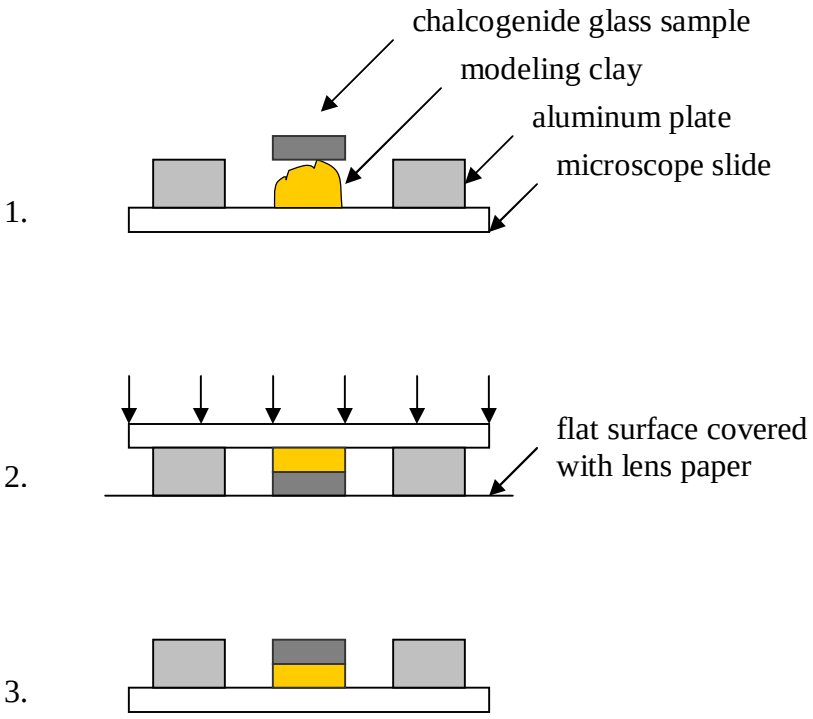

Figure III-15: The cross section of the VAR sample holder is shown schematically for each stage of the procedure used to align a chalcogenide glass sample.

The reflectometer is calibrated by measuring the power reflected by a silver mirror for θ_0 between 25º and 65º taken in 5º increments. The measured reflected power is divided by the theoretical R_p of silver, calculated using IMD v. 4.1, to determine the incident power for each value of θ_0. The power emitted by the CO_2 laser is ~17 W, but several gold screens were inserted in the beam path to reduce the power to about 1.60 W. A thermopile detector is used to measured the power reflected by the chalcogenide glass sample. Five measurements are performed on each chalcogenide glass sample for each θ_0. R_p is determined by dividing the average reflected power by the incident power. **Figure III-16** shows the measured dependence of R_p on θ_z for the composition $Ag_{25}As_{40}Se_{35}$. Least squares regression is used to fit the reflectance data to the Fresnel

equation while allowing the value of n_1 to vary. In this manner refractive indices are determined with a precision of 0.01.

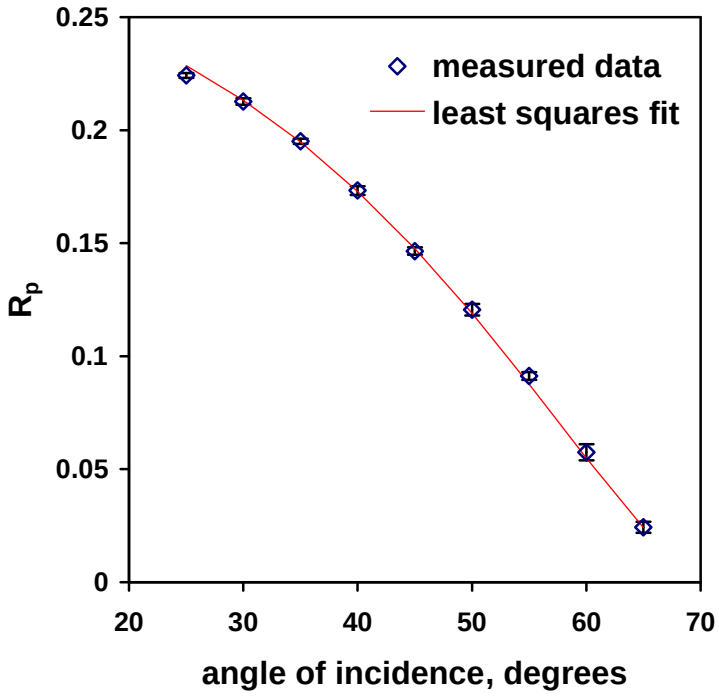

Figure III-16: R_p is plotted a function of the angle of incidence of $Ag_{25}As_{40}Se_{35}$ glass.

The refractive indices of the glass compositions examined in this study are indicated on the ternary diagram presented in **Figure III-17**. The refractive index at 10.6 μm generally increases with decreasing Se content at constant As to Ag ratios. Holding the As to Se ratio constant the refractive index increases with increasing Ag content. The highest refractive indices correspond to the compositions $Ag_{25}As_{40}Se_{35}$, n = 3.10, and $As_{26.7}As_{36.7}Se_{36.6}$, n = 3.11.

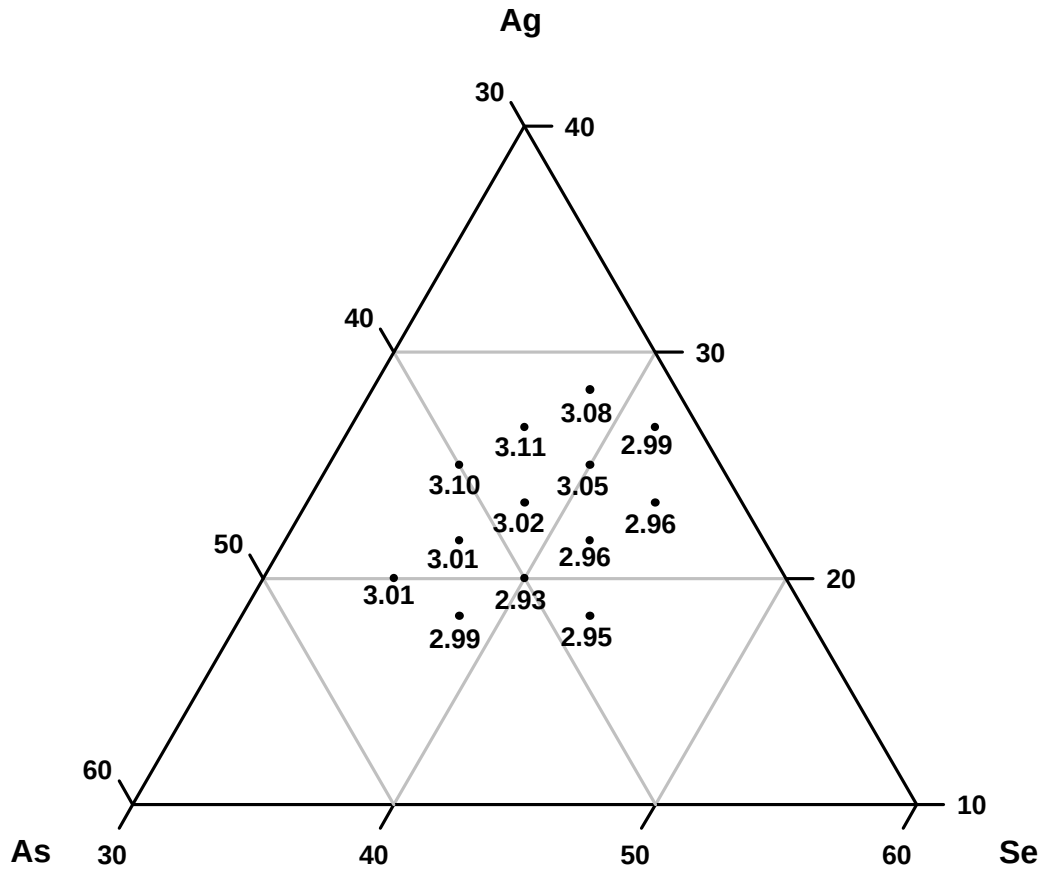

Figure III-17: The refractive indices of Ag-As-Se glasses are indicated on a ternary diagram.

III.D-4 CO_2 Laser Calorimetry

Considering Borisova's thermal property data, as well as the refractive index data and infrared transmission spectra collected in this study, the composition $Ag_{25}As_{40}Se_{35}$ meets the criteria stated in Section III.A for pairing with $Ge_{20}Se_{80}$ in a chalcogenide glass HBF. The refractive index contrast of this pair (3.10/2.46 = 1.26) is lower than that of the OmniGuide fiber. However, the theoretical calculations presented in Chapter II indicate that a chalcogenide glass HBF with low refractive index contrast may still have lower loss at 10.6 μm than the OmniGuide HBF because chalcogenide glasses have lower

extinction coefficients than PEI. To compare of the OmniGuide HBF to the proposed $Ge_{20}Se_{80}$ / $Ag_{25}As_{40}Se_{35}$ chalcogenide glass HBF, the extinction coefficient of the $Ag_{25}As_{40}Se_{35}$ glass must be determined.

The analysis in Section III.E-2 of the infrared transmission spectra of Ag-As-Se glasses indicates that they have low absorption at 10.6 μm, but FTIR spectroscopy does not provide the necessary precision to quantify the extinction coefficient. Laser calorimetry can be used to determine the absorption coefficient of very low loss materials in the infrared, including chalcogenide glasses [33-35]. Willamowski et al. review the various techniques for low loss bulk materials in detail [36]. The basic philosophy is to transmit laser radiation through a sample and measure the small temperature increase as the radiation is absorbed by the sample. The temperature of the sample is measured continuously while the laser radiation is transmitted though the sample and for several minutes after irradiation has ceased. The time of irradiation is denoted, t_p. The gradient method relates the absorption coefficient, α, to the sum of the slopes of the heating curve, $\left.\frac{dT}{dt}\right|_h$, and $\left.\frac{dT}{dt}\right|_c$ denotes the slope of the cooling curve. $\left.\frac{dT}{dt}\right|_h$ is measured at the time, $t_h = 0.8 \cdot t_p$ and $\left.\frac{dT}{dt}\right|_c$ is measured at the time, $t_c > t_p$, where $T(t_c) = T(t_h)$. The absorption coefficient, α [m^{-1}] is given by

$$a = \frac{n+1}{2 \cdot n} \cdot \frac{m \cdot c_p}{L \cdot P_T} \cdot \left(\left.\frac{dT}{dt}\right|_c + \left.\frac{dT}{dt}\right|_h \right) \qquad \text{Eq.(III.7)}$$

where n is the refractive index, m [kg] is the mass of the sample, c_p [$J \cdot kg^{-1} \cdot {}^oC^{-1}$] is the heat capacity, L [m] is the length of the sample, and P_T [W] is the transmitted power [36].

Figure III-18 shows a schematic diagram of the CO_2 laser calorimeter used to determine the extinction coefficient of $Ag_{25}As_{40}Se_{35}$ glass. A 14.7 mm glass rod with polished parallel faces is fabricated in a similar manner as the plates used for FTIR spectroscopic measurements. The calorimeter consists of brass box coated with an absorbing paint to reduce the effect of scattered radiation. The $Ag_{25}As_{40}Se_{35}$ glass rod is placed on a set of rails in the calorimeter that align it with the propagation direction of the CO_2 laser beam. A 20" focal length mirror is used to focus the beam into the center of the sample. A type-T differential thermocouple is used to measure the temperature increase of the $Ag_{25}As_{40}Se_{35}$ glass rod relative to the reference. The thermoelectric voltage, E [mV], is measured using a Keithley 181 nanovoltmeter. The relationship between the temperature, T [ºC], to the thermoelectric voltage of a type-T thermocouple is given by

$$T = d_0 + d_1E + d_2E^2 + \mathsf{K}\, d_7E^7 \qquad \text{Eq.(III.8)}$$

The coefficients d_0, d_1,…d_7 are called the inverse temperature coefficients. **Table III-7** gives the values of the inverse temperature coefficients for a type-T thermocouple [37-38]. A GPIB interface is used to continuously transfer the thermoelectric voltage data from the nanovoltmeter to a laptop computer. Initially, the CO_2 laser beam is blocked by a ceramic brick to permit the collection of a thermal background, which is averaged to establish an initial temperature. The ceramic block is removed for 120 seconds and the change in temperature is recorded continuously. The sample is allowed to reach thermal equilibrium between measurements; and the results of 10 measurements are averaged to determine the absorption coefficient.

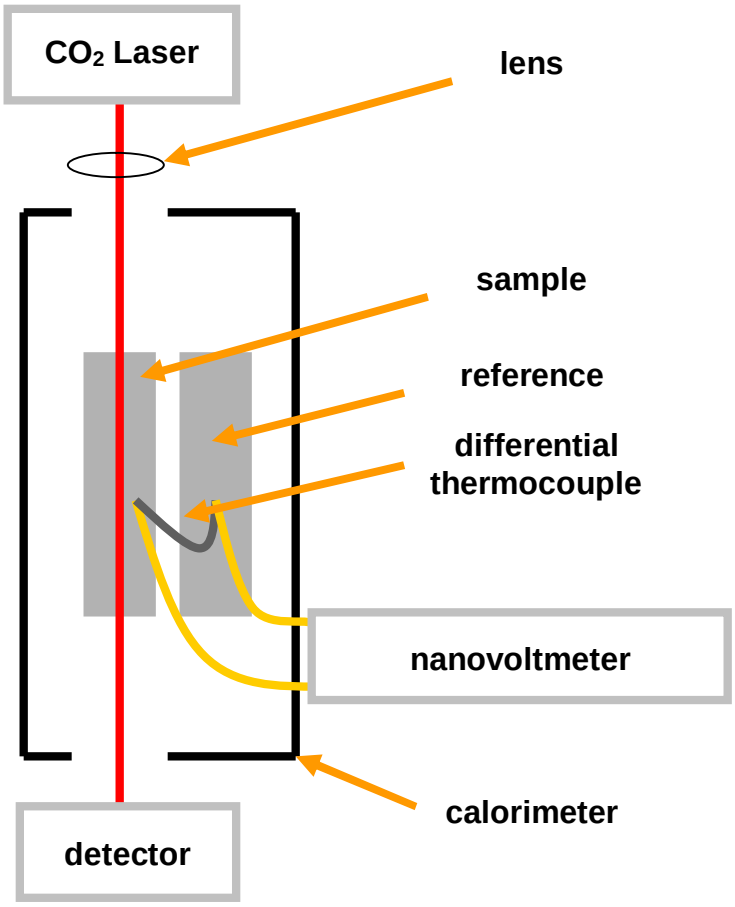

Figure III-18: A schematic diagram of a CO_2 laser calorimeter is shown.

Coefficient	Value
d_0	0
d_1	$2.5928 \cdot 10^{1}$
d_2	$-7.602961 \cdot 10^{-1}$
d_3	$4.637791 \cdot 10^{-2}$
d_4	$-2.165394 \cdot 10^{-3}$
d_5	$6.048144 \cdot 10^{-5}$
d_6	$-7.602961 \cdot 10^{-7}$
d_7	0

Table III-7: Inverse temperature coefficients of a type-T thermocouple for 0 °C to 400 °C.

Figure III-19 shows a plot of the change in temperature of the $Ag_{25}As_{40}Se_{35}$ glass rod as a function of time as it is irradiated by the CO_2 laser for 120 s and then allowed to cool. The slopes of the heating curve and cooling curve at t_h and t_c are indicated in red. The average power transmitted by the plate is 66 mW causing the temperature at the surface of sample to increase by 0.78 °C upon irradiation for 120 s. The value of α is calculated to be $1.16\times10^{-1} \pm 3\times10^{-2}$ m^{-1}. The extinction coefficient of $Ag_{25}As_{40}Se_{35}$ glass is $9.8\times10^{-6} \pm 0.3\times10^{-6}$, obtained by substituting α into Eq.(III.1). This value is higher than that of $Ge_{20}Se_{80}$ as determined by Nishii [23], but several orders of magnitude lower than PEI.

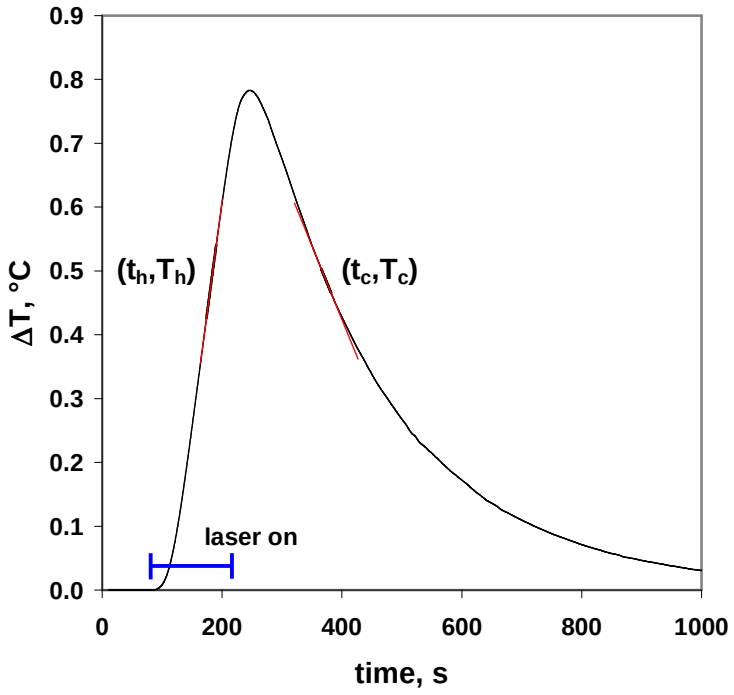

Figure III-19: ΔT is plotted as a function of time for a 14.7 mm $Ag_{25}As_{40}Se_{35}$ glass rod irradiated with CO_2 laser radiation for 120 s.

III.E Theoretical Analysis of a Ge-Se/Ag-As-Se Hollow Bragg Fiber

As a result of the studies described in Sections III.B through III.D the compositions $Ge_{20}Se_{80}$ and $Ag_{25}As_{40}Se_{35}$ have been identified as forming a pair that meets the thermal and optical property requirements for application to a chalcogenide glass HBF. The complex refractive indices of $Ge_{20}Se_{80}$ and $Ag_{25}As_{40}Se_{35}$ are $2.46 - i\cdot 9.7\cdot 10^{-7}$ and $3.10 - i\cdot 9.8\cdot 10^{-6}$, respectively. This pair of glasses has lower contrast than the OmniGuide Bragg fiber, meaning that more layers will be necessary to achieve the same loss. However, the decrease in loss upon the addition of layer pairs is limited to approximately 7 layer pairs for the OmniGuide HBF, whereas many more layer pairs are effective in reducing the loss of the hypothetical chalcogenide glass HBFs analyzed in Section II.I.

The ray optics method is used to calculate the HE_{11} mode loss of 10.6 μm radiation propagating in 700 μm bore diameter $Ge_{20}Se_{80}$ / $Ag_{25}As_{40}Se_{35}$ and PEI / As_2Se_3 (OmniGuide) HBFs as a function of the number of layer pairs, *N*. First, the reflectivity for radiation propagating at the HE_{11} mode angle, given by Eq.(II.7), is calculated using the impedance transfer matrix method described in Section II.E. These values are substituted into Eq.(II.9) to determine the HE_{11} mode loss. **Figure III-20** shows the calculated HE_{11} mode loss for the $Ge_{20}Se_{80}$ / $Ag_{25}As_{40}Se_{35}$ HBF and the Omniguide HBF plotted as a function of *N*. The loss of the OmniGuide HBF is lower when *N* is less than 5. Around $N = 6$ the two HBFs have similar calculated losses. Beyond $N = 7$ the loss of the chalcogenide glass HBF continues to decrease exponentially while the loss of the OmniGuide fiber remains relatively constant. The observed behavior can be explained by

considering the relative contributions of materials absorption and leakage loss to the overall loss of the waveguide. Below $N = 5$ the loss of both waveguides is dominated by leakage through the Bragg reflector film. In this regime, the OmniGuide HBF has lower loss because it has a higher refractive index contrast, and therefore greater confinement of the HE_{11} mode. Above $N = 6$ the loss of the Omniguide HBF is dominated by materials absorption. There is very little materials absorption for the chalcogenide glass Bragg fiber, so its loss continues to be dominated by leakage even up to 15 layer pairs. Since the leakage decreases exponentially with the addition of each layer pair the loss of the chalcogenide HBF also decreases exponentially. The calculated loss of the $Ge_{20}Se_{80}$ / $Ag_{25}As_{40}Se_{35}$ and Omniguide HBFs with $N = 15$ are $4.9 \cdot 10^{-3}$ dB/m and $1.8 \cdot 10^{-1}$ dB/m, respectively.

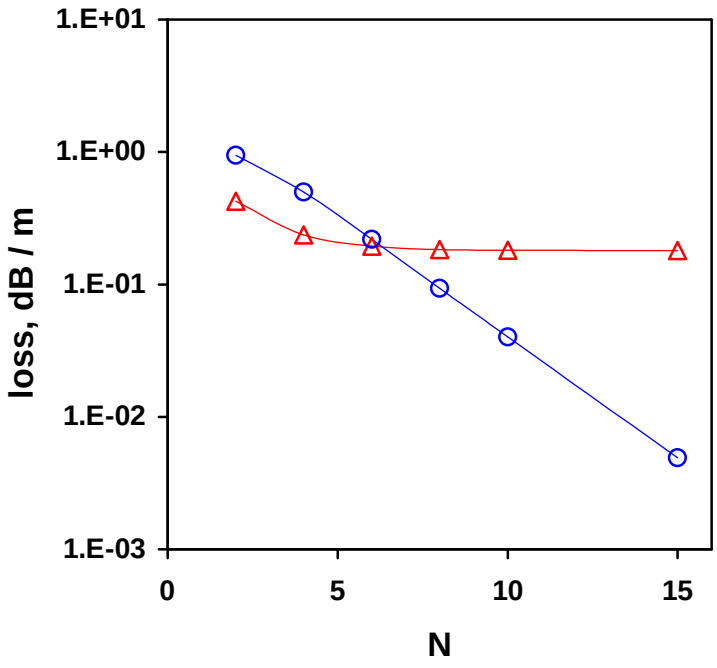

Figure III-20: The transmission loss of the HE_{11} mode is plotted as a function of N for CO_2 laser radiation propagating in a As_2Se_3 / PEI (red) Omniguide HBF and a $Ag_{25}As_{40}Se_{35}$ / $Ge_{20}Se_{80}$ (blue) HBF. $a = 350$ μm and $\lambda_o = 10.6$ μm.

It is concluded that a chalcogenide glass HBF consisting of at least seven $Ge_{20}Se_{80}$ / $Ag_{25}As_{40}Se_{35}$ layer pairs could have improved performance over the OmniGuide HBF for the transmission of CO_2 laser radiation. To realize this improvement, a fabrication method must be developed for chalcogenide glass HBFs that is capable of achieving similar microstructure precision to that which is possible using the OmniGuide HBF fabrication process.

III.F Chalcogenide Glass HBF Preform Fabrication and Drawing

Chalcogenide glasses are investigated for application to HBFs both for their optical and thermal properties. Fiber drawing is a key aspect of the OmniGuide HBF fabrication process because it allows precise control of HBF microstructure; long lengths of fiber can be made continuously; and fibers designed for many different wavelengths can be drawn from a single preform [39]. A free standing chalcogenide glass thin film is too brittle to be rolled into a preform, as is done with an As_2Se_3 coated PEI thin film to make the OmniGuide preform. A new technique must be developed to make a drawable chalcogenide glass HBF preform.

Chalcogenide glass thin films have been obtained by physical vapor deposition (PVD) techniques, including thermal evaporation, sputtering, and pulsed laser deposition [40-45]. A comparison of the film stoichiometry, film uniformity, and deposition rates that are characteristic of each PVD process are given in **Table III-8 [**46]. Film stoichiometry is important because small changes in the composition of the film can change the optical and thermal properties significantly. The importance of film

uniformity is discussed in Section II.I-4. A high deposition rate is needed to deposit films with thicknesses that are in proportion to the bore diameter of the preform taking into account the desired bore diameter of the HBF. For instance, the film thickness of a $Ge_{20}Se_{80}$ layer of an HBF designed for low loss at 10.6 μm is 1.18 μm; thus the $Ge_{20}Se_{80}$ layers of a 12 mm bore diameter preform that will be drawn into a 700 μm bore diameter fiber must be 1.18·12/0.7 = 20.2 μm thick. The slow deposition rates of sputtering and PLD may be prohibitive to their application in fabricating chalcogenide glass HBFs. These methods also require sophisticated equipment, whereas a rudimentary thermal evaporation system can be fabricated using a simple vacuum chamber and a heat source.

PVD Process	**Deposition Rate** $\mathring{A}/s$	**Film Stoichiometry**	**Film Uniformity**
Thermal Evaporation	15-300	Fair	Good
Sputtering	1-10	Good	Excellent
Pulsed Laser Deposition	1-20	Good	Poor

Table III-8: A comparison of PVD techniques.

The chalcogenide glass HBF preform fabrication process demonstrated in this study is inspired by the Omniguide HBF fabrication process and two waveguide fabrication techniques demonstrated by researchers from Tohoku Univeristy. Miyagi et al. fabricate germanium coated nickel hollow waveguides by first sputtering a germanium thin film on the outside of an aluminum mandrel; nickel is electroplated onto the Ge film; and finally the aluminum mandrel is dissolved using a NaOH solution [47]. An AsS_3 cladding is applied to the surface of an As_2S_3 rod by a thermal evaporation

technique described by Saito et al. [48]. The As_2S_3 rod is suspended in a glass chamber containing AsS_3 glass that is locally heated so that it evaporates and condenses on the As_2S_3 rod to form a low index cladding.

A simple thermal evaporation system is constructed to deposit chalcogenide glass films onto a water cooled aluminum substrate tube as shown schematically in **Figure III-21**. To deposit a chalcogenide glass layer, first the glass is crushed and dispersed along the bottom of the 10" deposition zone in the fused silica evaporation chamber. A ¼" diameter aluminum substrate tube is suspended above the chalcogenide glass and sealed within the chamber using differentially pumped rotational vacuum fittings. During the deposition process the tube is rotated at 5 RPM while cooling water (~0 °C) flows along its axis at a rate of 1 L/min. A turbo pump draws vacuum on the chamber as it is heated at a rate of 5 °C/min. to a 150 °C. This temperature is held for 1 hour to eliminate physically adsorbed water molecules from the chamber walls. The furnace is then heated at 10 °C/min. to the final deposition temperature of 400 °C – 500 °C. The furnace is held at the final deposition temperature for 4 hours to ensure that all of the material has been deposited on the aluminum substrate. This process is repeated to build up alternating layers of different chalcogenide glass compositions. The thickness of the layers is determined by the mass of the glass dispersed in the bottom of the fused silica chamber.

The fabrication of a mechanically stable all-chalcogenide glass HBF preform would require the deposition of an impractical number of layers. Instead, the chalcogenide glass films and aluminum substrate tube are covered with a thick PEI coating to provide mechanical support for the chalcogenide films. A 12" X 36" X 0.003" thick PEI film is

rolled onto the substrate forming a 1/16 inch thick coating that covers a 12 inch long section of the tube. The last layer of the polymer coating is tacked in place using a soldering iron. The coating is consolidated under vacuum by placing it in an evacuated fused silica tube and then passing a small hot zone tube furnace set at ~260 °C along the length of the coated substrate at a rate of 1 cm/min. This consolidation furnace is illustrated in **Figure III-22**. The portions of the aluminum substrate tube that extend beyond the consolidated PEI are cut off and the remaining aluminum is dissolved by submersing it in a 3 M hydrochloric acid solution. The chalcogenide glass film remains bonded to the PEI film when the dissolution of aluminum is complete. The chalcogenide coated PEI tube is drawn at a temperature ~305 °C at a draw rate of about 1 m/min., producing tens of meters of hollow fiber from each preform. A draw furnace with a small ~1 cm hot zone is used to minimize collapse of the air core.

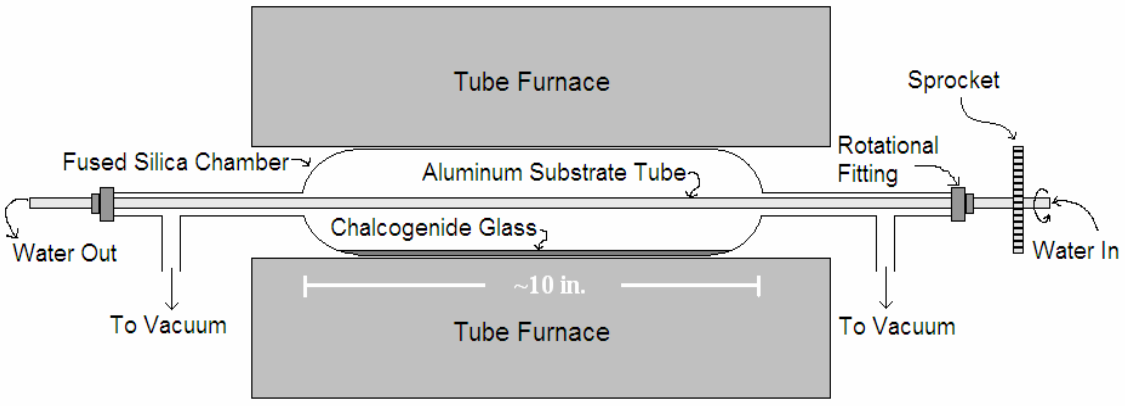

Figure III-21: A schematic diagram of the thermal evaporation set-up used to deposit chalcogenide glass films on the outside of a rotating aluminum tube.

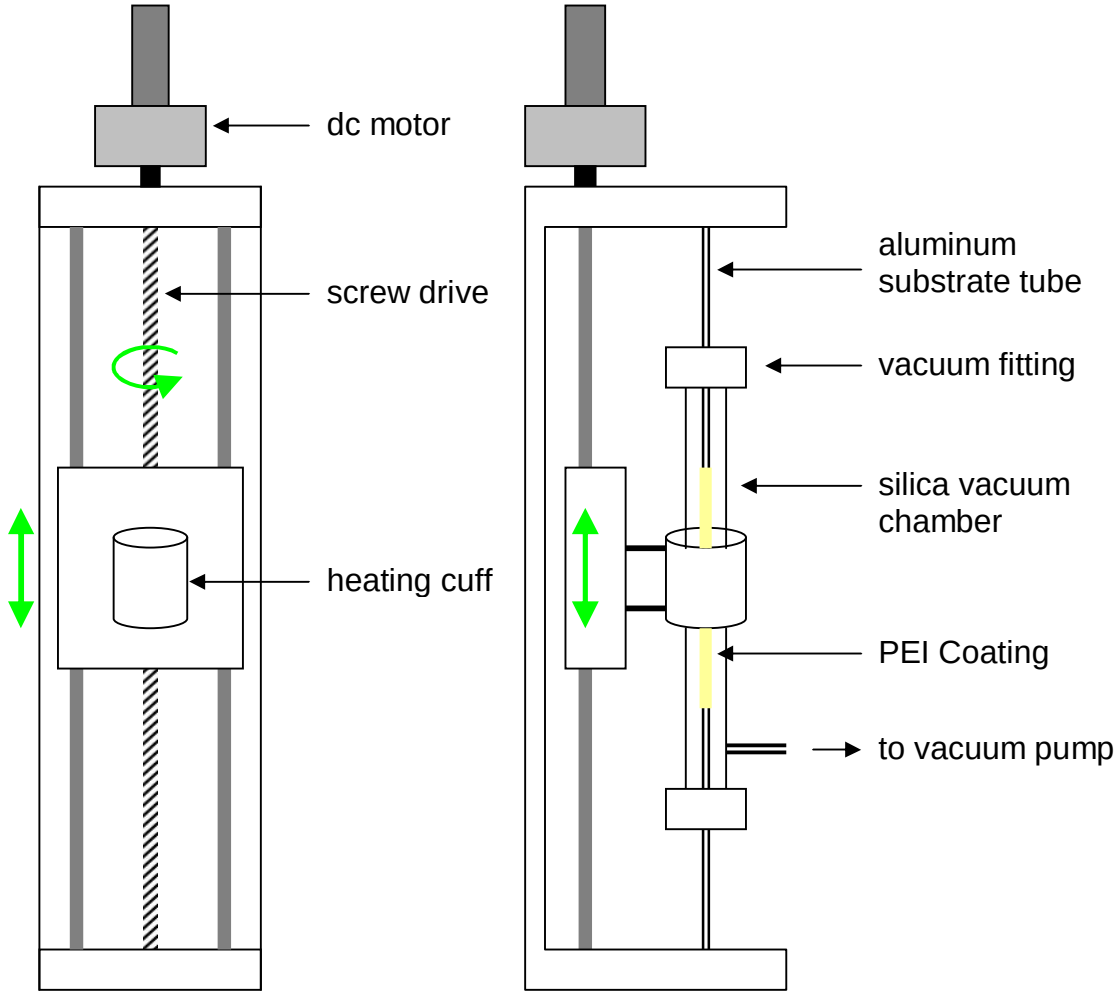

Figure III-22: A schematic diagram of the front (left) and side (right) of the polymer cladding set-up used to consolidate PEI films to form a protective coating for chalcogenide glass films deposited on the outside of and aluminum mandrel.

Figure III-23 shows an optical micrograph of the cross section of an aluminum substrate tube upon which three chalcogenide glass layers ($As_{40}Se_{60}$ – $Ge_{20}Se_{80}$ – $As_{40}Se_{60}$) have been deposited. The thicknesses of the films are uniform around the circumference of substrate and their interfaces are well defined. The outermost layer is

partially obscured by the epoxy in which the sample is mounted. $Ag_{25}As_{40}Se_{35}$ glass can not be deposited using this thermal evaporation system because silver has a much lower vapor pressure than As or Se. The molten glass in the evaporation chamber becomes increasingly concentrated in Ag as As and Se evaporate, which leaves a crystalline deposit that has a high silver content. $As_{40}Se_{60}$ is used in place of $Ag_{25}As_{40}Se_{35}$ to demonstrate that layers with different compositions can be deposited on top of one another. A more sophisticated thermal evaporation system incorporating separately heated boats for each element would be required to deposit $Ag_{25}As_{40}Se_{35}$ layers with the correct stoichiometry.

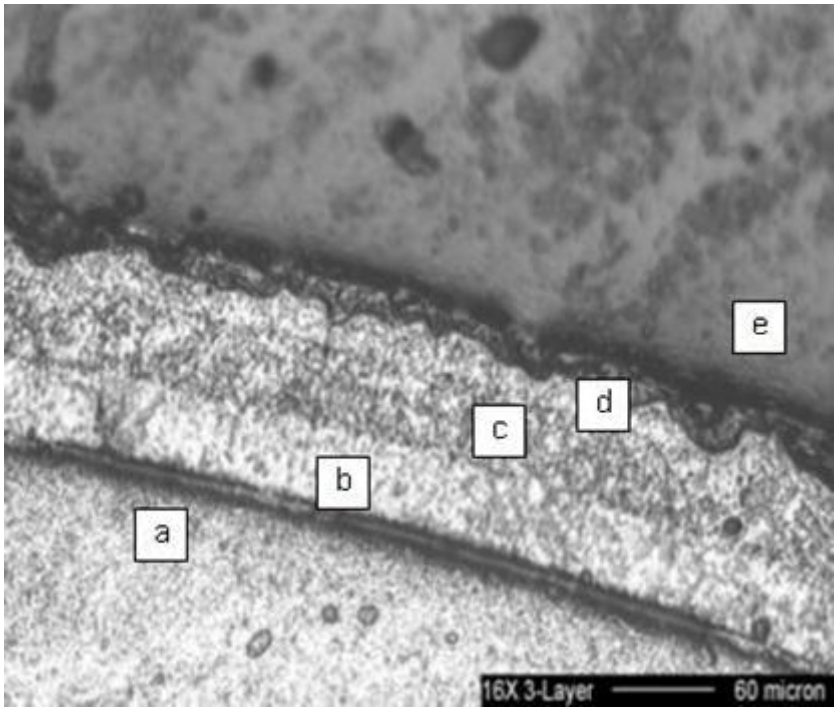

Figure III-23: A reflected light micrograph of the cross section of an aluminum substrate tube (a) with three layers; $As_{40}Se_{60}$ (b), $Ge_{20}Se_{80}$ (c), and $As_{40}Se_{60}$ (d) mounted in epoxy (e).

Figure III-24 shows the undrawn portion of a preform that consists of a single layer of $Ge_{20}Se_{80}$ coated with PEI. The preform is yellow and translucent where the PEI coating extends beyond the chalcogenide glass film. A short length of fiber drawn from this preform and split along its axis is shown in **Figure III-25**. The bore diameter and outer diameter are 200 μm and 460 μm, indicating a moderate collapse of the air core relative to the aspect ratio of the preform. The $Ge_{20}Se_{80}$ film appears to be smooth and is bonded uniformly to the PEI coating.

Figure III-24: A digital photograph of a hollow fiber preform consisting of a 1/4" inner diameter 1/16" wall thickness PEI tube with an inner $Ge_{20}Se_{80}$ coating.

Figure III-25: An optical micrograph of the cross section of a hollow PEI fiber with an inner $Ge_{20}Se_{80}$ coating. The fiber's inner and outer diameters are 200 μm and 460 μm, respectively.

II.G Summary

Chalcogenide glasses have unique optical and thermal properties that make them a good candidate for application to the fabrication of a CO_2 laser radiation transmitting HBF. Ge-Se and Ag-As-Se glasses are investigated to identify a pair of glass compositions with high refractive index contrast, low extinction coefficient at 10.6 μm, and appropriate T_g and T_x for application to the fiber draw process. The pair of glasses $Ge_{20}Se_{80}$ and $Ag_{25}As_{40}Se_{35}$ has the best combination of these properties among Ge-Se and Ag-As-Se glasses. Ray optics calculations are used to compare theoretical loss of CO_2 laser radiation propagating in a $Ge_{20}Se_{80}$ / $Ag_{25}As_{40}Se_{35}$ HBF to the loss of the OmniGuide HBF. These calculations show that the theoretical loss of the all chalcogenide HBF is significantly lower than the OmniGuide HBF for microstructures consisting of at least 8 layer pairs. The basic elements of a chalcogenide HBF fabrication process are demonstrated including depositing chalcogenide glass thin films on a rotating aluminum substrate tube by thermal evaporation, adding a thick PEI cladding for mechanical support, dissolving the substrate tube, and drawing the chalcogenide film / PEI preform into a hollow fiber.

III.H References

1. A. K. Varshneya, "Fundamentals of inorganic glasses," Academic Press, (1993).

2. N.F. Mott, "Conduction in Noncyrstalline Materials. III. Localized States in a Psuedogap and Near Extremities of Conduction Valence Bands," *Philos. Mag.*, Vol. 19, pp. 835-52 (1969).

3. J. S. Sanghera, J. Heo, J.D. Mackenzie, "Chalcohalide Glasses," *J. Non-Cryst. Solids*, Vol. 103, pp. 155-178 (1988).

4. V. F. Kokorina, "Glasses for Infrared Optics," CRC Press, (1996).

5. W.C. Lacourse, A.K. Varshneya, and A.G. Clare, "Properties and new applications for chalcogenide glasses, fibers, and films," *Proceedings of the Selenium Tellurium Development Associations 5th International Symposium*, pp. 267-71 (1994).

6. A.B. Seddon, "Chalcogenide glasses: a review of their preparation, properties, and applications, *J. Non-Cryst. Solids*", Vol. 184, pp. 44-50 (1995).

7. M. Saito and K. Kikuchi, "Infrared optical fiber sensors," *Opt. Rev.*, Vol. 4, No. 5, pp. 527-538 (1997).

8. S. Hudgens and B. Johnson, "Overview of phase-change chalcogenide nonvolatile memory technology," *MRS Bull.*,Vol. 29, No. 11, pp. 829-832 (2004).

9. L. K. Malhorta, Y. Sripathi, and G. B. Redd, "Materials science aspects of phase change optical recording," *B. Mater. Sci.*, Vol. 18, No. 6, pp. 725-739 (1995).

10. J. Heo, "Rare-earth doped chalcogenide glasses for fiber-optic amplifiers," *J. Non-Cryst. Solids*, Vols. 326-327, pp. 410-415 (2003).

11. I.T. Sorokina and K. L. Vodopyanov, eds., "Mid-infrared fiber lasers," Springer, (2003).

12. Amorphous Materials, Inc., <http://www.amorphousmaterials.com>.

13. J. Heo and J. D. Mackenzie, "Chalcohalide glasses I. synthesis and properties of Ge-S-Br and Ge-S-I Glasses," *J. Non-Cryst. Solids*, Vol. 111, pp. 29-35 (1989).

14. H. Krebs and H. Welte, "Atomic distribution in glass forming system Ge-As-Se," *J. Solid State Chem.*, Vol. 2, pp. 182-187 (1970).

15. P. Tronc, M. Nemsoussan, A. Breac, and C. Cebenne, "Optical-absorption edge and Raman scattering in $Ge_{1-x}Se_x$ glasses," *Phys. Rev. B*, Vol. 8, pp. 5947-5956 (1973).

16. J.C. Phillips, "Structural principles of amorphous and glassy semiconductors," *J. Non-Cryst. Solids*, Vol. 35, pp. 1157-1165 (1980).

17. J.C. Phillips, "Topology of covalent non-crystalline solids I: Short-range order in chalcogenide alloys," *J. Non-Cryst. Solids*, Vol. 34, pp. 153-181 (1979).

18. J.C. Phillips, "Topology of covalent non-crystalline solids II: Medium-range order in chalcogenide alloys and α-Si(Ge)." *J. Non-Cryst. Solids*, Vol. 43, pp. 37-77 (1981).

19. U. Senapati and A. Varshneya, "Configurational arrangements in chalcogenide glasses: A new perspective on Phillips' constraint theory," *J. Non-Cryst. Solids*, Vol. 76, pp. 109-116 (1985).

20. Z. U. Borisova, "Glassy Semiconductors," Plenum Press, (1981).

21. T. Nang, M. Okuda, T Matsushita, "Composition Dependence of the Refractive Index and its Photoinduced Variation in the Binary Glass Systems: $Ge_{1-x}Se_x$ and $As_{1-x}Se_x$," *J. Non-Cryst. Sol.*, Vol. 33, pp. 311-323 (1972).

22. A. N. Sreeram, D. R. Swiler, and A. K. Varshneya, "Gibbs-Demarzio equation to describe the glass transition temperature trends in multicomponent chalcogenide glasses," *J. Non-Cryst. Sol.*, Vol. 127, pp. 287-297 (1991).

23. J. Nishii, "Studies on Non-oxide glasses for infrared optical fibers," Ph.D. Thesis, *Tokyo Metropolitan University*, (1989).

24. G. Burns, “Solid-State Physics,” Academic, (1985).

25. K. Sangwal and W. Kucharczyk, “Relationship between density and refractive index of inorganic solids,” *J. Appl. Phys.*, Vol. 20, pp. 522-525 (1987).

26. M. A. Popescu, “Non-Crystalline Chalcogenides,” Springer, (2000).

27. P. Patel and N. D. Kreidl, “As-Ag-Se Glasses,” *J. Am. Ceram. Soc.*, Vol. 58, Nos. 5-6, pp. 263-268 (1975).

28. Z. U. Borisova and T. S. Rykova, “Some features of glass formation in the silver-arsenic-selenium system,” *Fiz. Khim. Stekla*, Vol. 3, No. 6, pp. 585-589 (1977).

29. W. A. King, A. G. Clare and W. C. Lacourse, “Laboratory preparation of highly pure As_2Se_3 glass,” *J. Non-Cryst. Solids.* Vol. 181, pp. 231-237 (1995).

30. A. M. Reitter, A N. Sreeram, A K. Varshneya, D.R. Swiler, “Modified preparation procedure for laboratory melting of multicomponent chalcogenide glasses,” *J. Non-Cryst. Solids*, Vol. 139, pp. 121-128 (1992).

31. E. Hecht, “Optics,” Addison Wesley, (2002).

32. B. J. Stagg and T. T. Charalampopulos, “Sensitivity of the reflection technique: optimum angles of incidence to determine the properties of materials,” *Appl. Optics*, Vol. 31, No. 22, pp. 4420-4427 (1992).

33. D. A. Pinnow and T. Rich, “Development of a calorimetric method for making precision optical absorption measurements,” *Appl. Optics*, Vol. 12, pp. 984-992 (1973).

34. H. B. Rosenstock, M. Hass, D. Gregory, and J. A. Harrington, “Analysis of laser calorimetric data,” *Appl. Optics*, Vol. 16, pp. 2837-2842 (1977).

35. J. S. Sanghera, V. Q. Nguyen, R. Miklos, and I. D. Aggarwal, “Measurement of bulk absorption coefficients of chalcogenide and chalcohalide glasses at 10.6 μm using CO_2 laser calorimetry,” *J. Non-Cryst. Solids*. Vol. 161, pp. 320-322 (1993).

36. M. Hass, “Measurement of very low optical absorption coefficients in bulk materials,” *Opt. Eng.*, Vol. 17, No. 5, pp. 525-529 (1978).

37. H. Preston-Thomas, “The international temperature scale of 1990 (ITS90),” *Metrologia*, Vol. 27, pp. 3-10 (1990).

38. B. W. Mangum and G. T. Furukawa, “Guidelines for realizing the International Temperature Scale of 1990 (ITS-90),” *Natl. Inst. Stand. Technol. Tech. Note 1265* (1990).

39. B. Temelkuran, S. D. Hart, G. Benoit, J.D. Joannopoulos, Y. Fink, "Wavelength-scalable hollow optical fibres with large photonic band gaps for CO_2 laser transmission", *Nature*, Vol. 420, pp. 650-653 (2002).

40. K. White, B. Kumar, A. K. Rai, “Effect of deposition rate on structure and properties of As_2S_3 Film,” *Thin Solid Films*, vol. 161, pp. 139-47 (1988).

41. M. E. Marquez, J. M.Gonzalez-Leal, A. M. Bernal-Oliva, R. Prieto-Alcon, J. C. Navarro-Delgado, M. Vlcek, “Calculation and analysis of the complex refractive index of uniform films of the As-S-Se glassy alloy deposited by thermal evaporation,” *Surf. Coat. Tech.*, Vol. 122, No. 1, pp. 60-66 (1999).

42. K. Tada, N. Tanino, T Murai, M. Aoki, “Sputtered films of sulphur- and/or selenium-based chalcogenide glasses for optical waveguides,” *Thin Solid Films*, Vol. 96, No. 2, pp. 141-147 (1982).

43. S. Ramachandran, S. G. Bishop, “Excitation of Er^{3+} emission by host glass absorption in sputtered films of Er-doped $Ge_{10}As_{40}Se_{25}S_{25}$ glass,” *Appl. Phys. Lett.*, Vol. 73, No. 22, pp. 3196-3198 (1998).

44. P. Nemec, M. Frumar, B. Frumarova, M. Jelinek, J. Lancok, J. Jedelsky, “Pulsed laser deposition of pure and praseodymium-doped Ge-Ga-Se amorphous chalcogenide films,” *Opt. Mater.*, Vol. 15, No. 3, pp. 191-197 (2000).

45. R. Asal, H. N. Rutt, “Optical properties of laser ablated gallium lanthanum sulphide chalcogenide glass thin films prepared at different deposition laser energy densities,” *Opt. Mater.*, Vol. 8, No. 4, pp. 259-268 (1997).

46. M. Ohring, “Materials Science of Thin Films – Deposition and Structure,” Academic Press (2002).

47. M. Miyagi, A. Hongo, Y. Aizawa, and S. Kawakami, “Fabrication of germanium-coated nickel hollow waveguides for infrared transmission,” *Appl. Phys. Lett.*, Vol. 43, No. 5, pp. 430-432 (1983).

48. M. Saito, M. Takizawa, and M. Miyagi, “Infrared optical fibers with vapor deposited cladding layer,” *J. Lightwave Technol.*, Vol. 7, No. 1, pp. 158-162 (2006).

Chapter IV Ag/PS Hollow Glass Waveguides for THz Radiation

IV.A Background

Applications in spectroscopy, radiometry, and the delivery of high power CO_2 and Er:YAG laser radiation have driven the development of infrared (IR) transmitting waveguides over the last 40 years [1]. The field of THz radiation sources, waveguides, and detectors is comparatively new. The first commercial THz spectrometer became available in the year 2000, which roughly coincides with the earliest studies of THz waveguides [2]. Many IR waveguiding technologies have been applied to THz frequency radiation, such as photonic crystal fibers (PCFs) [3-4], hollow Bragg fibers (HBFs) [5-6], and solid core fibers [7-8], but the metal/dielectric HGW technology has not. Ray optics calculations in Section II.J indicate that this technology could be used to fabricate waveguides with lower loss than any THz radiation transmitting waveguide that has been demonstrated to date.

A significant challenge in the application of metal/dielectric HCW technology to THz waveguides is that much greater dielectric layer thicknesses are required for low loss. Eq.(II.31) shows that the optimum dielectric layer thickness for metal/dielectric HCWs is proportional to the design wavelength. The wavelength of THz frequency radiation is 10 to 100 times longer than IR radiation; hence the dielectric film thickness of a metal/dielectric HCW designed to transmit THz frequency radiation must be 10 to 100 times greater than those designed for IR radiation.

The goal of this study is to extend the metal/dielectric HCW technology used for IR waveguides to the fabrication of waveguides for the transmission of THz frequency radiation. First, the methods commonly employed in the fabrication of IR transmitting metal/dielectric HCWs are compared to determine the potential for their successful application to THz waveguides. It is shown that the liquid flow coating (LFC) process used to deposit polymer thin films has the greatest potential for THz HCWs. The LFC process is studied in detail to determine the important processing parameters to produce thicker polymer films. It is shown in Section II.J that PS has good optical properties for making good metal/dielectric HCWs. In this chapter it is demonstrated that solutions formed by dissolving PS in toluene have favorable rheological properties for depositing relatively thick polymer films by the LFC process. PS films are deposited in Ag-coated HGWs using highly concentrated PS/toluene solutions. The Ag/PS HGWs thus formed are characterized using FTIR spectroscopy and a Coherent SIFIR-50 CO_2 pumped CH_3OH laser tuned to emit 119 μm (2.5 THz) radiation.

IV.B Fabrication of Metal / Dielectric Hollow Core Waveguides

Numerous techniques have been demonstrated for fabricating metal/dielectric HCWs. Researchers at Tohoku University fabricated nickel tubes with inner Ge, ZnS, or PbF_2 dielectric coatings by sputtering the dielectric layer onto an aluminum substrate, electroplating a thick nickel layer over the dielectric, and then dissolving the aluminum tube [9]. Laakmann deposited Ag and PbF_2 layers on a thin metal strip, which was then rolled into a tube and inserted into a stainless steel sleeve [10]. Bhardwaj et al. used a

more direct technique in which the inner surface of a silver tube is partially converted to dielectric AgBr or AgCl using a gas or liquid phase reaction [11]. The surface of the silver tube was chemically polished prior to the addition of the dielectric film. A smoother silver surface, and therefore improved performance, can be achieved by depositing a silver coating on the inside of a smooth glass or plastic tube. This technique was first demonstrated by researchers at Tel Aviv University, who deposited silver coatings on the inner surface of polyethylene and Teflon tubing using an electroless liquid phase chemical deposition (ELPCD) process [12]. In this technique a dielectric AgI thin film is formed by reacting a portion of the silver layer with a solution containing I^-. Researchers at Rutgers University have fabricated the lowest loss Ag/AgI waveguides using high quality fused silica and polycarbonate tubing [13].

Ag/AgI HCWs are limited to a single dielectric layer because of the subtractive nature of the fabrication process. Seeking to improve upon Ag/AgI HCWs, researchers at Rutgers Univeristy have developed new ELPCD processes to deposit dielectric thin films with metal sulphide compositions, such as CdS and PbS [14]. Since the films are added over the silver layer, multiple layers can be deposited to form a periodic alternating high/low refractive index structure. In theory, a multilayer dielectric waveguide should have significantly lower loss than a waveguide consisting of only a single layer of either dielectric material. In practice, the potential loss reduction by depositing multilayer dielectric films is compromised by the increase in roughness as the overall thickness of the dielectric stack increases [15].

THz metal/dielectric HCWs require much thicker dielectric films than IR transmitting HCWs. The increase in roughness upon depositing 10 to 100 times thicker

films may therefore be prohibitive in the application of Ag/AgI or Ag/metal sulphide technology to HCWs designed for THz frequency radiation. However the increase in scattering resulting from rougher films will be at least partially offset by the decrease in scattering losses at these longer wavelengths. In practice it is difficult to form thick dielectric coatings limiting the choices for fabricating a viable THz HCW. The refractive indices of AgI, CdS, and PbS at IR wavelengths are 2.2, 2.3, and 4, respectively. Assuming the refractive indices of these materials are similar at THz frequencies, the dielectric film thicknesses for single layer metal/dielectric HCWs optimized for 119 μm are 9.7 μm, 9.3 μm, and 5.4 μm for AgI, CdS, and PbS, respectively. The growth rate of the silver films deposited by the ELPCD process is about 1 μm/hr. [15], so it will take at least 10 hours to fabricate a single Ag/AgI HGW optimized for 119 μm radiation. The growth rate of CdS and PbS films are 0.14 μm/hr. and 0.4 μm/hr, respectively [16]. To fabricate a single layer HGW the deposition times for CdS and PbS are therefore about 66 hours and 14 hours, respectively. Application of the fabrication processes used to make Ag/AgI and Ag/metal sulphide IR transmitting HCWs to THz radiation would result in increased roughness, long deposition times, and would also increase the hazardous waste generated.

Researchers at Tohoku University have developed metal/polymer coated HGWs as an alternative to HCWs with inorganic dielectric thin films [17-21]. A primary motivation for their work is that polymers have refractive indices that are close to 1.4, which provides the lowest theoretical loss for metal/dielectric HCWs assuming that the polymer has no absorption [22]. Polymer films are deposited by the LFC process. The LFC process is a promising alternative to the dynamic liquid phase chemical deposition

process for fabricating HCWs optimized for the transmission of THz radiation and it is described in detail in the following section.

IV.C The Liquid Flow Coating Process

The first reported metal/polymer HGW is the polyimide (PI)/silver HCW described in a short communication from researchers at Tohoku University [17]. A silver layer is formed inside a fused silica tube by the ELPCD process. The PI film is then added over the silver by flowing a 3.9 wt. % solution through the waveguide at a rate of 12.5 cm/min. A thin liquid film remains on the surface of the silver coating after the liquid has passed through tube, a phenomenon called the Jamin effect [23-27]. The waveguide is heated to evaporate the solvent leaving a thin uniform film of PI. The waveguide thus fabricated has a loss of about 1 dB/m at the Er:YAG laser wavelength of 2.94 μm. Shortly after this initial publication, the same researchers provided a detailed analysis of the relationship between coating velocity and solution concentration to the film thickness and surface roughness of fluorocarbon polymer (FCP) films deposited inside silver coated fused silica tubing [18]. More recently researchers at Tohoku University have focused on the deposition of cyclic olefin polymer (COP) because it has low absorption at the Er:YAG and CO_2 laser wavelengths [19-21].

Figure IV-1, reproduced from Wang et al [18], and shows the roughness of FCP films formed by dip coating Ag-coated silicate glass slides in solutions with various concentrations of FCP dissolved in a perfluorochemical solution at various coating velocities. **Figure IV-2** is reproduced from the same study and shows the relationship of

the film thickness to the coating rate and solution concentration. Clearly, both the roughness and film thickness increase with increasing concentration and coating rate. The polymer film thickness, *d*, varies with solution concentration, *C*, and coating rate, *V*, according to an empirical relationship established by Fairbrother and Stubbs [26] which is

$$d = \left(\frac{a \cdot C}{200}\right) \cdot \left(\frac{V \cdot \eta}{\gamma}\right)^{1/2} \qquad \text{Eq.(IV.1)}$$

where *a* is the bore radius of the waveguide, η is the viscosity of the coating solution, and γ is the surface tension of the solution specific to the substance that is being coated. It is well known that the viscosity of polymer solutions increases with concentration. The relationship between η and *C* for the FCP solution is given by

$$\eta = 2.9 \cdot 10^{-3} \cdot 10^{0.2 \cdot C} \qquad \text{Eq.(IV.2)}$$

where η and *C* are expressed in Pa·s and weight percent, respectively. Substituting Eq.(IV.2) into Eq.(IV.1) provides a simple expression for *d* in terms of *C* and *V*:

$$d = A \cdot 10^{0.1 \cdot C} C \cdot V^{1/2} \qquad \text{Eq.(IV.3)}$$

where *A* is a constant that incorporates *a*, γ, and the proportionality term in Eq.(IV.2). As shown in **Figure IV-2**, experimentally determined values of *d* increase linearly with $V^{1/2}$ as predicted by Eq.(IV.3). An equation similar to Eq.(IV.3) can be established for any metal/polymer/solvent system allowing the polymer film thickness to be controlled by altering *C* or *V*. The researchers concluded that the highest quality films are produced using combinations of low *V* and high *C*, but they did not draw any conclusions about the relationship between film thickness and roughness.

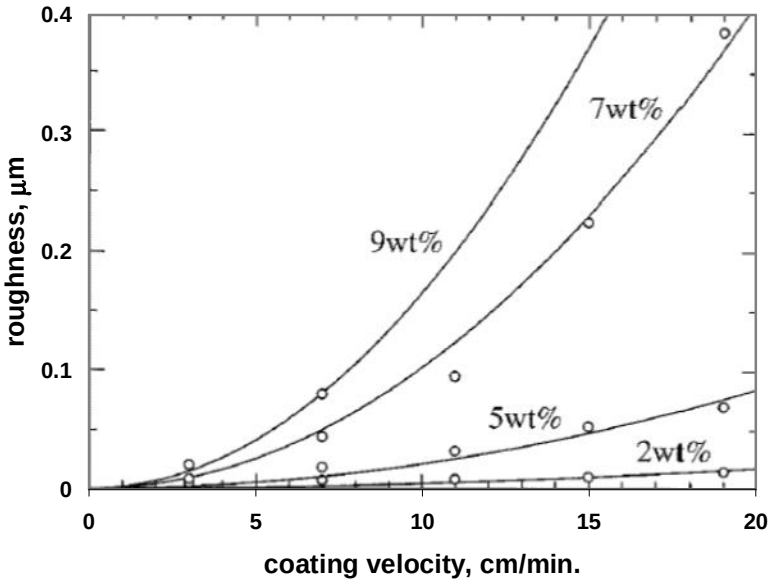

Figure IV-1: The roughness of FCP films deposited on silver coated glass substrates as a function of coating velocity for various weight concentrations of the coating solution [18].

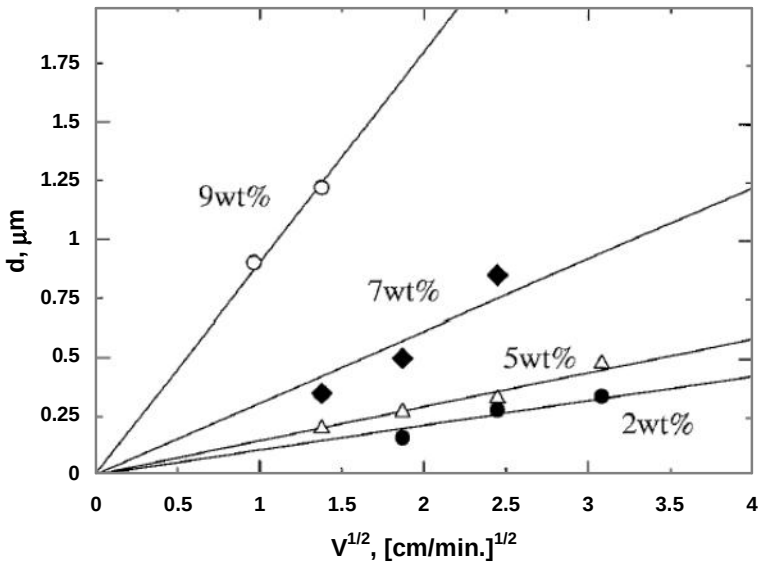

Figure IV-2: The thickness, *d*, of FCP films deposited on silver coated glass substrates as a function of square root of the coating velocity, $V^{1/2}$ for various weight concentrations of the coating solution [18].

To better study the relationship between roughness and film thickness the data of Wang et al. is further analyzed by determining the coating velocities that correspond to constant values of roughness for 5 wt. %, 7 wt. % and 9 wt. % solutions as shown in **Figure IV-3**. Contours of constant roughness may then be plotted over the data from **Figure IV-2** as shown in **Figure IV-4**. The constant roughness contours show that films with different thicknesses can have the same roughness. At low solution concentrations the roughness decreases with decreasing film thickness. The roughness is relatively independent of film thickness for high concentration solutions, but decreases with decreasing coating rate. This observation confirms that thick polymer films can be deposited with low roughness by using highly concentrated polymer solutions and low coating velocities. It is intuitive that this should be the case, because films deposited from highly concentrated solutions undergo less shrinkage during drying. The deposition of thick yet smooth dielectric films is an essential element in the fabrication of metal/dielectric HCWs designed to transmit THz radiation.

In addition to decreased roughness, the LFC process addresses the other major issues associated with extending the ELPCD process to HCWs designed for THz radiation. The volume of solution required to deposit a polymer film using the LFC process is less than 10 mL so very little waste is generated. Also, the deposition time is independent of the film thickness because the value of C can be varied to achieve any film thickness at a given coating rate. Assuming a typical coating rate of 4 cm/min., it takes only 25 minutes to deposit a polymer film inside a 1 m long HCW. Clearly the LFC process has significant advantages over the ELPCD process for the fabrication of HCWs designed to transmit THz radiation.

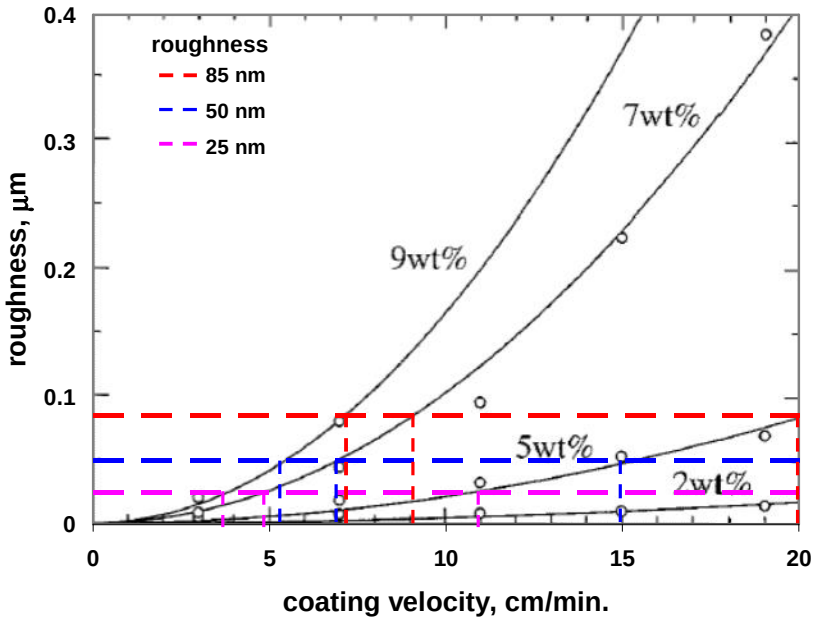

Figure IV-3: Lines laid over the plot from **Figure IV-1** illustrate the procedure for determining the coating velocities that produce films with roughness of 25 nm, 50 nm, and 85 nm for 5 wt. %, 7 wt. %, and 9 wt. % FCP solutions.

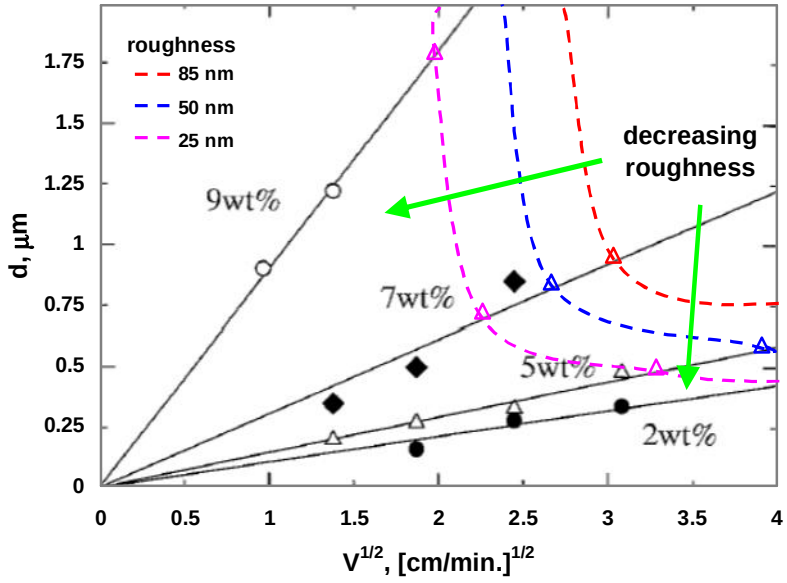

Figure IV-4: Constant roughness contours are laid over the plot from **Figure IV-2**.

IV.D Viscosity of Polystyrene/Toluene Solutions

The flow of a liquid in a capillary tube becomes less stable with increasing flow rate and increasing viscosity [27]. Unstable flow results in the formation of small droplets of liquid with regular size and spacing. This behavior is unsuitable for the deposition of uniform polymer films for metal/dielectic HCWs. The viscosity increases rapidly with concentration for the COP coating solutions used to fabricate IR transmitting HCWs. Since high concentrations are needed to deposit COP films designed for 10.6 μm radiation, researchers have had to develop special modifications to the LFC process to counteract the decreased flow stability of the coating solution. For instance, Iwai et al. [21] deposit polymers films using a closed loop pumping system, which allows the coating solution to be simultaneously drawn and pushed through the waveguide using a single peristaltic pump. Their results indicate that increased coating uniformity is obtained due the more consistent flow rate and less rapid solvent evaporation provided by this system. Increasing the polymer film thickness to achieve low loss for THz radiation requires further increasing the concentration or increasing the coating velocity, both of which decrease the flow stability. COP coating solutions produce uniform films for 10.6 μm radiation, but extension of LFC process to the film thicknesses needed for THz HCWs requires a new solvent/polymer combination with lower viscosity at high concentrations.

The ray optics calculations presented in II.J-3 show that polystyrene (PS) has near optimum optical properties for metal/dielectric HGWs designed for low loss at 119 μm (2.5 THz) radiation. The viscosity has been measured for solutions of PS in toluene to

determine if this system has favorable rheological properties for the deposition of the relatively thick films required for low loss THz HCWs. ACS grade toluene and 148G grade PS pellets purchased from Fisher Scientific and BASF Corporation, respectively, are combined in glass bottles to obtain solutions with concentrations ranging from 15 wt. % to 27.5 wt %. The bottles are capped and placed in an ultrasonic bath to homogenize the solutions. A TA Instruments AR 1000N rheometer equipped with a rotary vane spindle is used to determine the viscosity of each solution. The basic philosophy is to immerse the spindle in the solution, rotate the spindle at a constant rate, and measure the torque required to maintain a constant shear rate, $\partial u/\partial y$. The shear stress, τ, applied to the liquid is calculated from the torque. The viscosity, η, is the constant of proportionality between τ and $\partial u/\partial y$ such that

$$\tau = \eta \cdot \left(\frac{\partial u}{\partial y} \right) \qquad \text{Eq.(IV.4)}$$

for Newtonian fluids [28]. The shear stress required to maintain various shear rates for a 25 wt. % PS in toluene solution is plotted in **Figure IV-5**. The linear relationship and the fact that the data passes through the origin indicate that PS/toluene solutions are Newtonian. A least squares regression is used to fit a straight line through the data and the slope is equal to the solution viscosity. The viscosities of PS/toluene solutions are plotted as a function of concentration in **Figure IV-6**. Least squares regression is then used to fit the data to the empirical relation

$$\eta = A \cdot 10^{B \cdot C} \qquad \text{Eq.(V.5)}$$

where C is the concentration and A and B are fitting parameters. It is found that the values of A and B for BASF 148G grade PS in toluene are $2.6 \cdot 10^{-3}$ and 0.079, respectively. The

viscosity-concentration relationship for FCP/perfluorochemical solutions which have $A = 2.9 \cdot 10^{-3}$ and $B = 0.2$ is also plotted in **Figure IV-6** for comparison [18]. The viscosity of the PS solutions is clearly much lower than the FCP solutions for all concentrations. At 15 wt. % the viscosity of the PS solution is about 73 times lower than the FCP solution; at 25 % the viscosity is nearly 1,200 times lower.

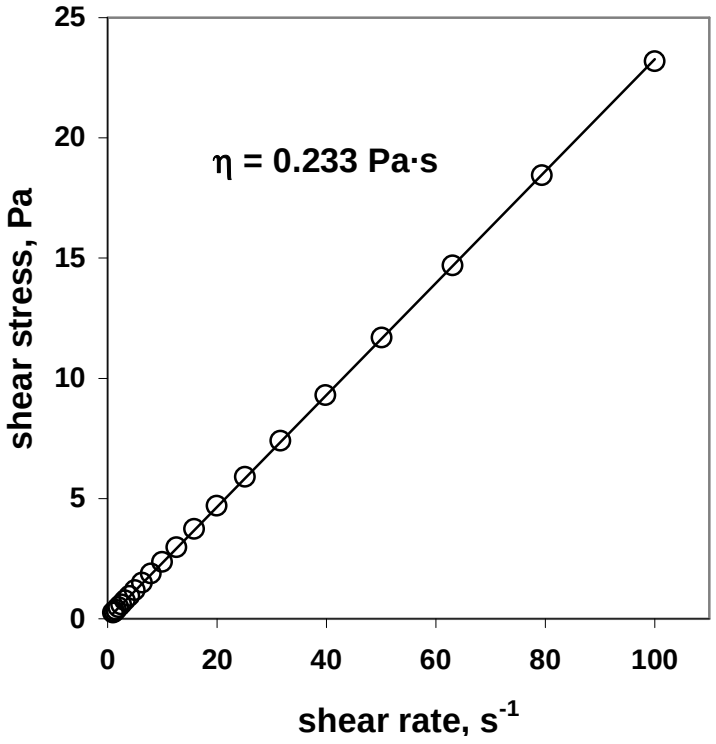

Figure IV-5: The shear stress required to maintain a constant shear rate is plotted for a 25 wt. % PS/toluene solution. The slope of the solid line fit through the data is obtained by least squares regression and is equal to the viscosity, η.

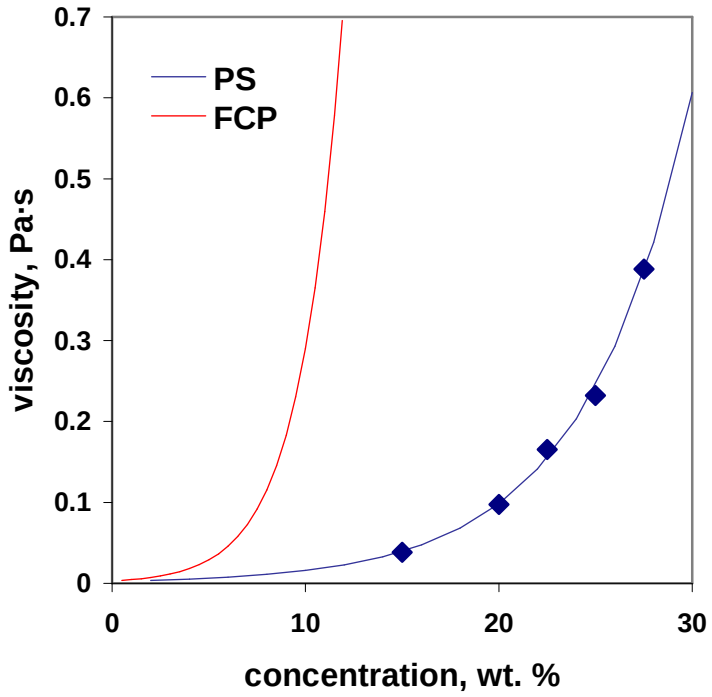

Figure IV-6: The viscosity of FCP/perflourochemical and (red) and polystyrene/toluene (blue) solutions are plotted as a function of the concentration of the polymers measured in wt. %.

In comparison to the FCP/perfluorochemical solutions, PS/toluene solutions are better suited for the deposition of polymer films in HCWs designed for low loss at THz frequencies. The low viscosity of PS solutions allows thick films to be deposited under a more stable fluid flow condition than is possible using higher viscosity FCP solutions.

IV.E Liquid Flow Coating Process Study

Section IV.B reviews the philosophy of the LFC process and describes some of the key experimental results reported by its pioneers from Tohoku University. In contrast to the prior art, which focuses on IR transmitting HGWs, this study seeks to extend the LFC process to the fabrication of waveguides optimized for THz radiation. The ray optics

calculations presented in Section II.J-3 show that Ag/PS HGWs could transmit 119 μm (2.5 THz) radiation with low loss. This new application requires the deposition of PS films that are greater than 10 times the thickness of the polymer films used in IR transmitting HGWs. As demonstrated in Section IV.C PS/toluene solutions have favorable rheological properties for the deposition of relatively thick polymer films.

Ag/PS HGWs are fabricated by first silver coating the inner wall of a silicate glass tube using the ELPCD process and then adding a PS film by the LFC process. PS films are deposited using a variety of coating rates and PS/toluene solution concentrations. The Ag/PS waveguides are characterized using FTIR spectroscopy to ascertain the relationship between these key process variables and the film thickness and uniformity.

IV.E-1 Ag Coating Deposition

The classic silver mirroring process described by Schweig [29] is the basis for the ELPCD process used to deposit Ag films to form HGWs. The ELPCD process consists of:

1. forming a silver solution and a reducer solution,
2. combining the solutions inside a glass tube causing a reaction that results in the deposition of silver metal on the inner wall of the tube and
3. flowing the solutions through the tube to continuously replenish the reactants until a silver metal film of sufficient thickness has been deposited on the inner wall of the glass substrate tube.

Rabii et al. have studied this process in detail [30]. Their process is reproduced in this study to deposit Ag coatings on silicate glass tubing. The chemicals used in this study are obtained from Acros Organics.

The silver solution is prepared by first dissolving 2.44 g of silver nitrate ($AgNO_3$) in 800 mL of deionized water contained within a 1000 mL beaker. While stirring continuously, the $AgNO_3$ solution is titrated with a 6 % ammonium hydroxide (NH_4OH) solution. Initially, the solution turns dark brown as the silver ion is converted to silver oxide according to chemical equation

$$2 \cdot AgNO_3 + 2 \cdot NH_4OH \rightarrow Ag_2O\downarrow + 2 \cdot NH_4NO_3 + H_2O \qquad \text{Eq.(IV.6)}$$

Upon further additions the NH_4OH reacts with the silver oxide to form a silver complex, a reaction described by

$$Ag_2O + 4 \cdot NH_4OH \rightarrow 2 \cdot Ag(NH_3)_2OH + 3 \cdot H_2O \qquad \text{Eq.(IV.7)}$$

The titration process continues until the solution turns clear, indicating that all of the Ag_2O has been reacted. 44 mL of a 1% sodium hydroxide (NaOH) solution are then added to the silver solution, which again causes the precipitation of Ag_2O. Titration with NH_4OH continues until the solution is once again clear. The addition of NaOH improves the adhesion and hardness of the deposited Ag film [29]. Deionized water is added to the silver solution until the total volume is 1000 mL. The silver solution thus obtained is photosensitive and must be covered with a dark cloth to prevent precipitation of silver metal prior to the initiation of the coating process.

The reducer solution is prepared by dissolving 0.56 g of dextrose ($C_6H_{12}O_6$) and 0.08 g of disodium salt of ethylenediamine tetraacetic acid (Na_2EDTA) in 1000 mL of water contained in a 1000 mL flask. The flask containing the solution is immersed in an

ultrasonic bath for 20 minutes to promote homogenization.

A schematic diagram of the system used to deposit Ag films by the ELPCD process is shown in **Figure IV-7**. A peristaltic pump is used to draw the silver solution and reducer solution into a Nalgene tube system where they are mixed and delivered to the glass substrate tube. Upon mixing the solutions, a chemical reaction is initiated that results in the precipitation of silver metal. It is unclear which of the many possible reactions by which Ag metal may be formed are active in this process; two possibilities are described by the reaction equations

$$12\cdot Ag(NH_3)_2OH + 6\cdot NaOH + C_6H_{12}O_6 \rightarrow$$
$$12\cdot Ag\downarrow + 6\cdot HCOONa + 12\cdot H_2O + 24\cdot NH_3 \qquad \text{Eq.(IV.8)}$$

and

$$2\cdot Ag(NH_3)_2OH + NaOH + C_6H_{12}O_6 \rightarrow$$
$$2\cdot Ag\downarrow + C_5H_{11}O_5COONa + 2\cdot H_2O + 2\cdot NH_3 \qquad \text{Eq.(IV.9)}$$

Initially, small clusters of Ag atoms precipitate on the inner surface of the glass substrate tube. The clusters grow and coalesce, ultimately forming a continuous silver coating. The thickness of the silver coating increases linearly with time. George has measured a growth rate of about 1 μm/hr. from solutions of the same concentrations as those used in this study [15]. The flow rate of the solutions must be optimized for each tubing bore diameter. If the flow rate is too low the reactants become significantly depleted along length of the glass substrate tube as Ag precipitates. This results in a coating thickness that decreases along the length of the glass substrate tube. If the flow rate is too fast the mixing of the reactants may not be sufficient to initiate the precipitation of Ag where the solutions enter the glass substrate tube [30].

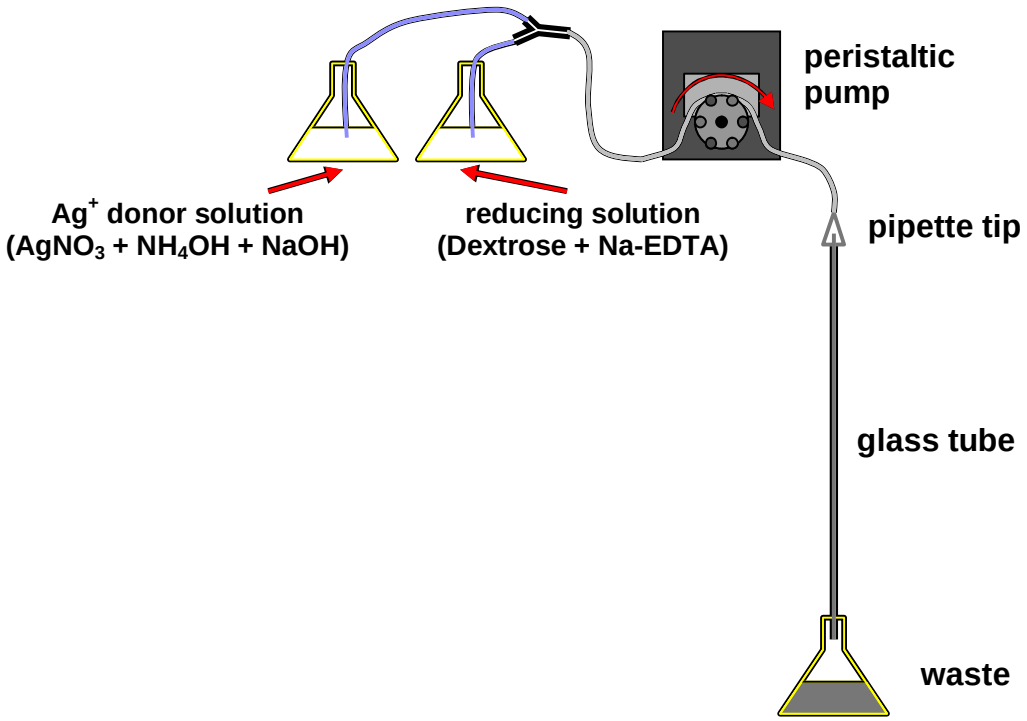

Figure IV-7: A schematic diagram of the apparatus used to deposit silver coatings via the electroless liquid phase chemical deposition (ELPCD) process.

In this study the ELPCD process is used to silver coat 1.6 mm, 1.7 mm, and 2.2 mm bore diameter silicate glass substrate tubes that are 120 cm in length. The volume flow rates of the silver solution and reducer solution are 5 mL/min., 6 mL/min. and 7 mL/min. for the 1.6 mm, 1.7 mm, and 2.2 mm tubes, respectively. The flow rate of the combined coating solutions is twice their individual flow rates. According to the theoretical calculations in Section II.J a coating thickness of only 100 nm is required to prevent leakage of 119 μm THz radiation through the HGW wall. The Ag deposition process proceeds for 40 minutes resulting in an Ag coating thickness of approximately 600 nm. George has observed that at IR wavelengths the *n* and *k* of Ag films formed by the ELPCD process are significantly lower than bulk Ag [19]. Thus, a wide thickness margin is used to account for the likelihood that the *n* and *k* of the Ag film at THz

frequencies are lower than those of bulk Ag, which were used in the theoretical calculations.

IV.E-2 Polystyrene Thin Film Deposition

A schematic diagram of the system used to deposit the PS films within Ag-coated HGWs is shown in **Figure IV-8**. The system is designed to draw PS/toluene solution through the HGW at a constant coating velocity using a Masterflex L/S peristaltic pump configured with a microbore tubing pump head. A viton feed tube connected to the upper opening of the waveguide delivers the PS/toluene solution. Viton tubing is chosen because it does not degrade when exposed to toluene. The bottom opening is connected to a U-shaped Nalgene waste tube that collects the excess solution as it exits the waveguide. The peristaltic pump acts on a 0.89 mm bore diameter PVC pump tube connected to the other end of the waste tube. Some pulsation of the volume flow rate is inherent in systems utilizing a peristaltic pump, thus the coating velocity is also pulsed. The use of a microbore pump tube minimizes the amplitude of the pulsation.

One mL of PS/toluene solution is transferred from the bulk solution to a 15 mm X 85 mm glass vial using a graduated polyethylene pipette. With the peristaltic pump engaged the feed tube is inserted into the solution. The peristaltic pump creates a pressure difference between the atmosphere over the solution and the inside of the waveguide causing solution to be drawn into the feed tube. After a specific time interval the feed tube is removed from the vial while the pump runs continuously. This action forms a column of solution that passes through the waveguide at a constant coating

velocity. The time interval between the insertion of the feed tube and its removal is adjusted for each combination of HGW bore diameter and coating velocity to produce a 10 cm long column of solution. As the column travels along the length of the HGW a thin film of PS/toluene solution is deposited over the Ag coating. Once the column of solution exits the waveguide the pump is stopped. The HGW is immediately transferred to a drying apparatus that forces air through its core at a rate of 1 L/min. The HGW remains on the drying apparatus for ~24 hours to ensure complete evaporation of the solvent.

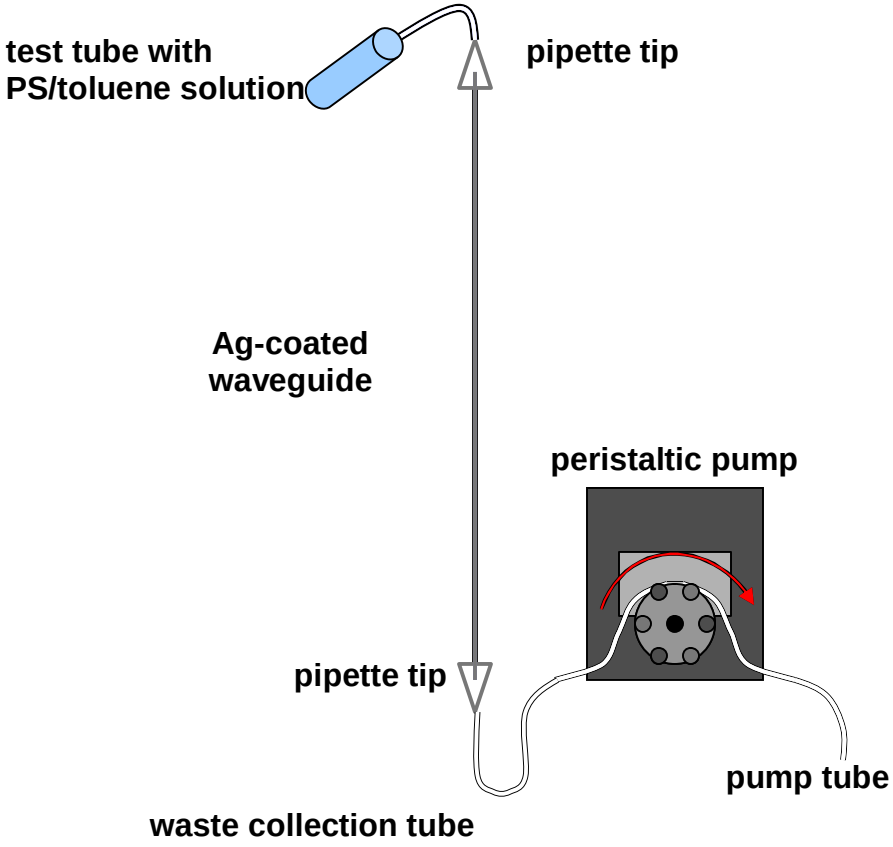

Figure IV-8: A schematic diagram of the apparatus used to deposit polymer thin films by the liquid flow coating (LFC) process.

As the column of PS/toluene solution passes though the waveguide its length decreases. The time interval between the leading meniscus entering and exiting the wave guide is measured using a stop watch. The interval is also measured for the trailing meniscus. The coating velocity is calculated by dividing the length of the waveguide by the average of the time intervals measured for both menisci. The measured coating velocity for 1.7 mm bore diameter HGWs is plotted as a function of the revolution rate of the peristaltic pump head in **Figure IV-9**. The revolution rate of a peristaltic pump head is directly related to the volume flow rate that it induces. This explains the observed relationship between the coating velocity and the revolution rate for 1.7 mm bore diameter HGWs. It is concluded that the revolution rate of the pump head provides an adequate predictor for the coating velocity.

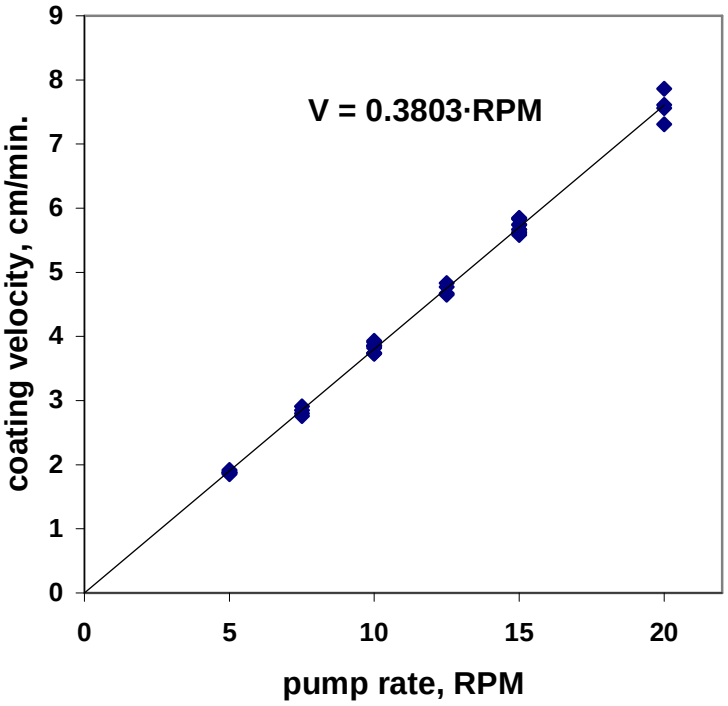

Figure IV-9: The measured coating velocity, *V*. is plotted a function of the revolution rate of the peristaltic pump head used draw PS/toluene solutions through 1.7 mm bore diameter Ag-coated HGWs.

Figure IV-10 shows an optical micrograph of the cross-section of a 2.2 mm bore diameter Ag/PS HGW. A 25 wt. % PS/toluene solution and a coating velocity of 4.5 cm/min. are used to deposit the PS film. The PS film is uniform around the circumference of the HGW and its thickness is about 11 μm. The PS film and Ag coating adhere well to each other and the glass substrate tube. The surface of the PS film is smooth relative to both the Ag coating and the roughness that would be expected for a dielectric film of similar thickness deposited by the Ag/AgI or Ag/metal sulphide coating processes.

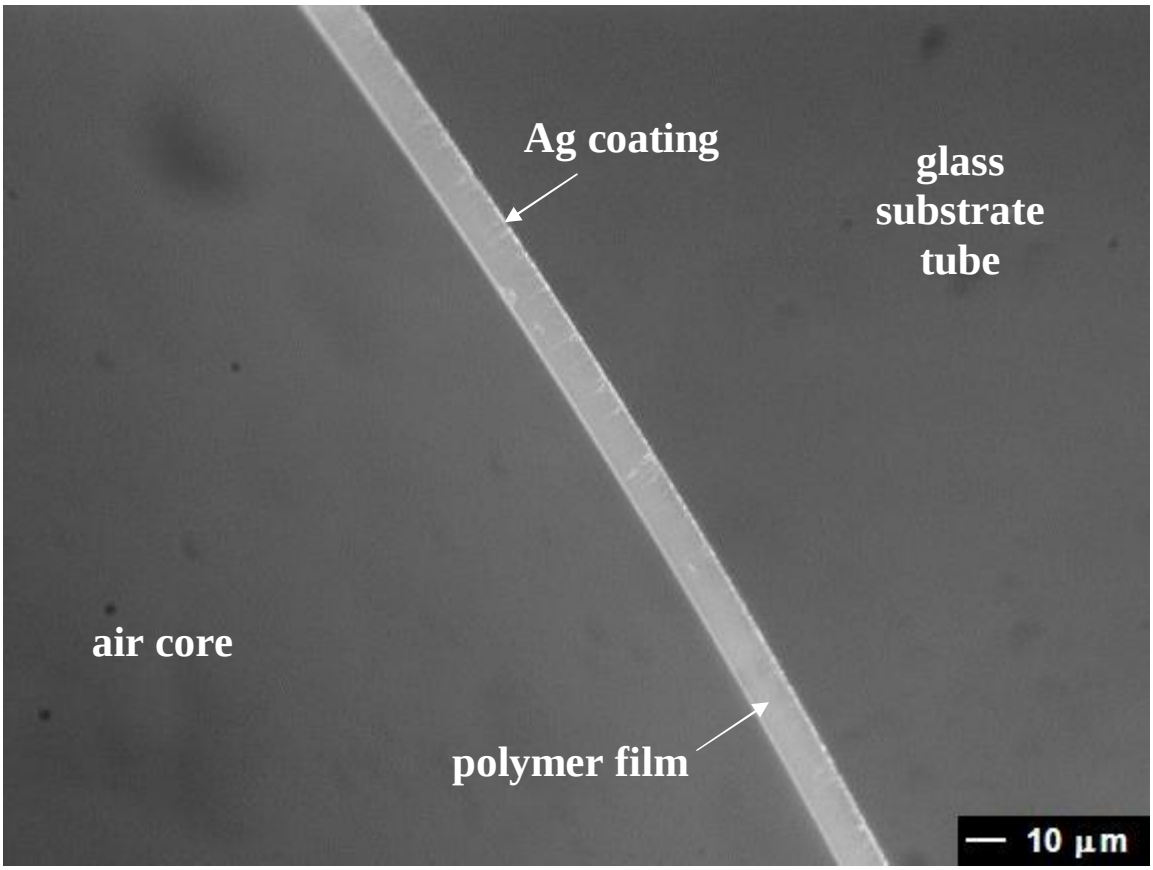

Figure IV-10: An optical micrograph of a 2.2 mm bore diameter Ag/PS HGW.

IV.E-3 Characterization of Ag/PS Hollow Glass Waveguides by FTIR Spectroscopy

FTIR spectroscopy is a powerful tool for the characterization of metal/dielectric coated HGWs. The basic set-up of an FTIR spectrometer is shown in **Figure III-11**. The spectral loss variation of a HGW can be determined by aligning the waveguide core with the beam path of the radiation traveling between the interferometer and the detector. **Figure IV-11** shows the spectral loss variation of Ag-only and Ag/COP coated HGWs measured by Abe et al. [20]. Several absorption peaks intrinsic to COP are observed beyond 4.5 μm. The stronger peaks at 3.6 μm and 1.8 μm correspond to the first and second order interference peaks of the COP film. The sharpness of the peaks indicates that the film thickness is uniform along the length of the waveguide. The reflectivity of the Ag coating is enhanced in the wavelength ranges between the interference peaks and beyond the first order peak. This effect is evident in decreased loss of the Ag/COP HGW in the same wavelength ranges.

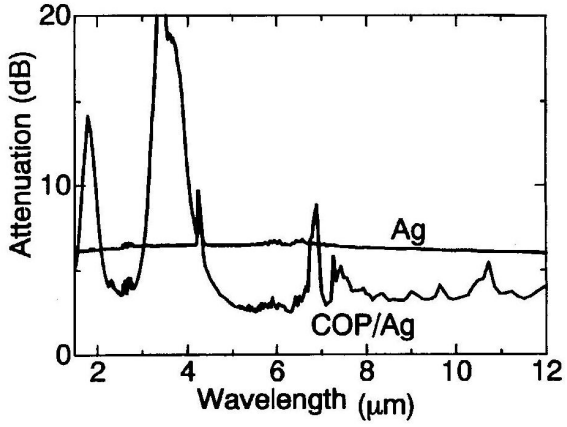

Figure IV-11: The infrared spectra of a 700 μm bore diameter, 1 m long, Ag–only HGW and Ag/COP HGW [20].

The wavelengths, λ_m, where the interference peaks occur are given by

$$\lambda_m = \frac{d \cdot \left(4 \cdot \sqrt{n^2 - 1}\right)}{m} \qquad \text{Eq.(IV.10)}$$

where d is the thickness of the dielectric film, n is the refractive index of the dielectric film, and m is a positive integer that corresponds to the order of the interference peak [20]. By rearranging Eq.(IV.10), an equation is obtained that can be used to determine the dielectric film thickness from the interference peaks observed in the IR loss spectrum of the HGW.

$$d = \frac{\lambda_m \cdot m}{4 \cdot \sqrt{n^2 - 1}} \qquad \text{Eq.(IV.11)}$$

The dielectric film thickness is typically calculated by substituting the wavelength corresponding to the first interference peak into Eq.(IV.11) with m = 1. This technique is used to calculate a COP film thickness of 0.77 μm for the Ag/COP HGW from **Figure IV-11**, assuming a refractive index of 1.53 for COP.

In this study, many 120 cm Ag-coated HGWs are prepared according to the procedure described in Section II.E-1. Each waveguide is cleaved to form two 60 cm sections. PS films are then added by the LFC process described in Section II.E-2. Individual waveguides are coated using 15 wt. %, 20 wt. %, 22.5 wt. %, 25 wt. %, or 27.5 wt. %, PS/toluene solutions. For each concentration, waveguides are fabricated using coating velocities of 1.5 cm/min., 2.4 cm/min., 3.4 cm/min., 4.7 cm/min., 6.1 cm/min., and 7.7 cm/min. The IR absorption spectrum is measured for each Ag/PS HGW using the FTIR spectroscopy set-up shown schematically in **Figure IV-12**. The Protégé 460 FTIR spectrometer used to analyze chalcogenide glasses in Section III.D is also used in this study. In this case the beam is reflected out of the spectrometer and then focused into a

Ag-only coated HGW that conditions the mode for launching into the waveguide that is to be analyzed. The Ag/PS HGW is brought into close proximity with the launch waveguide and their cores are aligned to provide maximum coupling. A white light source and InSb detector are used to collect the absorption spectrum of the Ag/PS HGWs from 1 μm to 5 μm. Between 5 μm and 20 μm the absorption bands of PS are so strong that they obscure any interference effects from the PS film.

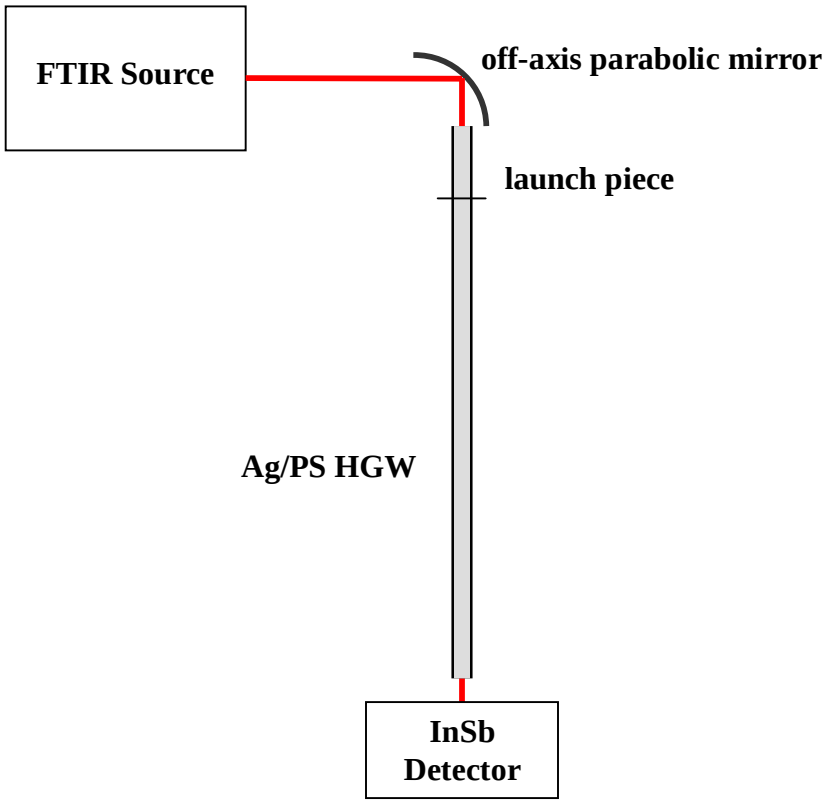

Figure IV-12: A schematic diagram of the FTIR spectroscopy set-up used to characterize Ag/PS HGWs.

Figure IV-13 shows the absorption spectra of Ag/PS HGWs deposited using three combinations of solution concentration and coating velocity: 15% / 6.1 cm/min., 22.5% / 6.1 cm/min., and 25 % / 7.7 cm/min. From 2 μm to 5 μm the spectra are

dominated by the intrinsic absorption bands of PS. Between 1 μm and 2 μm, where PS is transparent, interference peaks are clearly visible. The presence of interference peaks indicates that the PS film is uniform along the length of the HGW. The spacing of the interference peaks is longest for the 15% / 6.1 cm/min. waveguide and smallest for the 25 % / 7.7 cm/min. waveguide indicating that they have the thinnest and thickest PS films, respectively. All three films are too thick to permit the observation of the first order interference peak so Eq.(IV.11) can not be applied directly to determine the thickness of the PS films. A new method is required to determine the dielectric film thickness the thick films needed for Ag/PS HGWs designed to transmit THz radiation.

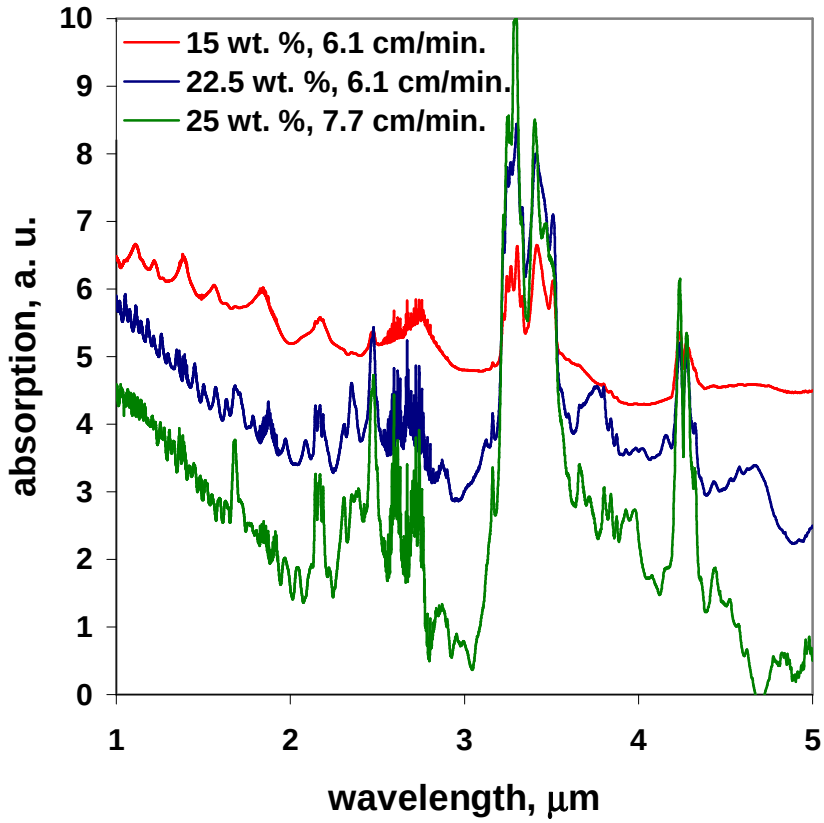

Figure IV-13: The near infrared (NIR) spectra of 1.7 mm bore diameter Ag/PS HGWs with PS films deposited using various PS/toluene solution concentrations and coating rates. The vertical scale is offset for clarity.

Substituting m = 1 and m = 2 into Eq.(IV.10) it is found that the first and second order interference peaks occur at wavelengths λ_1 and λ_2 given by

$$\lambda_1 = d \cdot \left(4 \cdot \sqrt{n^2 - 1}\right) \qquad \text{Eq.(IV.12)}$$

and

$$\lambda_2 = \frac{d \cdot \left(4 \cdot \sqrt{n^2 - 1}\right)}{2} = \frac{\lambda_1}{2} \qquad \text{Eq.(IV.13)}$$

In general the interference peaks occur at wavelengths given by

$$\lambda_m = \frac{\lambda_1}{m} \qquad \text{Eq.(IV.14)}$$

The wavenumbers, $\tilde{\nu}_m$, corresponding to each peak are then given by

$$\tilde{\nu}_m = \frac{1}{\lambda_m} = \frac{m}{\lambda_1} \qquad \text{Eq.(IV.15)}$$

The spacing between any two peaks, with orders m and m-1, in wavenumber space is given by

$$\tilde{\nu}_m - \tilde{\nu}_{m-1} = \frac{1}{\lambda_m} - \frac{1}{\lambda_{m-1}} = \frac{m}{\lambda_1} - \frac{m-1}{\lambda_1} = \frac{1}{\lambda_1} \qquad \text{Eq.(IV.16)}$$

Combining Eq.(IV.16) and Eq.(IV.11) it is found that the thickness of the dielectric film is related to the difference in wavenumber between any two adjacent interference peaks by

$$d = \frac{\left(\tilde{\nu}_m - \tilde{\nu}_{m-1}\right)^{-1}}{4 \cdot \sqrt{n^2 - 1}} \qquad \text{Eq.(IV.17)}$$

Figure IV-14 shows the absorption plotted as a function of wavenumber for a Ag/PS coated HGW fabricated using a 22.5% PS/toluene solution and coating rate of

6.1 cm/min. The spectrum between 4000 cm^{-1} to 9000 cm^{-1} (2.5 μm to 1.1 μm) is shown to emphasize the spectral region where the interference effect is not obscured by PS absorption bands. The interference peaks are evenly spaced as predicted by Eq.(IV.16). There are 9 interference peaks between 8770 cm^{-1} and 6380 cm^{-1}, so the average spacing between adjacent peaks is 266 cm^{-1}. Assuming the refractive index of PS is 1.58 and substituting 266 cm^{-1} for $\tilde{\nu}_m - \tilde{\nu}_{m-1}$ in Eq.(IV.17), the calculated PS film thickness is 7.7 μm . The calculated interference spectrum for a 7.7 μm PS film on Ag is plotted in **Figure IV-14**, along with the absorption spectra of a free standing PS thin film and a Ag-only HGW. Dashed lines connect some of the features that each spectrum has in common with that of the Ag/PS HGW. The Ag-only HGW and the Ag/PS HGW have similar atmospheric absorption peaks at 5400 cm^{-1} and 7300 cm^{-1}. The increase in absorption with increasing wavenumber, associated with the roughness of the coatings, is similar for both waveguides. The Ag/PS HGW has absorption peaks that correspond to the intrinsic absorption peaks of PS, some of which are at 5980 cm^{-1}, 4670 cm^{-1}, and 4060 cm^{-1}. The alignment of the calculated interference spectrum of a 7.7 μm PS film on Ag and the interference peaks observed in the Ag/PS HGW spectrum confirms that Eq.(IV.17) provides an accurate measure of the thickness of a dielectric film deposited in a HGW.

The PS film thickness deposited in 60 cm long Ag-coated HGWs by the LFC process is analyzed using FTIR spectroscopy. Films with various thicknesses are obtained using the various combinations of solution concentration and coating velocity. The film thicknesses are plotted as a function of the square root of the coating velocity in **Figure IV-15**. As predicted by Eq.(IV.1), the film thickness increases linearly as the square root of the coating rate increases for constant solution concentrations. The film

thickness also increases with increasing PS concentration at constant coating velocity. The largest film thickness is 16.6 μm and is achieved using a 27.5 % PS/toluene solution and 7.7 cm/min. coating velocity.

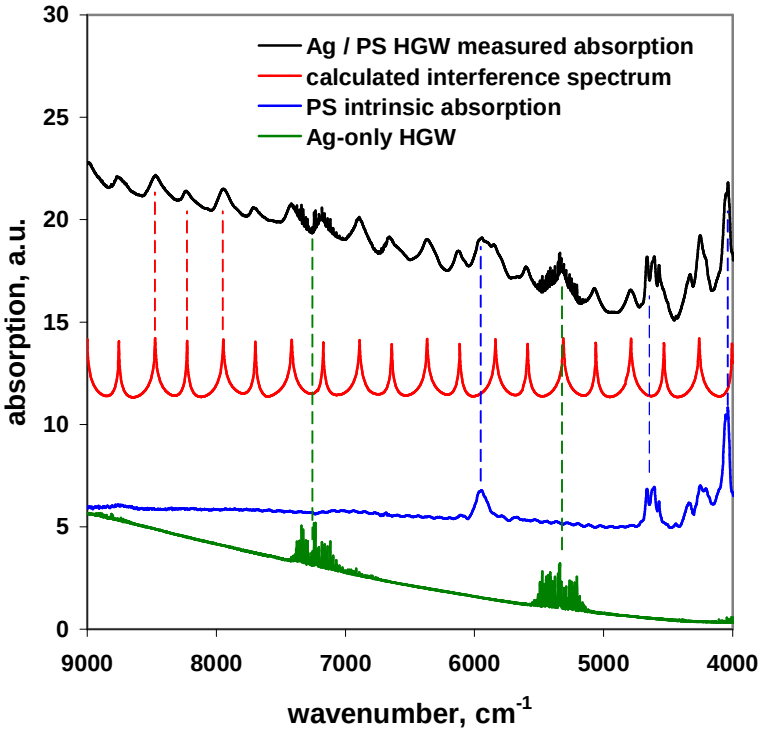

Figure IV-14: The NIR absorption spectrum of a 1.7 mm bore diameter Ag/PS HGW (black) is compared to the absorption spectra of an Ag–only HGW (green), a free standing PS film (blue), and the calculated interference spectrum for a 7.7 μm thick polystyrene layer on silver (red). The vertical scale is offset for clarity.

All of the measured PS film thicknesses are simultaneously fit to a modified form of the Fairbrother-Stubbs equation given by

$$d_{PS} = A \cdot 10^{\frac{1}{2}B \cdot C} C \cdot V^{\frac{1}{2}} \qquad \text{Eq.(IV.18)}$$

where d_{PS} is the thickness of the PS film; A is a constant that incorporates the surface tension of the PS/toluene solution, the viscosity proportionality constant from Eq.(IV.5),

and the bore diameter of the waveguide; B is the constant from Eq.(IV.5) that relates the viscosity of the polymer solution to its concentration, C; and V is the coating velocity. The value of A and B are 0.042 and 0.019, respectively, as determined by least squares regression. Thus d_{PS} is approximated by

$$d_{PS} = 0.019 \cdot 10^{0.042C} C \cdot V^{1/2} \qquad \text{Eq.(IV.19)}$$

Solid lines plotted in **Figure IV-15** correspond to the value of d_{PS} obtained by substituting the appropriate value of C and V into Eq.(IV.19). The viscosity data presented in Section IV.D gives the value B = 0.079, which is in good agreement with the value of B = 0.084 determined by fitting the thickness data to Eq.(IV.18). The agreement between Eq.(IV.19) and the measured film thickness is generally good. There is some systematic error in the predicted film thickness for C = 20 % and C = 25 %. An error of less than 1 wt. % in the coating solution concentration can account for the systematic error in the predicted film thickness.

Eq.(IV.19) provides a good estimate of the deposited PS film thickness for 1.7 mm HGWs. Referring to Eq(IV.1) it is clear that the constant A is proportional to the HGW bore diameter. Therefore the PS film thickness can be predicted for any HGW with bore diameter, a, by replacing the coefficient A = 0.019 with $A = 0.019 \cdot a/1.7$. This information allows the calculation of the approximate PS film thickness deposited in a HGW of any bore diameter with any combination of solution concentration and coating velocity.

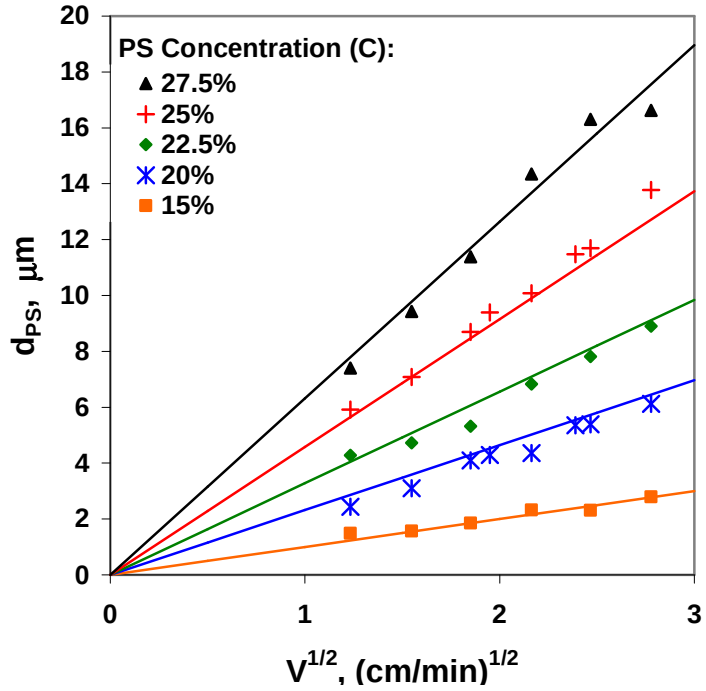

Figure IV-15: The thickness, d_{PS}, of PS films is plotted as a function of the coating rate, $V^{½}$, for various concentrations of PS in toluene. Markers indicate measured data. Solid lines indicate the film thickness calculated from the empirical equation $d = 0.019 \cdot 10^{0.042 \cdot C} \cdot C \cdot \sqrt{V}$.

IV.F Ag/PS HGW Characterization using 119 μm THz Laser Radiation

The ray optics calculations presented in II.J-3 show that the Ag/PS HGWs could have low loss for 119 μm (2.5 THz) radiation. The theoretical loss decreases with increasing PS film thickness up to 12.7 μm, for which a minimum theoretical loss of 0.18 dB/m is predicted. To confirm these calculations 1.6 mm, 1.7 mm, and 2.2 mm bore diameter Ag/PS coated HGWs are fabricated with various PS film thicknesses. The films are deposited in 120 cm long substrate tubes. The PS/toluene solution layer deposited at the inlet end of the waveguide slumps over the time that is required to coat the entire waveguide. This effect is most significant for the thickest films, imposing a limit of about

11 μm for the thickness of uniform films. Attempts to deposit thicker films often resulted in the formation of a PS plug at the bottom of the waveguide during drying.

The mode structure and transmission loss of the Ag/PS HGWs are analyzed using a Coherent, Inc. SIFIR-50 CO_2 laser pumped CH_3OH laser tuned to emit 119 μm radiation. The set-up used to characterize the waveguides is shown schematically in **Figure IV-16**. The SIFIR-50 laser emits a horizontally polarized TEM_{00} beam that is coupled into the HGW using a 7.5 cm focal length off-axis parabolic mirror. The radiation exiting the HGW is detected using a pyroelectric detector for cut back loss measurements, or a Spiricon Pyrocam I pyroelectric camera for mode profile measurements.

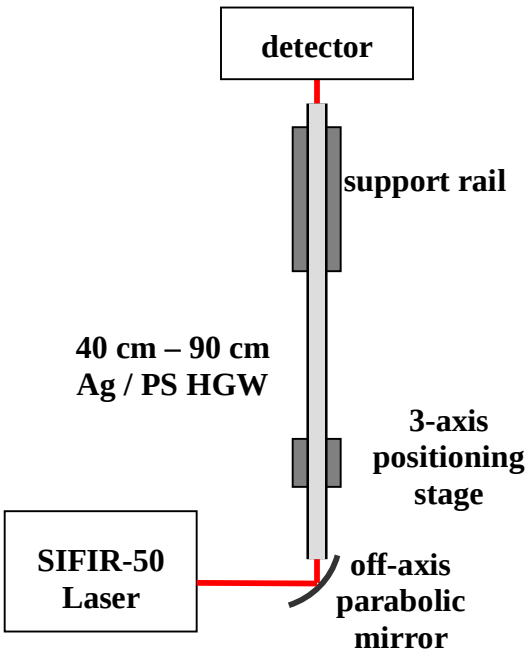

Figure IV-16: A schematic diagram of the SIFIR-50 CO_2 pumped CH_3OH laser system used to characterize Ag/PS HGWs. A thermopile detector is used for cutback loss measurements and a pyroelectric camera serves as the detector for mode profile measurements.

IV.F-1 The SIFIR-50 Laser

The SIFIR-50 is an optically pumped THz laser (OPTL) [32]. OPTLs emit THz frequency laser radiation generated by the rotational transitions of excited molecules. In this study, the SIFIR-50 laser cavity is evacuated and filled with CH_3OH gas at a pressure of ~200 mTorr. CO_2 pump laser radiation at 9.62 μm is coupled into the cavity where it is absorbed by the CH_3OH molecules through excitation of the C-O stretch mode. The molecules relax by emitting a photon at 119 μm, corresponding to transition from the J = 16 to J = 15 rotational energy levels. A physical representation of this process is shown in **Figure IV-17**. The energy that remains after the emission of the THz photon dissipates as heat when the CH_3OH molecules collide with the wall of the cavity. The maximum efficiency of this laser is only 4%, but it is the highest power OPTL laser that has been demonstrated [33]. The power output of the SIFIR-50 laser at the 119 μm line is ~25 mW.

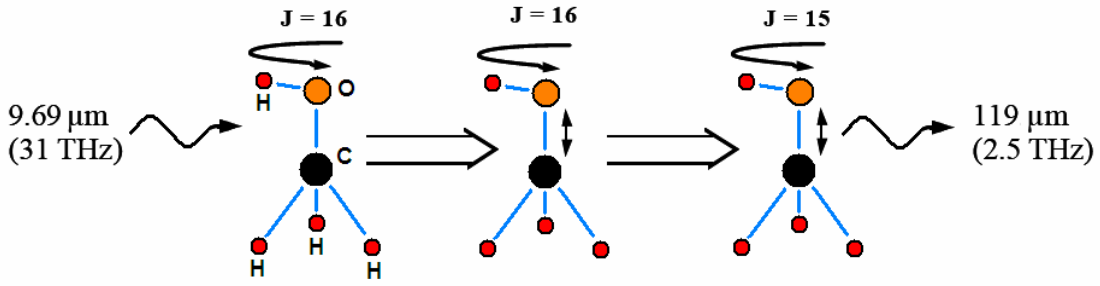

Figure IV-17: A physical representation of the process by which a 9.69 μm photon is absorbed by a CH_3OH molecule resulting in the emission of a 119 μm photon [31].

IV.F-2 Mode Profiles

The mode profile of 119 μm radiation propagating in Ag/PS HGWs is observed by measuring the spatial intensity variation of the radiation exiting 90 cm long waveguides. Separate images are collected with horizontal and vertical wire grid polarizers inserted between the output end of the waveguide and the pyroelectric camera to determine the polarization state of the radiation exiting the waveguides. The waveguide is aligned with the beam path and its position is adjusted to achieve the maximum output power. **Figure IV-18** shows the modes profiles of 1.6 mm bore diameter Ag-only HGW and a Ag/PS HGW with a 10 μm PS film obtained with a horizontal polarizer, no polarizer, and a vertical polarizer. The donut shape of the mode profile for the waveguide with no PS film is characteristic of the TE_{01} mode. The horizontally and vertically polarized radiation profiles confirm that the electric field is parallel to the walls of the waveguide, also a characteristic of the TE_{01} mode. In contrast, the mode profile of the Ag/PS coated HGW with a 10 μm PS film is Gaussian-like and is made up almost entirely of horizontally polarized radiation. These are characteristics of the HE_{11} mode.

Figure IV-19 shows the mode profiles of 1.6 mm, 1.7 mm, and 2.2 mm bore diameter Ag/PS HGWs with various PS coating thickness. The mode profile of the radiation propagating in the guide changes significantly with the HGW bore diameter and the PS coating thickness. The waveguide with no PS coating has a significant TE_{01} component. As the PS thickness increases the HE_{11} component of the mode profiles increases significantly. Radiation propagates primarily in the HE_{11} mode in the

waveguides with the thickest PS films. Some higher order modes propagate in the 2.2 mm waveguides that are not present in the 1.6 mm or 1.7 mm Ag/PS coated HGWs. The observed increase in the number of propagating modes with increasing waveguide bore diameter is consistent with Eq.(II.2) and the experimental observations of Harrington et al. [34].

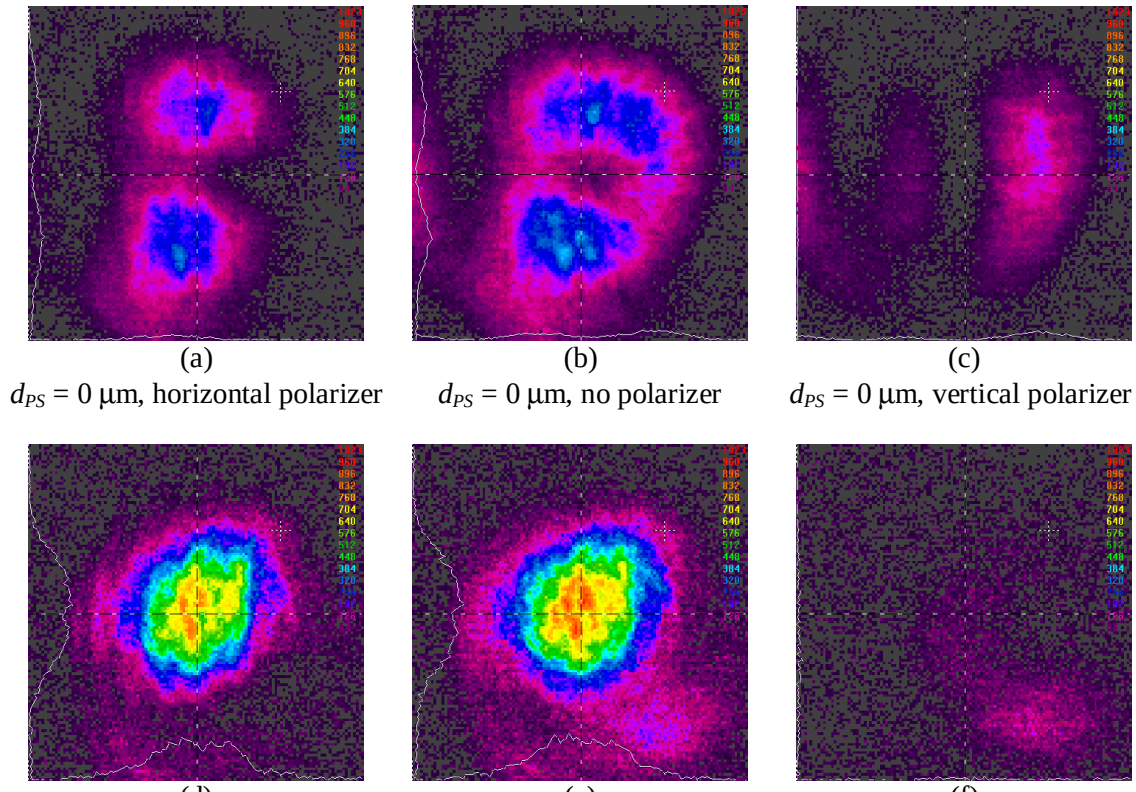

(a) d_{PS} = 0 μm, horizontal polarizer
(b) d_{PS} = 0 μm, no polarizer
(c) d_{PS} = 0 μm, vertical polarizer
(d) d_{PS} = 10 μm, horizontal polarizer
(e) d_{PS} = 10 μm, no polarizer
(f) d_{PS} = 10 μm, vertical polarizer

Figure IV-18: The far-field spatial intensity variation of 119 μm radiation upon exiting 90 cm long 1.6 mm bore diameter Ag/PS HGWs is shown. Images *a*, *b*, and *c* correspond to a waveguide with no PS film, whereas images *d*, *e*, and *f* correspond to a waveguide with a 10 μm PS film. Images *a* and *d* are obtained with a horizontal wire grid polarizer inserted between the output end of the waveguide and the camera. Images *c* and *f* are obtained using a vertical wire grid polarizer.

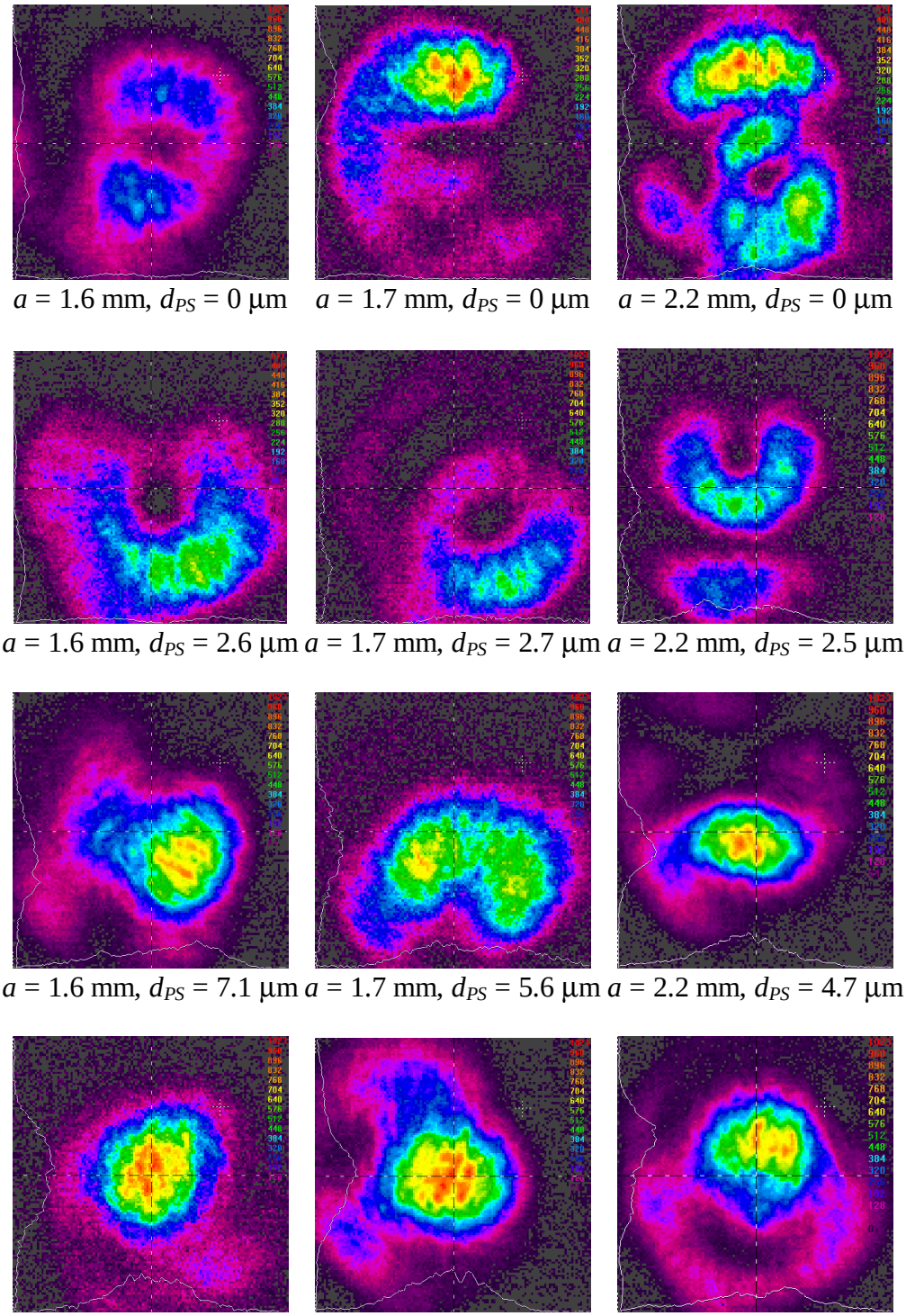

a = 1.6 mm, d_{PS} = 0 μm a = 1.7 mm, d_{PS} = 0 μm a = 2.2 mm, d_{PS} = 0 μm

a = 1.6 mm, d_{PS} = 2.6 μm a = 1.7 mm, d_{PS} = 2.7 μm a = 2.2 mm, d_{PS} = 2.5 μm

a = 1.6 mm, d_{PS} = 7.1 μm a = 1.7 mm, d_{PS} = 5.6 μm a = 2.2 mm, d_{PS} = 4.7 μm

a = 1.6 mm, d_{PS} = 10.0 μma = 1.7 mm, d_{PS} = 9.8 μma = 2.2 mm, d_{PS} = 11.3 μm

Figure IV-19: The far-field spatial intensity variations of 119 μm radiation upon exiting 90 cm long Ag/PS HGWs are shown. The bore size, a, and PS film thickness, d_{PS}, of the HGW are given below each image.

At near glancing incidence metals have high reflectivity for s-polarized radiation, but low reflectivity for p-polarized radiation due to the effect of the metal's principle angle of incidence [35]. The TE_{01} mode propagates with low loss in Ag-coated HGWs with no dielectric coating because the orientation of the electric field is parallel to the surface of the metal coating. Radiation propagating in the HE_{11} mode has a hybrid polarization state. Hybrid modes are highly attenuated for metal-only HCWs, because p-polarized radiation is absorbed by the metal. The addition of the dielectric PS film increases the reflectivity of the metal for p polarization via an inference effect and thus the loss of the hybrid modes decreases. Ray optics calculations predict a minimum HE_{11} mode loss with a 12.7 μm PS film. The transition from TE_{01} dominated transmission to HE_{11} mode transmission as the film thickness increases supports these concepts. To further characterize the transmission properties of the waveguides, cutback loss measurements are compared to the theoretical HE_{11} mode loss in the following section.

IV.G-3 Cutback Loss Measurements

The set-up shown schematically in **Figure IV-16** is used to determine the loss of Ag/PS HGWs by the cutback method. A cutback loss measurement consists of measuring the power transmitted by a long section of waveguide, P_{out}; cleaving the waveguide to remove the majority of its length while a small section of the waveguide at its proximal end is left undisturbed; and measuring the power , P_{in}, exiting the remaining short section of the waveguide. The loss, measured in dB/m, over the section of waveguide removed in

the cutback process is given by

$$loss = -\frac{10}{L} \cdot \log\left(\frac{P_{out}}{P_{in}}\right) \qquad \text{Eq.(IV.20)}$$

where L is the cutback length. In this study the initial length of the waveguides is 90 cm. They are cleaved 10 cm from their proximal end to measure P_{in}. The remaining 80 cm is reserved for another cutback measurement. A total of six cutback measurements are performed on each 90 cm waveguide. Thus the loss is measured for waveguide sections that are 80 cm to 30 cm in length.

Figure IV-20 is a plot of the quantity $-10 \cdot \log\left(\frac{P_{out}}{P_{in}}\right)$ versus L for a 1.7 mm bore diameter Ag-only coated HGW and a 1.7 mm bore diameter Ag/PS coated HGW with a 9.8 μm PS film. According to Eq.(IV.20), the slope of a straight line forced through the origin and fit to the data gives the loss of the waveguide. The loss of Ag/PS HGW is 1.7 dB/m, significantly lower than the 4.6 dB/m loss of the Ag-only HGW. **Figure IV-21** is a plot of the loss versus PS film thickness, d_{PS}, for the waveguides examined in this study. Solid lines indicate the theoretical loss of the HE_{11} mode calculated using the ray optics method. The theoretical calculations assume that the core is a vacuum, but the core was not evacuated for these measurements. To account for atmospheric absorption at 119 μm, 0.5 dB/m is added to the theoretical loss [34]. The loss of the Ag/PS HGWs is generally higher than the theoretical HE_{11} mode loss, but the predicted trend of decreased loss with increasing film thickness is clearly shown. The lowest measured loss is 0.95 dB/m for a 2.2 mm bore diameter Ag/PS coated HGW with an 8.2 μm PS film. The theoretical loss for this waveguide including atmospheric absorption is 0.68 dB/m.

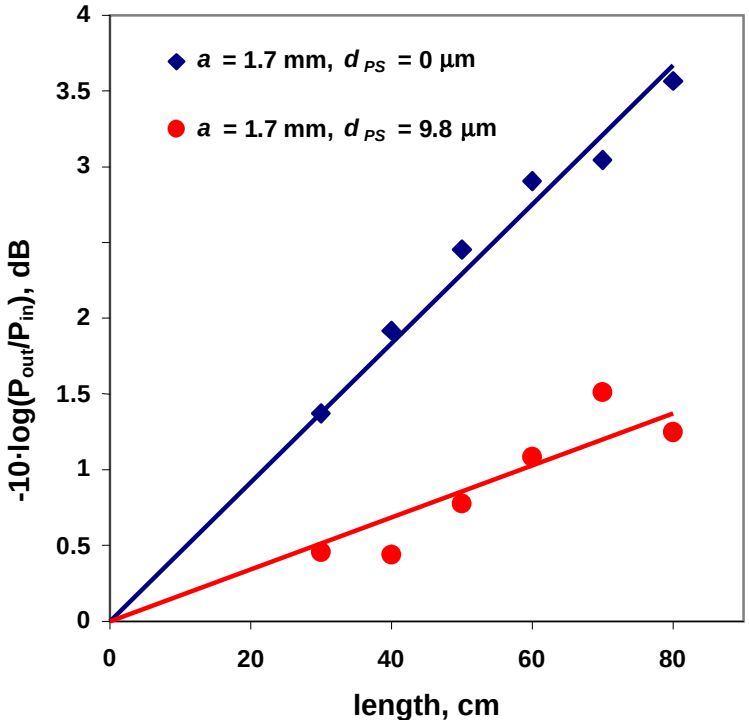

Figure IV-20: Cut-back loss measurement data is shown for 119 µm radiation propagating in 1.7 mm bore diameter Ag/PS coated HGWs. The solid lines are linear fits to the data forced through the origin.

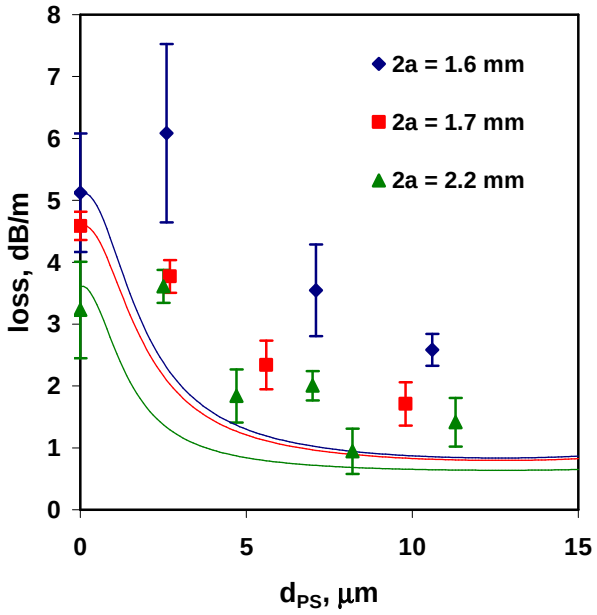

Figure IV-21: The measured transmission loss is plotted as a function of PS film thickness, d_{PS}, for 119 µm radiation propagating in 1.6 mm (blue), 1.7 mm (red), and 2.2 mm (green) bore diameter Ag/PS coated HGWs.

IV.G-4 Coupling Efficiency

The percent coupling efficiency is given by

$$coupling\ efficiency = 100 \cdot \frac{P_{input}}{P_{source}} \qquad \text{Eq.(IV.20)}$$

where P_{source} is the power emitted by the SIFIR-50 THz laser (~25 mW), and P_{input} is the power coupled into the waveguide. For each waveguide P_{input} is estimated by taking the average power collected from the six 10 cm cutback sections for each waveguide less the calculated power loss over that 10 cm section. Aside from one outlier with a coupling efficiency of 66 %, all 1.7 mm and 2.2 mm bore diameter Ag/PS coated HGWs had coupling efficiencies between 78 % and 84 %. There is no coupling efficiency trend with PS film thickness and the difference between the average coupling efficiencies for 1.7 mm and 2.2 mm bore diameter waveguides is within the scatter of the data. The measured coupling efficiencies are significantly lower for the 1.6 mm waveguides. The difference in bore diameter between the 1.6 mm and 1.7 mm waveguides is not sufficient to explain this difference. The temperature setting for the SIFIR-50 laser chiller was outside of the manufacturer recommended range during the measurement of the 1.6 mm bore diameter samples. The output power of the laser was not measured directly during the measurements taken on the 1.6 mm bore diameter waveguides so the P_{source} was taken as 25 mW, which is the output power of the SIFIR-50 laser under normal operating conditions. It is likely that the improper chiller operation resulted in a lower P_{source} for the 1.6 mm bore diameter samples introducing a systematic error into the coupling efficiency calculation for the 1.6 mm bore diameter waveguides. The coupling efficiency and loss data are summarized in **Table IV-1**.

Nubling and Harrington have calculated the overlap integral of the spatial distributions of the hybrid modes and the TEM_{00} laser mode to determine the coupling efficiency as a function of f-number [36]. The f-number is given by

$$f-number = f/D = \pi\omega/2\lambda \qquad \text{Eq.(IV.21)}$$

where f is the focal length, D is the beam diameter, ω is the beam waist, and λ is the wavelength of the radiation. When the ratio ω/a is equal to 0.64 there is optimum coupling of 98 % to HE_{11} mode. For lower values of ω/a there is greater coupling to higher order modes. For higher values the amount of radiation coupled to the HE_{11} mode increases relative to the higher order modes. However, the total coupling efficiency decreases because a significant portion of the beam intensity is incident beyond the core of the waveguide. For this work, the beam diameter of the 119 μm laser radiation is about 1 cm and the focal length of the off-axis parabolic mirror is 7.5 cm. The ratio ω/a for the 1.6 mm, 1.7 mm, and 2.2 mm HGWs is therefore 0.71, 0.67, and 0.52, respectively. The theoretical coupling efficiency for the HE_{11} mode at these ratios is greater than 90%. The observation of non-ideal coupling efficiencies is most likely due to misalignment of the waveguide and distortion of the laser beam profile by the off-axis parabolic lens. It is interesting that even the waveguides with no PS coating, which exhibit TE_{01} modes, have high coupling efficiency. This may indicate that radiation is initially coupled to hybrid modes that are then converted to TE modes within the waveguide. In general, it is observed that the TE_{01} mode is never fully developed even after propagating for 90 cm. The agreement between the loss of the waveguides with predominantly TE modes and the calculated loss for the HE_{11} mode also indicates that there may be some additional coupling losses as the TE modes develop.

Bore Diameter (mm)	Loss (dB/m)	Coupling Efficiency (%)
1.6	5.1	41
	6.1	46
	3.5	46
	2.6	53
1.7	4.6	78
	3.8	66
	2.3	81
	1.7	84
2.2	3.2	84
	3.6	79
	1.8	79
	2.0	81
	0.95	81
	1.4	79

Table IV-1. Loss and coupling efficiency of Ag/PS HGWs.

IV.G Summary

For the first time, the metal/dielectric HGW technology used primarily for IR applications has been demonstrated for THz waveguides. The greatest technological barrier to the success of this study was the need to fabricate a waveguide with a dielectric film thickness greater than 10 times that which has been previously demonstrated. Smooth, uniform, well adhered PS films with thicknesses up to 16.6 μm are deposited in Ag-coated HGWs using the LFC process. The key to the fabrication of such thick films is the high concentration yet low viscosity of the PS/toluene solution used to deposit them.

Waveguide Type	Bore / Core Diameter (μm)	Length (cm)	Frequency (THz)	Coupling Efficiency (%)	Loss (dB/m)
Polyethylene Wire [7]	200	6 – 18	0.31 - 0.36	15 - 22	0.4 -8.7
High Density Polyethylene PCF [3]	500	2	0.1 – 2	30	< 22
Teflon PCF [4]	1000	18	0.1 - 1	10	43 - 130
Hollow Cu-Coated Polycarbonate Waveguide [34]	3000	110	1.89	no data	3.9
Stainless Steel Tube [37]	280	2.4	1	40	300
Polyvinylidene Difluoride Tube [38]	8000	30	1-2	no data	6.5
Ag/PS HGW [this study]	2200	90	2.5	81	0.95

Table IV-2. Comparison of THz waveguides.

It is found that Ag/PS coated HGWs have significantly lower loss for 119 μm radiation as compared to Ag-only HGWs. The dominant transmission mode transitions from TE_{01} for the Ag-only guides to HE_{11} for Ag/PS HGWs with near optimum PS film thickness. The best waveguide demonstrated in this study is a 2.2 mm bore diameter Ag/PS HGW with an 8.2 μm PS film thickness. The measured transmission loss of this waveguide is 0.95 dB/m and the demonstrated coupling efficiency was 81 %. **Table IV-2** compares these attributes to those of other THz waveguide technologies. The Ag/PS HGW as the best THz waveguiding technology that has been demonstrated to date.

IV.H References

1. J. A. Harrington, *Infrared Fibers and Their Applications*, SPIE, (2003).

2. D. Mittleman, ed., *Sensing with Terahertz Radiation*, Springer, (2003).

3. H. Han, H. Park, M. Cho, and J. Kim, "Terahertz pulse propagation in a plastic photonic crystal fiber," *Appl. Phys. Lett.*, Vol. 80, No. 15, pp. 2634-2636 (2002).

4. M. Goto, A. Quema, H. Takahashi, S. Ono, and N. Sarukura, "Teflon photonic crystal fiber as terahertz waveguide," *Jpn. J. Appl. Phys.*, Vol. **43, No.** 2B. pp. 317-319 (2004).

5. Y. Gao, N. Guo, B. Gauvreau, O. Zabeida, L. Martinu, C. Dubois, M. Skorobogatiy "Consecutive solvent evaporation and co-rolling techniques for polymer multilayer hollow fiber preform fabrication," *J. Mat. Res.*, Vol. 21, pp 2246-2254 (2006).

6. M. Skorobogatiy, "Efficient anti-guiding of TE and TM polarizations in low index core waveguides without omnidirectional reflectors," *Opt. Lett.*, Vol. 30, pp. 2991-2993 (2005).

7. L. J. Chen, H. W. Chen, T. F. Kao, J. Y. Lu, and C. K. Sun, "Low-loss subwavelength plastic fiber for terahertz waveguiding," *Opt. Lett.*, Vol. 31, pp. 308-310 (2006).

8. S. P. Jamison, R. W. McGowan, and D. Grischkowsky, "Single-mode waveguide propagation and reshaping of sub-ps terahertz pulses in sapphire fibers," *Appl. Phys. Lett.*, Vol. 76, No. 15, pp. 1987-1989 (2000).

9. M. Miyagi, A. Hongo, Y. Aizawa, and S. Kawakami, "Fabrication of germanium-coated nickel hollow waveguides for infrared transmission," *Appl. Phys. Lett.*, Vol. 43, No. 5 (1983).

10. K. D. Laakman and M. B. Levy, "U. S. Patent No. 5,005,944 (Issued 1991).

11. P. Bhardwaj, O. J. Gregory, C. Morrow, G. Gu, and K. Burbank, “Performance of a dielectric-coated monolithic hollow metallic waveguide,” *Mater. Lett.*, Vol. 16, pp. 150-156 (1993).

12. N. Croitoru, D. Mendlovic, J. Dror, S. Ruschin, and E. Goldenberg, “Improved metallic tube infrared waveguides with inside dielectric coating,” *Proc. SPIE*, Vol. 713, pp. 6-10 (1987).

13. R. George and J. A. Harrington, "Infrared transmissive, hollow plastic waveguides with inner Ag–AgI coatings," *Appl. Opt.*, Vol. 44, pp. 6449-6455 (2005).

14. V. Gopal and J. A. Harrington, “Deposition and characterization of metal sulfide dielectric coatings for hollow glass waveguides,” *Optics Express*, Vol. 11, No. 24, pp. 3181-3187 (2003).

15. R. George, "New dielectric thin film coatings for Ag and Cu coated hollow infrared waveguides," Ph.D. Thesis, Rutgers University, (2004).

16. V. Gopal, “New dielectric coatings for low-loss hollow glass waveguides and bundles,” Ph.D. Thesis, Rutgers University, (2003).

17. Y. Kato, M. Osawa, M. Miyagi, S. Abe, M. Aizawa, and S. Onodera, “Loss characteristics of polyimide-coated silver hollow glass waveguides for the infrared,” *Electron. Lett.*, Vol. 31, No. 1, pp. 31-32 (1995).

18. Y. Wang, A. Hongo, U. Kato, T. Shimomura, D. Miura, and M. Miyagi, “Thickness and uniformity of polymer films dynamically coated inside silver hollow glass waveguides,” *Appl. Opt.*, Vol. 36, No. 13, pp. 2836-2892 (1997).

19. Y. W. Shi, Y. Wang, Y. Abe, Y. Matsuura, M. Miyagi, S. Sato. M. Taniwaki, and H. Uyama, “Cyclic olefin polymer-coated silver hollow glass waveguides for the infrared,” *Appl. Optics*, Vol. 37, No. 33, pp. 7758-7762 (1998).

20. Y. Abe, Y. Matsuura, Y. W. Shi, H. Uyama, and M. Miyagi, “Polymer-coated hollow fiber for CO_2 laser delivery,” *Opt. Lett.*, Vol. 23, pp. 89-90 (1998).

21. K. Iwai, M. Miyagi, Y. W. Shi, and Y. Matsuura, "Uniform polymer film formation in hollow fiber by closed loop coating method," *Proc. SPIE*, Vol. 6083, pp. 60830J1-60830J8 (2006).

22. M. Miyagi and S. Kawakami, "Design theory of dielectric-coated circular metallic waveguides for infrared transmission," *J. Lightwave Technol.*, Vol. LT-2, pp. 16-126 (1984).

23. R. N. Marchessault and S. G. Mason, "Flow of entrapped bubbles through a capillary," *Ind. Eng. Chem.*, Vol. 52, pp. 79-84 (1960).

24. M. Novotny, K. D. Bartle, and L. Blomberg, 'Dependence of film thickness on column radius and coating rate in preparation of capillary columns for gas chromatography," *J. Chromatogr.*, Vol. 45, pp. 469-471 (1969).

25. K. D. Bartle, "Film thickness of dynamically coated open-tubular glass columns for gas chromatography," *Anal. Chem.*, Vol. 45, pp. 1831-1836 (1973).

26. F. Fairbrother and A. E. Stubbs, "Studies in electo-endosmosis. Part VI. The 'bubble-tube' method of measurement," *J. Chem. Soc.*, Vol. 1, pp. 527-529 (1935).

27. S. Tomokita, "On the instability of a cylindrical thread of viscous liquid surrounded by another viscous fluid," *Proc. R. Soc. London Ser. A*, Vol. 150, pp. 322-337 (1995).

28. Ch. W. Macosko, *Rheology: Principles, Measurements, and Applications*, Wiley-VCH, (1994).

29. B. Schwieg, *Mirrors – A Guide to the Manufacture Mirros and Reflecting Surfaces*, Pelham, (1973).

30. C. Rabii, "Hollow glass waveguide for mid-infrared applications," Ph.D. Thesis, Rutgers University, (1998).

31. V. M. Zolotarev, B. Z. Volchek, E. N. Vlasova, "Optical constants of industrial polymers in the IR region," *Optics and Spectroscopy*, Vol. 101, No. 5, pp. 716-723 (2006).

32. E. R. Mueller, “Optically-pumped Thz laser technology,” http://www.coherent.com/downloads/OpticallyPumpedLaser.pdf

33. J. Farhoomand, and H. M. Pickett, “Stable 1.25 Watts cw far infrared radiation at the 119 μm methanol line,” *Int. J. Infrared Milli.*, Vol. 8, No. 5, pp. 441-447 (1987).

34. J. A. Harrington, R. George, P. Pedersen, and E. Mueller, “Hollow polycarbonate waveguides with inner Cu coatings for delivery of terahertz radiation,” *Opt. Express*, Vol. 12, pp. 5263-5268 (2004).

35. E. Hecht, *Optics*, Addison Wesley, (2002).

36. R. K. Nubling and J. A. Harrington, "Launch conditions and mode coupling in hollow glass waveguides," *Opt. Eng.*, Vol. 37, pp. 2454-2458 (1998).

37. R. W. McGowan, G. Gallot, and D. Grischkowsky, “Propagation of ultrawideband short pulses of terahertz radiation through submillimeter-diameter circular waveguides,” *Opt. Lett.*, Vol. 24, pp. 1431-1433 (1999).

38. T. Hidaka, H.Minamide, H. Ito, S. Maeta, and T. Akiyama, “Ferroelectric PVDF cladding terahertz waveguide,” *Proc. SPIE*, Vol. 5135, pp. 70 - 77 (2003).

Chapter V Conclusions and Future Work

In this study the design theory, materials selection, and fabrication of HCWs were considered together to develop low loss optical waveguides for the IR to THz spectral range. Waveguide technologies were developed for the transmission of IR CO_2 laser radiation at 10.6 μm and THz CH_3OH laser radiation at 119 μm (2.5 THz). However, the design theory and fabrication techniques demonstrated in this study could be applied to other wavelengths from the IR to THz spectral range. This chapter reviews the key results of this study and provides some perspective on future work that could be conducted to further develop IR to THz waveguiding technologies.

As HCWs have evolved their design has shifted from the metal tubes proposed by Marcatelli and Smeltzer to designs that minimize the interaction of light with the metal through the use of dielectric materials [1]. Most recently, innovative HCW fabrication techniques have produced IR waveguides with periodic dielectric structures that do not require metals to achieve high reflectivity and thereby low loss. The MIT / OmniGuide HBF fabrication process has harnessed the potential of the all-dielectric Bragg fiber design first proposed by Yeh et al in 1978 [2-3]. In this study, ray optics calculations show that the 0.5 dB/m loss demonstrated at 10.6 μm for the Omniguide HBF is near the theoretical minimum imposed by the high absorption of its PEI layers. This result both validates the use of ray optics for investigating HBFs and shows that improvement upon the Omniguide HBF may be realized though the use of low loss materials that can be incorporated into a multilayer structure.

Having reviewed several candidate materials for application to an OmniGuide-like HBF, it was found that only chalcogenide glasses possess the required combination of thermal and optical properties to make an HBF. Ray optics calculations of hypothetical all-chalcogenide glass HBFs show that it may be feasible to achieve orders of magnitude improvement over the loss of the Omniguide HBF at 10.6 μm. These calculations provided motivation for the identification of chalcogenide glass compositions that are compatible with the OmniGuide HBF fabrication process. $Ge_{20}Se_{80}$ glass ($\tilde{n} = 2.46 - i \cdot 9.7 \cdot 10^{-7}$) was selected as the low refractive index glass because of its relatively low refractive index among chalcogenide glasses which have low absorption at 10.6 μm as well as excellent thermal stability. To identify a high refractive index composition to combine with $Ge_{20}Se_{80}$ glass, several glass compositions were synthesized from within the Se-deficient region of Ag-As-Se glass formation. Thermal property data from the literature was combined with the results of the optical characterization, which included FTIR spectroscopy, CO_2 laser reflectometry, and CO_2 laser calorimetry. Based on this, $Ag_{25}As_{40}Se_{35}$ ($\tilde{n} = 3.10 - i \cdot 9.8 \cdot 10^{-6}$) was selected as the best glass composition for paring with $Ge_{20}Se_{80}$. Ray optics calculations of an HBF comprised of alternating layers of $Ag_{25}As_{40}Se_{35}$ and $Ge_{20}Se_{80}$ glass show that such a waveguide, with just eight layer pairs, could have lower loss than the OmniGuide HBF. Efforts to fabricate a $Ag_{25}As_{40}Se_{35}/Ge_{20}Se_{80}$ HBF were unsuccessful because it is not possible to deposit stoichiometric thin films of $Ag_{25}As_{40}Se_{35}$ glass using the thermal evaporation system developed for use in this study. However, many of the key elements of an all-chalcogenide glass HBF fabrication process were demonstrated. Continuation of this work will require the design of a system that is capable of depositing stoichiometric

multicomponent chalcogenide glass thin films. For example, thin film deposition could be done using RF sputtering, pulsed laser deposition, or simultaneous thermal evaporation from several boats, each of which contain one of the elements that comprise the target glass composition.

The THz waveguide technology has drawn heavily from designs that are used for IR waveguides. Metal tubes, solid core fibers, PCFs, HBFs, and ATIR waveguides have all been applied to the transmission of THz radiation. Prior to this study, the metal/dielectric HCW design used to fabricate the lowest loss IR waveguides had not been applied to THz radiation. In this work Ag/PS HGWs are fabricated by silver coating a glass substrate tube and then depositing a PS thin film over the silver using the LFC process. Ray optics calculations show that this combination of materials could produce a HCW for 119 μm with near minimum loss for a metal/dielectric design. Achieving low transmission loss at 119 μm required the extension of the LFC process to deposit films more than 10 times thicker than previously demonstrated in the literature. This was accomplished by depositing the PS films from highly concentrated solutions of PS dissolved in toluene. Ag/PS HGWs were characterized using a CO_2 pumped CH_3OH laser tuned to emit 119 μm radiation. The propagating modes transitioned from TE_{01} dominant to HE_{11} dominant as the film thickness increased from 0 μm to 10 μm. The loss also generally decreased over this range of film thicknesses, as predicted by ray optics calculations. With a 2.2 mm bore diameter and 8.2 μm PS film thickness, the best waveguide had a loss of 0.95 dB/m and coupling efficiency of 80 %. There are no other THz waveguides that provide such high coupling efficiency and low loss.

There are many paths for improvement over Ag/PS HGWs for THz radiation. The glass tubing used in this study is inflexible, so the migration of these processes to flexible polycarbonate tubing would provide added functionality. Many applications of THz radiation require the transmission of a broadband pulse for TDS. The dispersion of these waveguides is not well understood and must be investigated to optimize their design for use in TDS systems. Future applications of THz waveguides may require even lower losses, in which case it may be necessary to deposit multiple dielectric layers. None of the currently demonstrated coating technologies have the capability to deposit high refractive index films of optimum thickness for THz radiation. One possibility would be to deposit a composite optical film consisting of nanosized high refractive index grains, such as Si, dispersed in a polymer matrix. THz radiation would behave as though the material had optical constants given by the volume average of the optical constants of each component. A similar concept has been demonstrated using PS foam to obtain a low refractive index composite for THz radiation [4].

Chapter V.A References

1. J. A. Harrington, *Infrared Fibers and Their Applications*, SPIE, (2003).

2. E. Garmire, T. McMahon, and M. Bass, "Flexible infrared waveguides for high-power transmission," *IEEE J. Quantum Electron.*, Vol. QE-16, pp.23-32, (1980).

3. A. Yeh, A. Yariv, and E. Marom, "Theory of Bragg Fiber," *J. Opt. Soc. Am.*, Vol. 68, No. 9, pp. 1196-1201 (1978).

4. G. Zhao, M. ter Mors, T. Wenckebach, and P. G. Planken, "Terahertz dielectric properties of polystyrene foam," *J. Opt. Soc. Am. B*, Vol. 19, No. 6, pp. 1476-1479 (2002).

Curriculum Vita

Bradley F. Bowden

2002	B.Sc. in Glass Engineering Science, Alfred University, Alfred, NY
2002-2007	Graduate Research Assistant in Materials Science and Engineering, Rutgers University, New Brunswick, NJ.
2003	Teaching Assistant, "Ceramics Laboratory III," Rutgers University, New Brunswick, NJ.
2005-2007	Fiber Optics Instructor, Somerset County Technical Institute, Bridgewater, NJ.
2005	B. Bowden, J. A. Harrington, and J. Cutrera, "Chalcogenide glass 1-D photonic bandgap hollow waveguide," Proc. SPIE, Vol. 5691, pp 66-72 (2005).
2005	J. A. Harrington, P. Pederson, B. Bowden, A. Gmitter, and E. Mueller, "Hollow Cu-coated plastic waveguides for the delivery of THz radiation," Proc. SPIE, Vol. 5727, pp 143-150 (2005).
2006	A. Sengupta, A. Bandyopadhyay, B.F. Bowden, J.A. Harrington, and J.F. Federici, "Characterization of olefin copolymers using terahertz spectroscopy," Electronics Letters, Vol. 42, Issue 25, pp 1477-1479 (2006).
2007	V. Johnson, B. Bowden, and J. A. Harrington, "Polymer/metal sulfide coated hollow glass waveguides for delivery of Er:YAG laser radiation," Proc. SPIE, Vol. 6433, pp 64330E1-64330E8 (2007).
2007	A. K. Varshneya, D. J. Mauro, B. Rangarajan, and B. F. Bowden, "Deformation and cracking in Ge-Sb-Se chalcogenide glasses during indentation," Journal of the American Ceramics Society, Vol. 90, Issue 1, pp 177-183 (2007).
2007	Ph.D. Ceramic and Materials Science and Engineering, Rutgers, The State University of New Jersey, New Brunswick, NJ.